



NAVAL POSTGRADUATE SCHOOL

MONTEREY, CALIFORNIA

THESIS

**OPTIMAL FINITE-THRUST TRANS-EARTH INJECTION
(TEI) MANEUVERS FOR A LOW LUNAR ORBIT (LLO)
EARTH RETURN MISSION**

by

Omar J. Wheatley

December 2010

Thesis Co-Advisors:

I. Michael Ross
Wei Kang

Approved for public release; distribution is unlimited

THIS PAGE INTENTIONALLY LEFT BLANK

REPORT DOCUMENTATION PAGE			<i>Form Approved OMB No. 0704-0188</i>	
Public reporting burden for this collection of information is estimated to average 1 hour per response, including the time for reviewing instruction, searching existing data sources, gathering and maintaining the data needed, and completing and reviewing the collection of information. Send comments regarding this burden estimate or any other aspect of this collection of information, including suggestions for reducing this burden, to Washington headquarters Services, Directorate for Information Operations and Reports, 1215 Jefferson Davis Highway, Suite 1204, Arlington, VA 22202-4302, and to the Office of Management and Budget, Paperwork Reduction Project (0704-0188) Washington DC 20503.				
1. AGENCY USE ONLY (Leave blank)		2. REPORT DATE December 2010	3. REPORT TYPE AND DATES COVERED Master's Thesis	
4. TITLE AND SUBTITLE Optimal Finite-Thrust Trans-earth Injection (TEI) Maneuvers for a Low Lunar Orbit (LLO) Earth Return Mission			5. FUNDING NUMBERS	
6. AUTHOR(S) Wheatley, Omar J.			8. PERFORMING ORGANIZATION REPORT NUMBER	
7. PERFORMING ORGANIZATION NAME(S) AND ADDRESS(ES) Naval Postgraduate School Monterey, CA 93943-5000			10. SPONSORING/MONITORING AGENCY REPORT NUMBER N/A	
9. SPONSORING /MONITORING AGENCY NAME(S) AND ADDRESS(ES) NASA JSC			11. SUPPLEMENTARY NOTES The views expressed in this thesis are those of the author and do not reflect the official policy or position of the Department of Defense or the U.S. Government. IRB Protocol number _____N/A_____.	
12a. DISTRIBUTION / AVAILABILITY STATEMENT Approved for public release; distribution is unlimited			12b. DISTRIBUTION CODE	
13. ABSTRACT (maximum 200 words) Pseudospectral methods are used to efficiently solve complex, non-linear optimal control problems and can be used to develop rapid and robust control solutions in astrodynamics applications. With the renewed efforts in resuming future manned missions to the moon or near-earth asteroids, fuel optimal flight trajectories are desired in order to alleviate the need for overestimates in fuel carried onboard, which has a negative impact on the overall spacecraft design. This thesis uses a pseudospectral optimal control solver, DIDO©, to solve for a fuel optimal moon-to-earth trajectory using only the auxiliary engines of the Orion Crew Exploration Vehicle (CEV) for the entire mission. Additionally, higher-order necessary conditions are examined to test the extremality of the computed solution. Singular arcs that appear in a main engine variable thrust, fuel optimal trajectory are examined by applying the Bellman Pseudospectral method. The feasibility of using the CEV auxiliary engines in place of the main engines for the singular arc maneuver is also investigated.				
14. SUBJECT TERMS Optimal Control; Singular Arc; Pontryagin's Principle; Bellman's Principle; pseudospectral			15. NUMBER OF PAGES 129	
			16. PRICE CODE	
17. SECURITY CLASSIFICATION OF REPORT Unclassified	18. SECURITY CLASSIFICATION OF THIS PAGE Unclassified	19. SECURITY CLASSIFICATION OF ABSTRACT Unclassified	20. LIMITATION OF ABSTRACT UU	

NSN 7540-01-280-5500

Standard Form 298 (Rev. 2-89)
Prescribed by ANSI Std. Z39-18

THIS PAGE INTENTIONALLY LEFT BLANK

Approved for public release; distribution is unlimited

**OPTIMAL FINITE-THRUST TRANS-EARTH INJECTION (TEI) MANEUVERS
FOR A LOW LUNAR ORBIT (LLO) EARTH RETURN MISSION**

Omar J. Wheatley
Lieutenant Commander, United States Navy
B.S., University of Colorado, 1998

Submitted in partial fulfillment of the
requirements for the degrees of

**MASTER OF SCIENCE IN ASTRONAUTICAL ENGINEERING
and
MASTER OF SCIENCE IN APPLIED MATHEMATICS**

from the

**NAVAL POSTGRADUATE SCHOOL
December 2010**

Author: Omar J. Wheatley

Approved by: I. Michael Ross
Thesis Co-Advisor

Wei Kang
Thesis Co-Advisor

Knox T. Millsaps
Chairman, Department of Mechanical and Aerospace Engineering

THIS PAGE INTENTIONALLY LEFT BLANK

ABSTRACT

Pseudospectral methods are used to efficiently solve complex, non-linear optimal control problems and can be used to develop rapid and robust control solutions in astrodynamics applications. With the renewed efforts in resuming future manned missions to the moon or near-earth asteroids, fuel optimal flight trajectories are desired in order to alleviate the need for overestimates in fuel carried onboard, which has a negative impact on the overall spacecraft design.

This thesis uses a pseudospectral optimal control solver, DIDO©, to solve for a fuel optimal moon-to-earth trajectory using only the auxiliary engines of the Orion Crew Exploration Vehicle (CEV) for the entire mission. Additionally, higher-order necessary conditions are examined to test the extremality of the computed solution. Singular arcs that appear in a main engine variable thrust, fuel optimal trajectory are examined by applying the Bellman Pseudospectral method. The feasibility of using the CEV auxiliary engines in place of the main engines for the singular arc maneuver is also investigated.

THIS PAGE INTENTIONALLY LEFT BLANK

TABLE OF CONTENTS

I.	INTRODUCTION.....	1
A.	BACKGROUND	1
B.	SCOPE OF THE RESEARCH.....	1
II.	EQUATIONS OF MOTION.....	5
A.	INTRODUCTION.....	5
B.	DEFINING THE REFERENCE FRAME (J2000)	5
C.	JPL HORIZONS DATA.....	9
D.	THE IMPORTANCE OF ACCURACY.....	14
E.	EQUATIONS OF MOTION.....	17
1.	The Restricted Two-Body Problem.....	17
2.	The n-Body Problem.....	19
3.	Equations of Motion for Moon to Earth Return Mission	20
III.	OPTIMAL CONTROL THEORY.....	25
A.	THE OPTIMAL CONTROL PROBLEM.....	25
B.	DERIVATION OF THE NECESSARY CONDITIONS USING THE CALCULUS OF VARIATIONS	26
C.	PONTRYAGIN'S PRINCIPLE.....	27
D.	THE SWITCHING FUNCTION.....	30
E.	NECESSARY CONDITIONS FOR SINGULAR ARC OPTIMALITY ..	31
F.	TRANSVERSALITY CONDITION	32
G.	SUMMARY OF NECESSARY CONDITIONS FOR OPTIMALITY	33
H.	GENERIC PROBLEM FORMULATION.....	33
IV.	USING DIDO©	35
A.	INTRODUCTION.....	35
B.	PROBLEM FORMULATION IN DIDO©.....	35
C.	BEST PRACTICES	37
1.	Scaling.....	37
2.	LGL Nodes.....	38
3.	Providing an Initial Guess.....	38
D.	VERIFICATION AND VALIDATION.....	41
1.	Examining Initial Output.....	41
2.	Checking Necessary Conditions for Optimality.....	42
3.	Checking Feasibility.....	42
4.	Comparison to Previous Studies.....	44
V.	AUXILIARY ENGINE FOR MOON TO EARTH RETURN MISSION	45
A.	THE MINIMUM TIME, FUEL FREE PROBLEM.....	46
1.	Problem Formulation	46
2.	Results and Analysis	47
a.	<i>Feasibility of the Solution.....</i>	<i>50</i>
b.	<i>Verification of the Optimality of the Solution.....</i>	<i>55</i>

3.	Conclusion for Minimum Time Case	58
B.	THE MINIMUM FUEL, FIXED TERMINAL TIME PROBLEM.....	59
1.	Problem Formulation	59
2.	Results and Analysis	60
a.	<i>Feasibility of the Solution</i>	63
b.	<i>Verification of the Optimality of the Solution</i>	68
C.	CONCLUSIONS FOR USE OF AUXILIARY ENGINES FOR RETURN MISSION	76
VI.	MAIN ENGINE SINGULAR ARC ANALYSIS.....	77
A.	PROBLEM FORMULATION	82
B.	TH1 RESULTS.....	82
C.	TH2 RESULTS.....	92
D.	TH3 RESULTS.....	97
E.	FEASIBILITY OF USING AUXILIARY ENGINES FOR SINGULAR ARC MANEUVER	101
F.	CONCLUSIONS	103
APPENDIX A.	SINGULAR ARC NECESSARY CONDITIONS.....	105
APPENDIX B.	END-POINT TRANSVERSALITY CONDITION.....	109
	LIST OF REFERENCES	111
	INITIAL DISTRIBUTION LIST	113

LIST OF FIGURES

Figure 1.	Thrust Profile Using Main Engine.....	3
Figure 2.	Heliocentric Reference Frame (From Vallado, 1997)	6
Figure 3.	Earth Centered Inertial Reference Frame (From Vallado, 1997)	7
Figure 4.	Precession and Nutation (From Vallado, 1997).....	9
Figure 5.	Sun Position Error wrt Moon.....	13
Figure 6.	Earth Position Error wrt Moon	13
Figure 7.	Effects of Additional Gravitational Bodies on Displacement.....	16
Figure 8.	Effects of Additional Gravitational Bodies on Velocity.....	16
Figure 9.	2-body Dynamic Model	18
Figure 10.	Three-Body Geometry (After Vallado, 1997)	19
Figure 11.	J2000 Sun and Moon Centered Frame (From Yan et al., 2010)	21
Figure 12.	Hamiltonian as a function of \mathbf{u} only (From Ross, 2009)	29
Figure 13.	H as a function of \mathbf{T} only (From Ross, 2009)	30
Figure 14.	Recalculation of Azimuth Control Angle	40
Figure 15.	Recalculation of Elevation Control Angle.....	41
Figure 16.	Bellman Principle.....	43
Figure 17.	Thrust Profile	48
Figure 18.	Azimuth Control Profile	49
Figure 19.	Elevation Control Profile	49
Figure 20.	Displacement Vector.....	50
Figure 21.	Tangential Velocity Vector.....	51
Figure 22.	Fuel Consumption.....	51
Figure 23.	Semi-major Axis	54
Figure 24.	Eccentricity	54
Figure 25.	Inclination	55
Figure 26.	Hamiltonian Evolution.....	56
Figure 27.	Co-state (λ_m) Evolution.....	56
Figure 28.	Primer Angle.....	57
Figure 29.	Switching Function	58
Figure 30.	Thrust Control Structure	61
Figure 31.	Azimuth Control Angle.....	62
Figure 32.	Elevation Control Angle	62
Figure 33.	Fuel Consumption.....	63
Figure 34.	Displacement State Trajectory	64
Figure 35.	Velocity State Trajectory	65
Figure 36.	Semi-major Axis With Respect to Moon Centered Frame	66
Figure 37.	Eccentricity With Respect to Moon Centered Frame	67
Figure 38.	Inclination With Respect to Moon Centered Frame	67
Figure 39.	Hamiltonian Evolution.....	69
Figure 40.	Co-state (λ_m) Evolution.....	69
Figure 41.	Thrust and Switching Function.....	70
Figure 42.	Derivatives of the Switching Function During Singular Arc.....	71

Figure 43.	Generalized Legendre-Clebesch Condition During Singular Arc	71
Figure 44.	Generalized Legendre-Clebesch Condition Over Entire Trajectory	72
Figure 45.	First TEI Burn	73
Figure 46.	Second TEI Burn	73
Figure 47.	Third TEI Burn	74
Figure 48.	Displacement Error	75
Figure 49.	Velocity Error	75
Figure 50.	Bellman Curve and Segment	78
Figure 51.	Three Time Horizons Around Original Main Engine Singular Arc	80
Figure 52.	Thrust Trajectories for TH1	83
Figure 53.	Azimuth Angle Trajectories for TH1	84
Figure 54.	Elevation Angle Trajectories for TH1	84
Figure 55.	Hamiltonian Evolution (TH1)	85
Figure 56.	End-point Transversality Condition (TH1)	86
Figure 57.	Primer Angle (TH1)	86
Figure 58.	Switching Function For Coarse Guess Solution	87
Figure 59.	Switching Function for 2-Point Guess Solution	87
Figure 60.	Fourth Time Derivative of Switching Function for Coarse Guess Solution	88
Figure 61.	Fourth Time Derivative of Switching Function for 2-Point Guess Solution	88
Figure 62.	Generalized Legendre-Clebesch Condition for Coarse Guess Solution	89
Figure 63.	Generalized Legendre-Clebesch Condition for 2-Point Guess Solution	89
Figure 64.	Displacement State (\bar{r}) Trajectories for TH1	90
Figure 65.	Velocity State (\bar{v}) Trajectories For TH1	91
Figure 66.	Fuel Consumption for TH1	92
Figure 67.	Thrust Trajectories for TH2	93
Figure 68.	Azimuth Angle Trajectories for TH2	94
Figure 69.	Elevation Angle Trajectories for TH2	94
Figure 70.	Displacement State (\bar{r}) Trajectories for TH2	95
Figure 71.	Velocity State (\bar{v}) Trajectories for TH2	96
Figure 72.	Fuel Consumption for TH2	96
Figure 73.	Thrust Trajectories for TH3	98
Figure 74.	Azimuth Angle Trajectories for TH3	98
Figure 75.	Elevation Angle Trajectories for TH3	99
Figure 76.	Displacement State Trajectories (TH3)	100
Figure 77.	Velocity Trajectories (TH3)	100
Figure 78.	Fuel Consumption (TH3)	101
Figure 79.	Auxiliary Engine Thrust Profile (TH1)	102

LIST OF TABLES

Table 1.	Moon-to-Sun Coefficients	11
Table 2.	Moon-to-Earth Coefficients	12
Table 3.	DIDO vs. Propagated Solution	52
Table 4.	Effects of the Bellman PS Technique	53
Table 5.	Fuel Consumption Comparison	68
Table 6.	TH1 Fuel Consumption.....	83
Table 7.	TH2 Fuel Consumption.....	97
Table 8.	Fuel Consumption for TH3	101
Table 9.	Fuel Consumption Comparison Between Main Engine and Auxiliary Engines Over Singular Arc	103

THIS PAGE INTENTIONALLY LEFT BLANK

ACKNOWLEDGMENTS

I would be remiss in not acknowledging the various people who have provided the inspiration, guidance, and moral support in helping me complete this thesis. First of all, I would like to express my gratitude to my thesis advisor, Dr. Mike Ross, for the wonderful introduction into the subject of optimal control and for agreeing to take me on as a thesis student. Thank you for the constant reminders for “analysis, analysis, and analysis!” To Dr. Wei Kang, my co-advisor, and the rest of the Mathematics Department at NPS, I thoroughly enjoyed the instruction and mentorship I received from you. Also, a special thanks goes out to all the professors who I have had the pleasure of working with within the Space Systems curriculum.

I would also like to thank Dr. Hui Yan and Dr. Chi Gong for their direct assistance on this thesis. It was a pleasure working with you both. I hope that this humble work contributes to the volumes you have and likely will continue to add to this field of research.

On the actual day to day battles with problem formulation and frustrating coding issues, I would like to thank Dr. Mark Karpenko for being the closest target of opportunity for my questions. I definitely owe you for the hours I probably took you away from your own research. Thanks also to Dr. Pooya Sekhavat for your insight and guidance in the singular arc problem.

Finally, I would like to thank the one person who is my inspiration and my guiding light and has been my strongest, steadfast supporter. To my wife and best friend, Patricia, thank you for encouraging me in my graduate studies and for your patience through the struggles along this journey. I never could have completed this tour without your continuing love and support. I also want to give thanks to my son, Isaac, who made his appearance in the world only ten months prior to my graduation. You have brought further meaning into my life and I aspire to be a better husband and father because of you. And thanks to God for making all things possible and for providing the countless blessings in my life.

THIS PAGE INTENTIONALLY LEFT BLANK

I. INTRODUCTION

A. BACKGROUND

The NASA Orion Crew Exploration Vehicle (CEV) program has more stringent safety requirements as compared to the Apollo missions of the 1960s and 1970s. One such requirement is for “anytime return” of the spacecraft in the event of a mission abort scenario. The increased safety margins that need to be incorporated into the spacecraft design begin to form a competing set of requirements. The design of spacecraft, whether manned or unmanned, is primarily driven by the mass of fuel carried onboard to perform maneuvers while performing its mission. This, in turn, drives the total mass of the spacecraft, which further constrains the design for mission essential equipment and can heavily influence the design and/or selection of the launch vehicle. Excess safety margins should be avoided, however, in order to maximize mission effectiveness.

The application of optimal control theory to astrodynamics applications allows for designers to generate engineering solutions that maximize desirable performance characteristics as well as minimizing the need for excess design margins. Current design practices may unwittingly limit the solutions being created by enforcing seemingly practical constraints. As the spacecraft design matures, clearly there is a need to start imposing design constraints due to the available technology, product specifications, and material. However, early in the design it is possible to find “best” solutions by limiting the number of constraints imposed on the design and mathematically validating the solutions using existing optimal control theory. The tools for solving complex optimal control problems allow for rapid and robust solutions and straightforward methods are available for ascertaining their feasibility.

B. SCOPE OF THE RESEARCH

This thesis investigated the feasibility of using solely the lower thrust auxiliary engines of the Orion CEV for return to earth from low lunar orbit. Using DIDO©, which utilizes MATLAB to solve complex, non-linear optimal control problems, solutions were

generated which demonstrate the existence of trajectories which would allow the spacecraft to return using only the auxiliary engines while meeting specific mission timeline and fuel consumption requirements. Furthermore, the solutions generated are shown to meet the necessary conditions of optimality by applying Pontryagin's Theory. While there exists a range of possible solutions, two significant solutions are presented: (1) the absolute minimum time required for the maneuver with no constraint on fuel, and (2) the minimum fuel required to reach the given final boundary conditions within 48 hours.

The first case is shown primarily to show the absolute lower limit on time required for the maneuver with the given engine characteristics and the dynamics of the problem. The necessary conditions for optimality of this solution are shown and a feasibility analysis is conducted to check the solutions. The feasibility of the control solution is conducted by the application of the Bellman technique. While the Bellman technique is not shown for the second, minimum fuel case, it demonstrates a method to verify the fidelity of the generated solutions and determine if the solution is "flyable" given a nominal set of discrete control points. The second case shows that the auxiliary engines can be used to complete the entire moon-to-earth Trans-earth Injection (TEI) maneuver sequence and still meet the 48-hour time requirement and use less fuel than the capacity of the Orion's fuel tank. In all cases, the necessary conditions for optimality are demonstrated using Pontryagin's Hamiltonian Minimization Condition (HMC) and where singular arcs appear in the trajectory, further analysis is performed to show optimality.

Another problem investigated in this thesis is the control of the singular arc segment of a previously determined DIDO© solution using the CEV main engines. The main engine solution resulted in the return trajectory consisting of three separate TEI burns. The first and third burns are maximum thrust burns, known as bang-bang maneuvers. The first burn raises the apoapsis of the low lunar orbit, while the final burn provides the necessary velocity to escape the moon's gravity on its way towards earth. The middle burn is given as a finite burn of varying thrust where the spacecraft conducts a plane change maneuver. A study of the high thrust singular arc solution was conducted in order to attain more in-depth details of the control trajectory in order to determine the

feasibility of using the auxiliary engines to conduct the singular burn segment of the high thrust return trajectory. Figure 1 shows the thrust profile for the minimum fuel, fixed time return solution using the Orion CEV main engines found by Yan et al. (Yan, Gong, Park, Ross, & Souza, 2010).

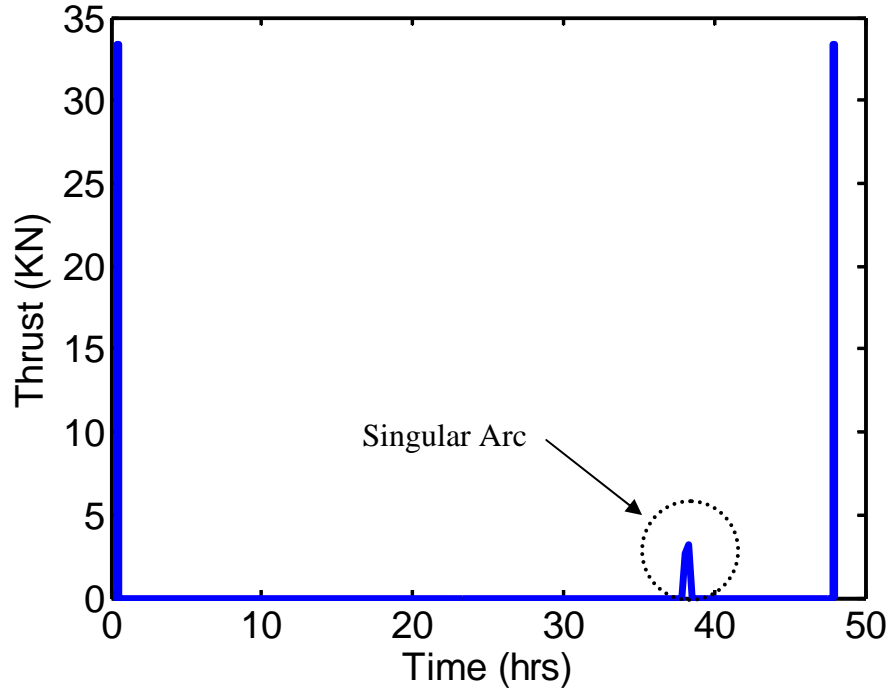


Figure 1. Thrust Profile Using Main Engine

THIS PAGE INTENTIONALLY LEFT BLANK

II. EQUATIONS OF MOTION

A. INTRODUCTION

For interplanetary trajectories, the two body problem no longer suffices as the spacecraft will pass through areas of varying gravitational influence as it gets further away from one body and gets closer to another. Even outside the sphere of influence of a particular body, the gravitational acceleration of that body may provide a minimal, but influential gravitational affect, often referred to as a gravitational perturbation. This chapter first defines the specific reference frame used for each case in this thesis. Secondly, it describes the gathering of ephemerides data on the gravitational bodies which have significant effect on the spacecraft trajectory which is ultimately used in setting up the dynamics of the moon-earth return mission. Finally, a brief description of the dynamics is given, followed by an example of why the problems require $n=4$ for moon-earth return missions.

B. DEFINING THE REFERENCE FRAME (J2000)

If one has to move from one specific location to another, one has to have good knowledge of the current position as well as an accurate description or knowledge of the intended final position. In common terms, it is called navigation. On the surface of the earth, the art of navigation is generally simple. Barring any obstacles, one simply takes the shortest distance between two points (which are fixed) and travels along the line that connects the two points. This is done by establishing a reference frame. Assuming that the travel is in only two dimensions, a planar reference frame can be used. Longer distances on the surface of the earth can be referenced to the surface of a sphere. Despite the rotations of the earth, the two dimensional traveler need only stay on the line connecting the two points. The reference frame, whether a flat plane or surface of the sphere is considered inertial since it is not accelerating with respect to the traveler.

Depending on the specific application, such as interplanetary space missions or tracking satellites in orbit, a number of different reference frames are used. For rough

calculations, the reference systems used can use an object's center of mass as the center. However, for spaceflight in the vicinity of the earth and moon, it might be useful to use the earth-moon *barycenter*, or system center of mass. Synodic systems are also used which are systems that rotate about the barycenter. In synodic coordinate systems, it is assumed that the rotation about the barycenter is with constant velocity with respect to an inertial frame.

The *Heliocentric Coordinate System (XYZ)* is a sun centered system with the primary axis, X , pointed at the vernal equinox. It is a right handed system with respect to the direction of earth's orbit around the sun with Z perpendicular to the ecliptic plane. With the correct transformations, this coordinate system could be converted into a *synodic* coordinate system, by using the barycenter of the solar system which is a point slightly off from the geometric center of the sun.

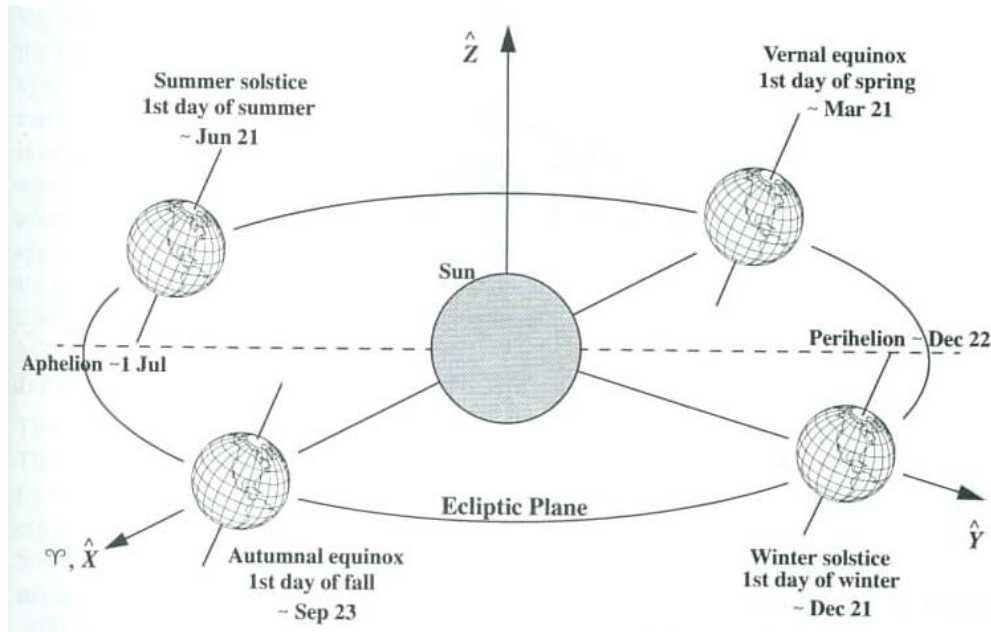


Figure 2. Heliocentric Reference Frame (From Vallado, 1997)

A commonly used coordinate system in astrodynamics is called the *Geocentric Equatorial Coordinate System (IJK)* which is a non-rotating system with the primary

axis, I , pointed at the vernal equinox. The J axis is 90 degrees to the east and the K axis points out of the earth's north pole. This system is also known as the *Earth Centered Inertial (ECI)* system. The ECI system in actuality does move over time due to effects such as *precession* and *nutation*. The J2000 system is essentially the ECI system at a fixed epoch, previously noted. This is considered an inertial frame from which calculations known as *reduction formulas* can be used to advance (or regress) to another epoch.

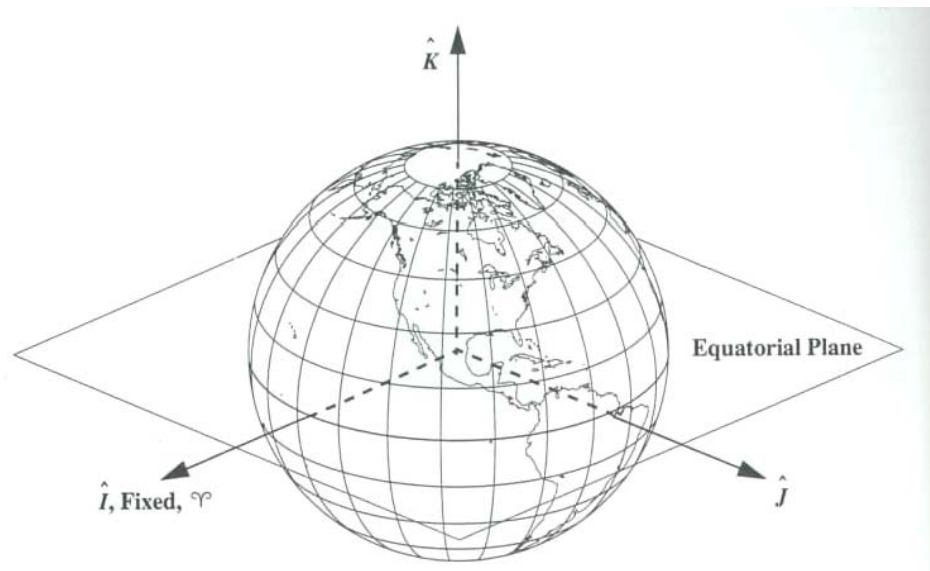


Figure 3. Earth Centered Inertial Reference Frame (From Vallado, 1997)

The problem with space travel is in determining and characterizing an inertial reference frame, since by nature all the objects in the solar system are in a state of continual motion, and in most cases non-uniform motion due to the effects of gravitational forces between them. For short time spans, it may suffice to assume an inertial frame with the earth at its center; however the nonuniform motion of the earth and other solar system bodies have an increasingly perturbing effect over time. Therefore, to accurately determine the position of a body (celestial body or spacecraft) traveling through the solar system, one has to have a method to accurately determine the locations of all the gravitational bodies, or at least the ones which have the most

significant effect on the motion of that body. The positions of the solar system bodies can be determined by observation and the future positions can be determined, assuming the motions are well characterized, at a future time.

For consistency, it has been useful to designate a specific time, or epoch, as a reference time with which the reference frame used for navigation purposes can be advanced or rotated. The current system in use today is called J2000. The J2000 epoch is specified to be, January 1, 2000 at 11:59:27.816 TAI (International Atomic Time), or about noon UT (Universal Time). Therefore, J2000 refers to a specific epoch from which to attach a coordinate system as a basis for all celestial observations (Vallado, 1997). Typically, an ECI reference frame is used as the basis. If a moon-centered inertial frame was desired, then with the proper transformation, the frame could be translated from the earth to the moon's location at the J2000 epoch.

In addition to planetary motion about the sun, the Earth's position and orientation with respect to the J2000 ECI frame varies due to gravitational interactions with other bodies in the solar system, but primarily due to the Moon and Sun. The four primary transformations which must be made are for *precession*, *nutation*, *sidereal time*, and *polar motion*. Precession results from perturbations from the Sun, Moon, and planets and it changes the orientation of the ecliptic with respect to the J2000 frame. The reduction formulas for precession allow for the calculation of the *mean equator of date* from the *mean equator at epoch (J2000)*. Nutation is largely caused by the moon and is the lengthiest transformation, consisting of over 100 trigonometric terms and is a periodic perturbation. Taking into account the effects of nutation transforms the *mean equator of date* into the *true equator of date*. The third transformation, sidereal time, transforms the non-rotating true of date frame to the *Earth-fixed* coordinate system. Finally, polar motion accounts for the changing location of the North Pole. The motion of the North Pole follows a circular spiral pattern and has a maximum variation of about only 9 meters in any direction (Vallado, 1997).

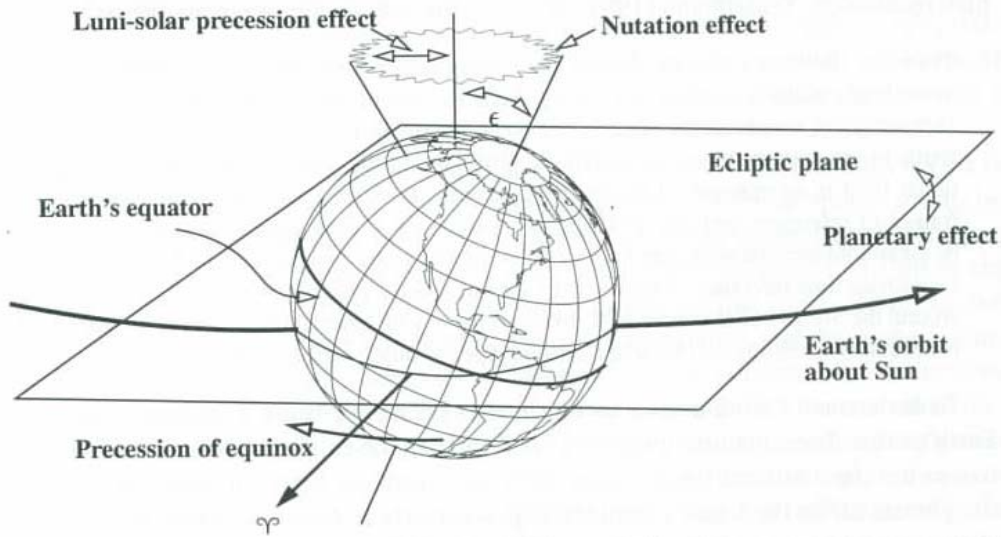


Figure 4. Precession and Nutation (From Vallado, 1997)

The problems studied in this thesis use a J2000 moon-centered frame of reference since the spacecraft originates in close proximity to the moon. In this way, the moon is the primary gravitational body exerting a force on the spacecraft, while other celestial bodies, including the earth, exert a perturbing force on the spacecraft.

C. JPL HORIZONS DATA

The Jet Propulsion Lab (JPL) HORIZONS on-line system provides accurate ephemeris data for solar system objects to include 538186 asteroids, 3066 comets, 170 planetary satellites, 8 planets, the Sun, L1, L2, select spacecraft, and system barycenters (Jet Propulsion Laboratory). Using the web interface, ephemeris data was collected for earth, sun, Mars, and Venus as target bodies with the origin body as the moon. The ephemeris data was collected in the form of position (X, Y, Z) and velocity (VX, VY, VZ) vectors from the moon to the target bodies in the J2000 frame covering a time span of ten days starting at midnight on April 2, 2024, until midnight on April 12, 2024, in increments of one minute. The vectors were with respect to the ecliptic and mean equinox of the J2000 epoch.

In order to have access to accurate position vectors to the target bodies at any time, the relative motion of the target bodies can be characterized as a smooth function of time. In this study the Matlab function, *polyfit*, was used to be able to compare the accuracy of the data used by Yan et al., who used the same function (Yan et al., 2010). Even though the data points are very close together in comparison to the total duration, it is desired to create a smooth function in order to determine the position vectors between the discrete points. The goal for the overall project is to ensure that the accuracy of the position of the spacecraft and the celestial bodies is within one kilometer. At spacecraft interplanetary velocities, one minute is actually a long duration. Take for example a spacecraft travelling at a velocity of 7.7 km/sec. In one minute, the spacecraft has travelled 462 km.

The *polyfit* function in Matlab interpolates between the data points by fitting a polynomial of specified order between the data points, x , by solving for $P(x)$ in a least squares approximation. In order to minimize calculation errors when solving for the state vectors using polynomials, the order of the polynomial should be minimized but balanced against desired accuracy. For the position vectors, an accuracy on the order of one meter was desired and was accomplished by using polynomials of degree $n = 12$. The coefficients for the position and velocity vector polynomials are given in TABLES 1 and 2. The position and velocities of the bodies can then be determined simply by applying the following equation, where P applies to either the Earth or Sun position or velocity at the specific time.

$$P = \sum_{k=0}^n a_k t^{n-k}, t = \text{days from start of epoch} \quad (1.1)$$

Figures 5 and 6 show the polynomial fitting errors for the sun and earth positions taken from the Horizons ephemeris database; increasing the order of the polynomial did not result in an increase in accuracy.

a_k	Coef. Of X_s	Coef. Of Y_s	Coef. Of Z_s
a_0	-0.000000118999244	0.000000051363297	0.000000031235814
a_1	0.000007535524407	-0.000001813763037	-0.000001195202237
a_2	-0.000193935822284	0.000008603741722	0.000010044635361
a_3	0.002551670749774	0.000411412069435	0.000153255992774
a_4	-0.018494484604858	-0.006223615168335	-0.002874344419063
a_5	0.096450588487681	0.029031951945015	0.013126497005896
a_6	-0.48791534224999	-0.245917701266308	-0.120333635274365
a_7	-1.80818923330034	1.47692100379431	0.853535973780927
a_8	-0.265672427554903	45.0362084788201	24.5131154837513
a_9	844.693396988081	58.7951095944313	21.8949581954112
a_{10}	-18090.2205317641	-13291.5876493955	-6819.90286281822
a_{11}	-620971.753444483	2278260.71520781	986430.475751975
a_{12}	145573547.288563	31280330.2617121	13595979.9986218
a_k	Coef. Of VX_s	Coef. Of VY_s	Coef. Of VZ_s
a_0	0.0000000000000876	0.00000000000134	0.000000000000705
a_1	-0.000000000035468	-0.000000000085042	-0.000000000045286
a_2	0.000000000400585	0.000000002222538	0.000000001198091
a_3	0.000000001838394	-0.000000030441403	-0.000000016612406
a_4	-0.000000065594787	0.000000235708378	0.000000130050108
a_5	0.000000409285064	-0.000001185558201	-0.000000656321966
a_6	-0.000002045604444	0.000005206853674	0.000002889371779
a_7	0.000016616317898	-0.000004789036079	-0.000003062311659
a_8	0.000138708440174	-0.000043909789614	-0.000027726262746
a_9	-0.000029838214692	-0.002134339196159	-0.001160538240461
a_{10}	-0.029299757820009	-0.002008086029233	-0.000742891068896
a_{11}	0.418744847880383	0.307664738921479	0.157862474895167
a_{12}	7.18717422343139	-26.3687571226232	-11.417018798621

Table 1. Moon-to-Sun Coefficients

a_k	Coef. Of X_E	Coef. Of Y_E	Coef. Of Z_E
a ₀	-0.000000120465923	0.000000052002009	0.000000031622897
a ₁	0.000007628381257	-0.000001836460056	-0.000001210064749
a ₂	-0.000196325470881	0.000008719042669	0.000010172147384
a ₃	0.002583117149928	0.000416339321152	0.000155085108346
a ₄	-0.018722521992485	-0.006298978841759	-0.002909197790503
a ₅	0.097640301438211	0.029382066258909	0.013284992773766
a ₆	-0.493926539477772	-0.248911414493782	-0.121800436698966
a ₇	-1.829533259726210	1.49341919298633	0.863311162886425
a ₈	-0.794558172099937	45.4263751279875	24.7436327304441
a ₉	821.8742589348	173.57690416087	71.6075269802601
a ₁₀	3527.10796729054	-8812.29966356204	-4891.3375699089
a ₁₁	-82856.1140443406	-31492.1606624715	-14834.6697711603
a ₁₂	-124996.868758181	310520.160006487	172373.588579813
a_k	Coef. Of VX_E	Coef. Of VY_E	Coef. Of VZ_E
a ₀	0.000000000000886	0.000000000001357	0.000000000000714
a ₁	-0.000000000035905	-0.000000000086088	-0.000000000045843
a ₂	0.000000000405515	0.000000002249876	0.000000001212828
a ₃	0.000000001860981	-0.000000030815843	-0.000000016816749
a ₄	-0.000000066401389	0.000000238607693	0.000000131649824
a ₅	0.000000414317781	-0.000001200141256	-0.000000664395353
a ₆	-0.000002070757641	0.000005270899291	0.000002924912661
a ₇	0.000016820396625	-0.000004848188830	-0.000003100088483
a ₈	0.000140364902077	-0.000044357520552	-0.000028027227578
a ₉	-0.000005874216492	-0.002153003638943	-0.001171523674705
a ₁₀	-0.028507056638794	-0.005993158263952	-0.002468810366489
a ₁₁	-0.081656401977571	0.203977384449362	0.113219690991780
a ₁₂	0.958983966914624	0.364493769544924	0.171698170715951

Table 2. Moon-to-Earth Coefficients

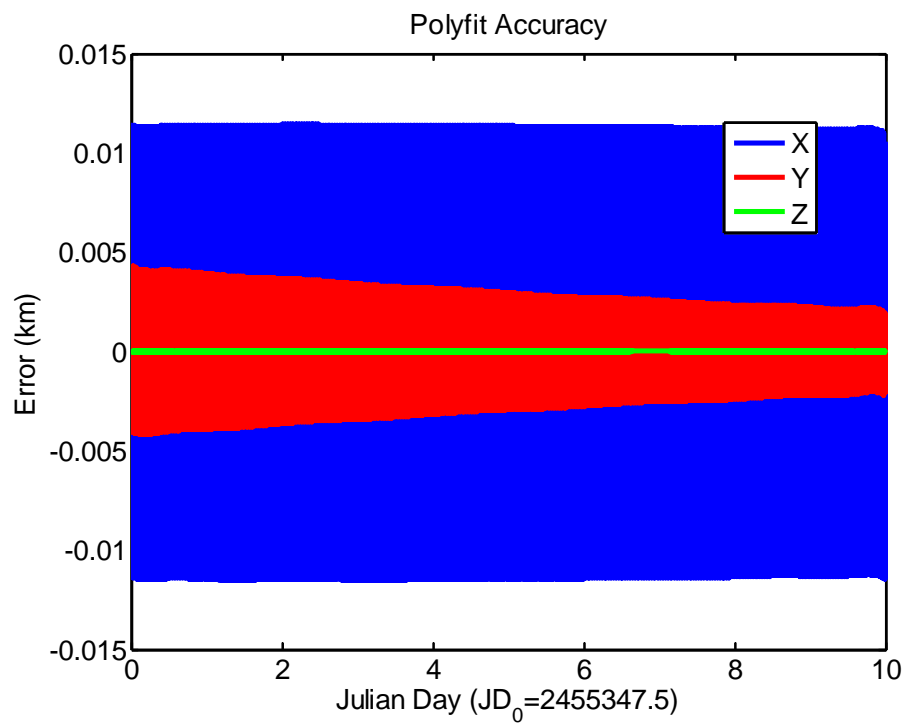


Figure 5. Sun Position Error wrt Moon

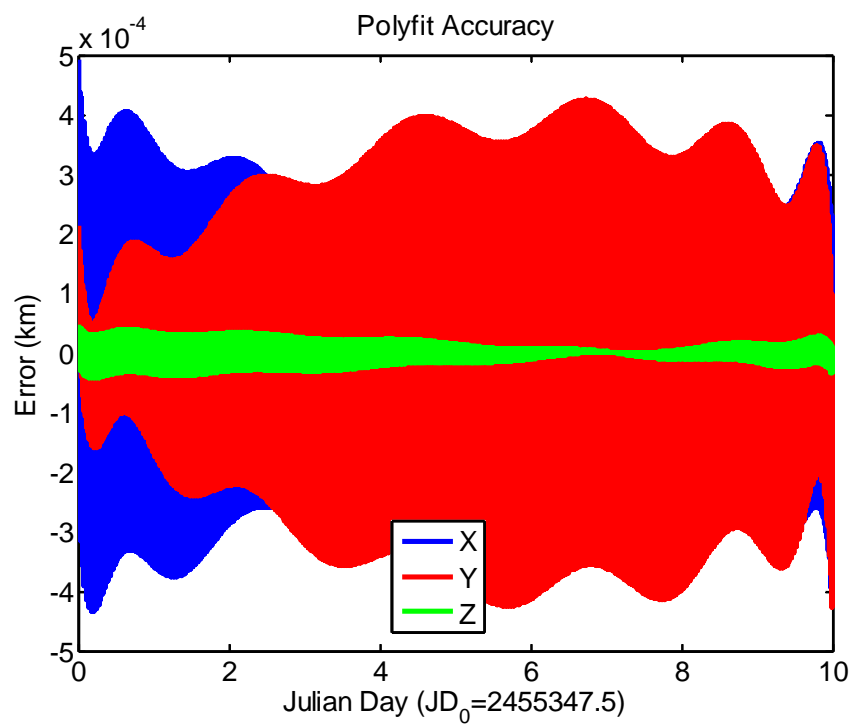


Figure 6. Earth Position Error wrt Moon

D. THE IMPORTANCE OF ACCURACY

One might ask why it is so important to take into account what seems like very small variations and perturbations. Obviously, over long periods of time, the effects of the perturbations would increase, but these could be taken into account using frequent observations and updates to spacecraft navigation systems and simply make course adjustments during flight. The greatest constraint on spacecraft is typically its mass, due to launch constraints imposed by launch vehicles. A portion of this mass is fuel which the spacecraft requires for orbit transfers, station keeping, and attitude control. While the spacecraft could conceivably make correction maneuvers in flight, it comes at a cost of fuel. Any additional fuel to a spacecraft comes at a cost to allocated mass in other systems. For interplanetary missions, especially for future manned exploration missions, the payload and support systems are critical to maximize mission duration and ultimately mission viability. In practice, the spacecraft design should minimize the amount of fuel required to conduct its mission. Therefore, for design purposes, it is important to take into account additional gravitational effects that act on the spacecraft.

If the target body's motion, such as the Moon or Mars, is very accurately determined, then optimal trajectories and thrust regimes could be used without the need for correction maneuvers during transit. An analogy might be a bullet travelling downrange to a target at a distance of 1,000 meters. If the bullet's initial trajectory is off by 0.1 degrees, it will only miss the center of the target by 1 millimeter. However, suppose a spacecraft travelling in a straight line, travels a distance of 80,000,000 kilometers, the rough straight line distance between Earth's orbit around the Sun and Mars' orbit. A trajectory error of the same, 0.1 degrees will have the spacecraft miss its intended target by over 120 kilometers. Considering the great distance travelled, this may not seem like a significant number, however when trying to hit the target on the mark, with minimum fuel, this is indeed a considerable error. This highlights the need for a very accurate description of the motion of the planetary bodies and this primarily relies on an accurate accounting of time from the inertial reference frame time.

For a spacecraft returning to Earth from the Moon, in order to minimize fuel, optimal control trajectories are being created such that the spacecraft has a 1 km window for earth orbit insertion. This means that in order for the trajectory to be accurately designed, the spacecraft dynamics need to be of very high order of accuracy. It can be shown that for a moon-earth return trajectory, the perturbation effects of the Earth and Sun must be taken into account in order to achieve the accuracy required. In order to demonstrate this fact, a portion of the trajectory from Yan et al. moon to earth trajectory using the CEV main engines was investigated to show the effects of changing the number of bodies included in the dynamics equations (Yan et al., 2010). The segment investigated has the initial position immediately following the first TEI maneuver and the target position immediately prior to the second TEI maneuver. The trajectory was propagated using the MatLab *ode45* function and allowed to propagate until the time of the second burn maneuver. Starting with a simple restricted two-body dynamics equation using only the Moon's gravity (Body 2), successive runs were conducted, each adding the gravitational effects of the Earth (Body 3), Sun (Body 4), and finally Mars (Body 5). The time-varying positions of the earth and sun with respect to the moon were taken into account as described previously as well as the governing equations of motion as described in the following section. The initial conditions are as follows:

$$\bar{X}_0 = \begin{bmatrix} x_0 \\ y_0 \\ z_0 \\ v_{x0} \\ v_{y0} \\ v_{z0} \end{bmatrix} = \begin{bmatrix} 406.4091528635830 & \text{km} \\ 255.0671214283607 & \text{km} \\ -1,824.834644517191 & \text{km} \\ 1.445606181317849 & \text{km/sec} \\ -1.651932481918282 & \text{km/sec} \\ -0.274681204800144 & \text{km/sec} \end{bmatrix}$$

Figures 7 and 8 show that the four-body dynamics, which includes the moon, earth and sun, satisfy the accuracy requirements while the addition of the fifth body do not contribute a significant effect on the trajectory, therefore its effect need not be included.

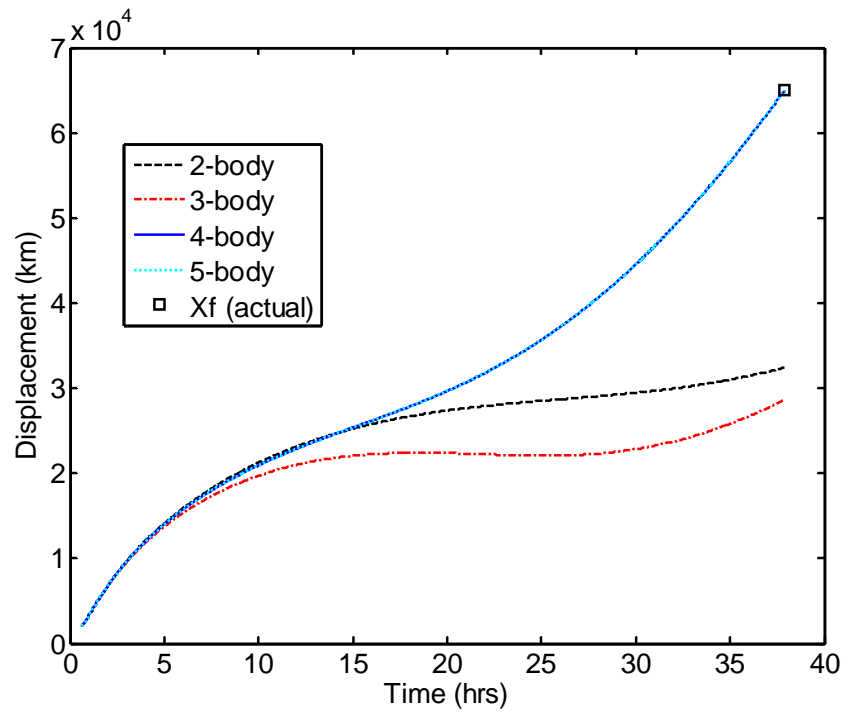


Figure 7. Effects of Additional Gravitational Bodies on Displacement

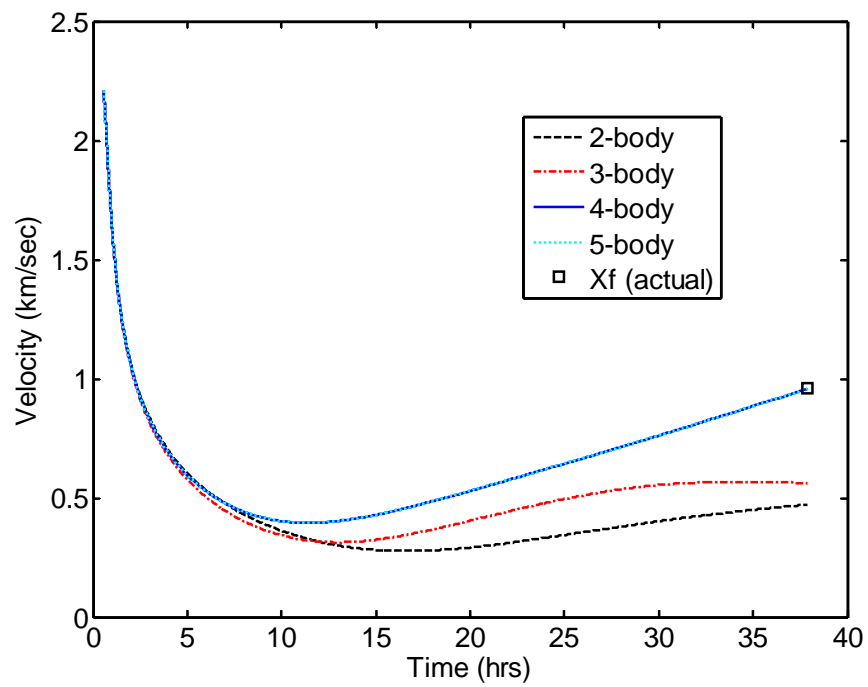


Figure 8. Effects of Additional Gravitational Bodies on Velocity

E. EQUATIONS OF MOTION

1. The Restricted Two-Body Problem

In the restricted two-body dynamic model, the mass of the spacecraft is deemed negligible and equation of motion is:

$$\ddot{\vec{r}} = -\frac{GM}{r^2} \left(\frac{\vec{r}}{r} \right) \quad (1.2)$$

This equation describes the force of attraction between two bodies, namely a planet (moon or sun) and a spacecraft where G is the universal gravitational constant, M is the mass of the large body, m is the mass of the spacecraft, and r is the position vector indicated by the negative sign to be from the spacecraft to the large body (Figure 9). For generality, the origin of the inertial reference frame will not be located at the center of the large mass. Therefore, the position vector r will be the difference between the vectors from the origin to each of the bodies as follows:

$$\vec{r} = \vec{r}_{SC} - \vec{r}_M \quad (1.3)$$

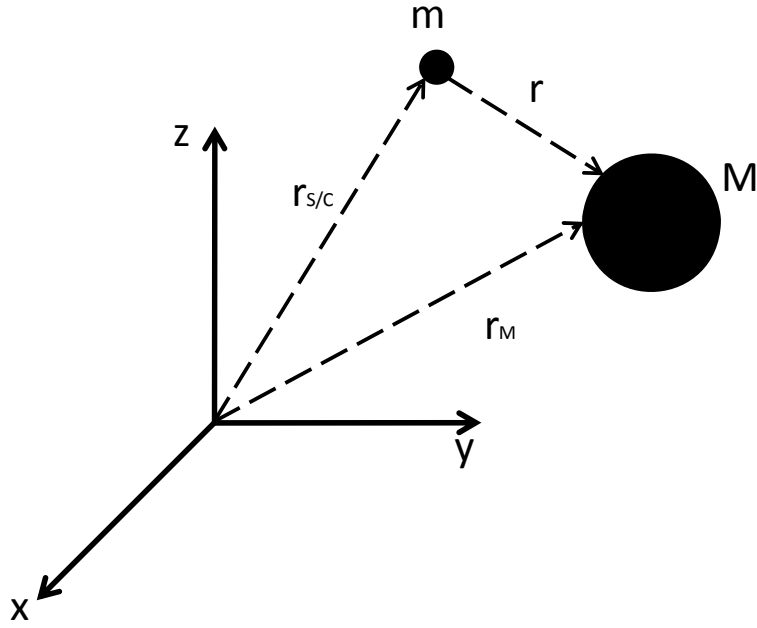


Figure 9. 2-body Dynamic Model

Since the data from HORIZONS is in XYZ vector format, the r vector is converted into Cartesian coordinates, substituting μ_M for GM . Three equations of motion are generated, one for each axis of motion where:

$$\begin{aligned}
 \ddot{x} &= -\frac{\mu_M x}{(x^2 + y^2 + z^2)^{3/2}} \hat{i}, & x &= x_{SC} - x_M \\
 \ddot{y} &= -\frac{\mu_M y}{(x^2 + y^2 + z^2)^{3/2}} \hat{j}, & y &= y_{SC} - y_M \\
 \ddot{z} &= -\frac{\mu_M z}{(x^2 + y^2 + z^2)^{3/2}} \hat{k}, & z &= z_{SC} - z_M
 \end{aligned} \tag{1.4}$$

2. The n-Body Problem

From the point of view of an inertial observer, the restricted n-body equation of motion with respect to the primary body is shown in Equation (2.5) below. Figure 10 shows a diagram of the n-body geometry when there are only three bodies (n=3).

$$\ddot{\vec{r}}_{1,2} = -\frac{\mu_1 \vec{r}_{1,2}}{r_{1,2}^3} - \sum_{j=3}^n \mu_j \left(\frac{\vec{r}_{j,2}}{r_{j,2}^3} + \frac{\vec{r}_{1,j}}{r_{1,j}^3} \right) \quad (1.5)$$

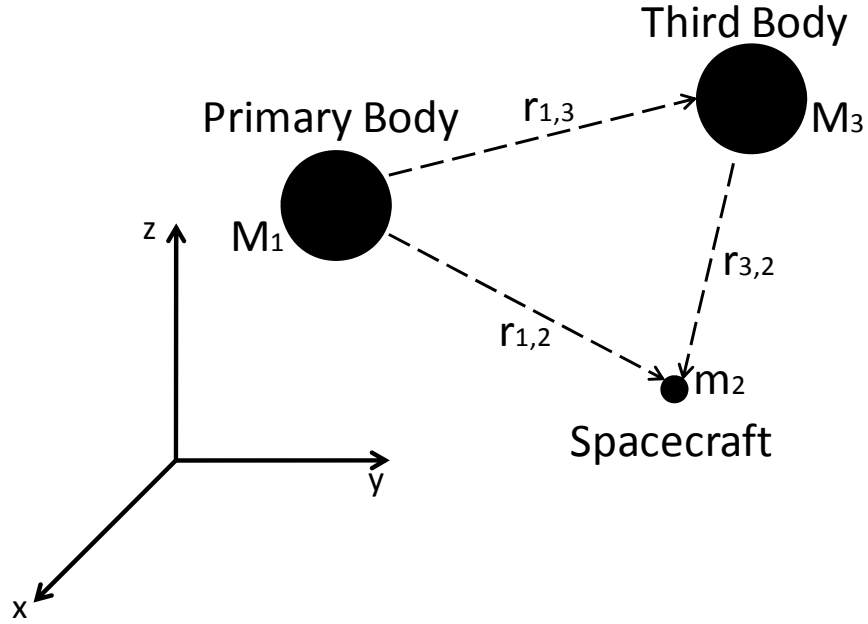


Figure 10. Three-Body Geometry (After Vallado, 1997)

The first term in Equation (1.5) is the 2-body part of the equation of motion, where the subscript “1” represents the primary gravitational body. The spacecraft in the equation is body number “2.” The summation term on the right represents the gravitational perturbation forces due to additional bodies j through n , starting with body number “3.” The perturbation term itself has two parts, the left term called the *direct effect* because it represents the force acting directly on the spacecraft by the body. The

right hand perturbation term is called the *indirect effect* because it represents the gravitational effect on the primary, or number one, body. This form of the equation of motion for the n-body problem is known as the relative form and is used because the motion of the spacecraft is calculated relative to the primary body (Vallado, 1997).

The indirect effect of the perturbation effects can be neglected if the motion of the n-bodies is adequately characterized. Because the relative positions between the gravitational bodies can be found by celestial observation, the gravitational forces acting between the bodies can be ignored. Using the available JPL Horizons data, it is assumed that the effects of the gravitational bodies on each other are already taken into account, therefore the only perturbation effects that need be considered acting on the spacecraft are the direct effects. Therefore, Equation (1.5) reduces to:

$$\ddot{\vec{r}}_{1,2} = -\frac{\mu_1 \vec{r}_{1,2}}{r_{1,2}^3} - \sum_{j=3}^n \mu_j \left(\frac{\vec{r}_{j,2}}{r_{j,2}^3} \right) \quad (1.6)$$

3. Equations of Motion for Moon to Earth Return Mission

The specific equations of motion used in this thesis are driven by the establishment of a J2000 moon-centered, translating Cartesian frame. The origin is fixed to the moon's center and the primary axes are aligned with the J2000 sun-centered inertial Cartesian frame (SXYZ). The SXYZ frame has the X-Y plane aligned with the plane of Earth's orbit and the X direction points to the First Point of Ares. The SXYZ is a right handed system, with the Z axis perpendicular to the X-Y plane.

Cartesian coordinates are selected first, for ease of using JPL Horizons ephemeris data, and secondly because it avoids singularities in spherical coordinates that may arise due to trigonometric constraints (Yan et al., 2010).

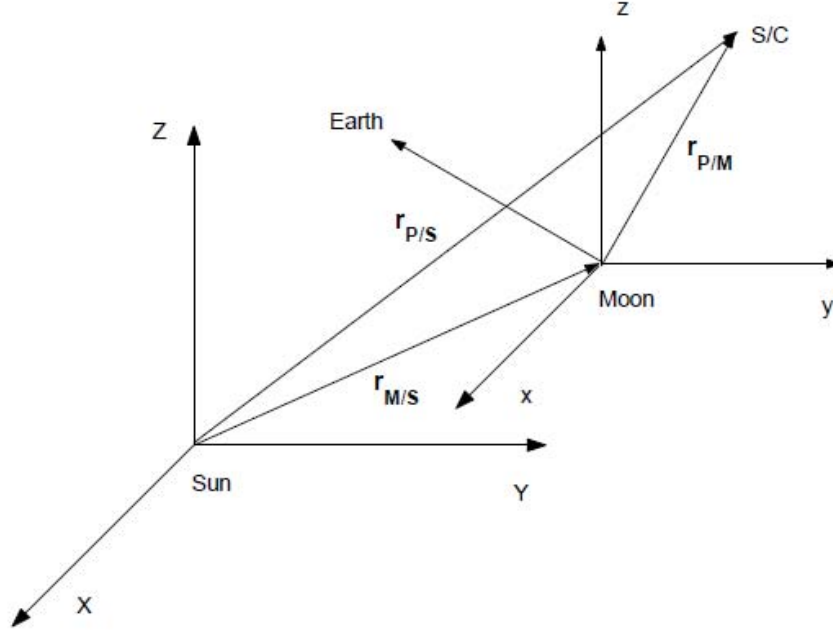


Figure 11. J2000 Sun and Moon Centered Frame (From Yan et al., 2010)

The position of the spacecraft is represented by $\vec{r}_{P/S} = \vec{r}_{M/S} + \vec{r}_{P/M}$, where $\vec{r}_{M/S}$ is the position of the Moon with respect to the center of the Sun, and $\vec{r}_{P/M}$ is the position of the spacecraft with respect to the Moon. Taking into account that the position of the spacecraft is with respect to the moon in a sun-centered inertial frame, then the following equation holds for $\vec{r}_{P/S}$:

$$\vec{r}_{P/S} = \vec{r}_{M/S} + x\hat{e}_x + y\hat{e}_y + z\hat{e}_z \quad (1.7)$$

Defining the velocity as:

$$v_x = \dot{x}, v_y = \dot{y}, v_z = \dot{z} \quad (1.8)$$

Taking the first and second derivative of Equation (1.7) with respect to the J2000 Sun-centered inertial frame yields:

$$\dot{\vec{r}}_{P/S} = \dot{\vec{r}}_{M/S} + v_x \hat{e}_x + v_y \hat{e}_y + v_z \hat{e}_z + \omega_{M/S} \times \vec{r}_{P/M} \quad (1.9)$$

$$\ddot{\vec{r}}_{P/S} = \ddot{\vec{r}}_{M/S} + \dot{v}_x \hat{e}_x + \dot{v}_y \hat{e}_y + \dot{v}_z \hat{e}_z + \omega_{M/S} \times \dot{\vec{r}}_{P/M} + \dot{\omega}_{M/S} \times \vec{r}_{P/M} \quad (1.10)$$

Noting that $\omega_{M/S} = 0$ because the orientation of the Moon-centered frame is aligned with the Sun-centered frame, Equation (1.10) simplifies to:

$$\ddot{\vec{r}}_{P/S} = \ddot{\vec{r}}_{M/S} + \dot{v}_x \hat{e}_x + \dot{v}_y \hat{e}_y + \dot{v}_z \hat{e}_z \quad (1.11)$$

The fully expressed spacecraft dynamics also have to be expressed in the Sun centered inertial frame and will include the dynamics as in Equation (1.11) as well as the controls or forces that the spacecraft will generate as part of the complete equations of motion. There are three control variables which are necessary for describing the three dimension Cartesian components of the thrust. T is the magnitude of the thrust and α and β respectively define the azimuth and elevation angles.

The dynamics can be succinctly expressed by applying Newton's second law in vector form as follows:

$$m\ddot{\vec{r}}_{P/S} = \vec{G}_M + \vec{G}_E + \vec{G}_S + \vec{T} \quad (1.12)$$

Where m is the mass of the spacecraft, \vec{T} is the thrust vector, and \vec{G}_M , \vec{G}_E , and \vec{G}_S are the gravitational forces of the Moon, Earth, and Sun respectively. The Moon's translating acceleration, also a required portion of the overall system dynamics can be defined as:

$$\vec{\ddot{r}}_{M/S} = \begin{bmatrix} \vec{\ddot{x}}_M \\ \vec{\ddot{y}}_M \\ \vec{\ddot{z}}_M \end{bmatrix} \quad (1.13)$$

The thrust vector is defined in the Moon centered frame defining α as the azimuth, and β as the elevation by the following:

$$\vec{T} = \begin{bmatrix} T_x \\ T_y \\ T_z \end{bmatrix} = \begin{bmatrix} T \cos \alpha \cos \beta \\ T \sin \alpha \cos \beta \\ T \sin \beta \end{bmatrix} \quad (1.14)$$

The time-varying components of the displacement between the spacecraft and the center of the Moon are given by (x, y, z) . Between the perturbing bodies of the sun and earth, and the primary body (moon), they are (x_s, y_s, z_s) and (x_e, y_e, z_e) respectively so that the magnitude of the displacements of the spacecraft from the gravitational bodies can be defined by:

$$\begin{aligned} r_M &= \sqrt{x^2 + y^2 + z^2} \\ r_E &= \sqrt{(x - x_e)^2 + (y - y_e)^2 + (z - z_e)^2} \\ r_S &= \sqrt{(x - x_s)^2 + (y - y_s)^2 + (z - z_s)^2} \end{aligned} \quad (1.15)$$

With (μ_M, μ_E, μ_S) representing the gravitational constants for the Moon, Earth, and Sun respectively and v_e representing the exhaust velocity of the spacecraft, the final form of the system dynamics can be written, which includes the time-varying mass of the rocket in the following equations of motion. Equation (2.16) becomes the governing set of equations of motion that are used in the problems solved in this thesis.

$$\begin{aligned}
\dot{x} &= v_x \\
\dot{y} &= v_y \\
\dot{z} &= v_z \\
\dot{v}_x &= -\ddot{x}_M - \frac{\mu_M x}{r_M^3} - \frac{\mu_E (x - x_E)}{r_E^3} - \frac{\mu_S (x - x_S)}{r_S^3} + \frac{T \cos \alpha \cos \beta}{m} \\
\dot{v}_y &= -\ddot{y}_M - \frac{\mu_M y}{r_M^3} - \frac{\mu_E (y - y_E)}{r_E^3} - \frac{\mu_S (y - y_S)}{r_S^3} + \frac{T \sin \alpha \cos \beta}{m} \\
\dot{v}_z &= -\ddot{z}_M - \frac{\mu_M z}{r_M^3} - \frac{\mu_E (z - z_E)}{r_E^3} - \frac{\mu_S (z - z_S)}{r_S^3} + \frac{T \sin \beta}{m}
\end{aligned} \tag{1.16}$$

III. OPTIMAL CONTROL THEORY

A. THE OPTIMAL CONTROL PROBLEM

Problems concerning “optimization” have a long history dating back to the ancient Greeks where through geometry they were able to determine answers to problems such as the shortest distance between two points (a line) and the maximum area enclosed by a given length of perimeter (a circle). These two problems are part of a class of problems known as optimization theory, where the former is a minimization problem and the latter a maximization problem. The calculus of variations is a theory that emerged during the eighteenth century that deals with the optimization of integrals. John Bernoulli (1667–1748) posed a problem concerning the minimization of an integral in his famous *brachistochrone problem* (Greek, brachist = shortest, chromos = time) of 1696 involving a bead sliding under gravity along a smooth wire in which he asks what shape the wire must be to reach the end point in minimum time. During the 1950s, the theory of *optimal control* emerged as a direct consequence of space exploration efforts by the Americans and the Soviets. The theory would allow a spacecraft’s trajectory to be controlled in such a manner as to reach a desired destination using minimal fuel and in minimum time (Pinch, 1993).

Optimal control theory, however, is not limited to the physical guidance and control of a spacecraft. It has applications for mission planning and in spacecraft design. Consider the case for a manned spacecraft mission in which time is a critical design factor. The mission duration drives requirements such as the fuel required for navigation and control of the spacecraft and amount of life support equipment and supplies needed to sustain the crew. Once the mission objectives are specified and the physics, or dynamics, of the problem are understood, the designer will seek for feasible solutions to problems such as the minimum time to be able to complete the mission and how much fuel to carry can be solved. Therefore, optimal control theory can be used in the design

process to determine feasible solutions to engineering problems. The strength of the results gained lie in the fact that the theory has a sound basis in mathematics, and can therefore be proved in a straightforward manner.

B. DERIVATION OF THE NECESSARY CONDITIONS USING THE CALCULUS OF VARIATIONS

The problem being solved is to determine the control $\underline{u}(t)$, such that the path, or trajectory, from an initial state $\underline{x}(t_0)$ to a final state $\underline{x}(t_f)$ minimizes the some cost functional $J[\underline{x}]$, where:

$$J[\underline{x}] = \int_{t_0}^{t_f} F(\underline{x}, \underline{u}) dt + E(\underline{x}_f) \quad (2.1)$$

The integral term represents the running cost and $E(\underline{x}_f)$ represents the end-point cost. Since real systems are being considered, it is safe to assume that any trajectory of $\underline{x}(t)$ will be continuous and twice differentiable within the domain of the state space. It is also allowable to have the controls be piecewise continuous and bounded within some finite control space. In order to show that a curve $\underline{x} = \underline{x}^*(t)$ is optimal, necessary conditions can be shown, under some assumptions of smoothness, using the calculus of variations and are as follows (Pinch, 1993):

Hamiltonian

$$H(\underline{\lambda}, \underline{x}, \underline{u}) = F(\underline{x}, \underline{u}) + \underline{\lambda}^T f(\underline{x}, \underline{u}) \quad (2.2)$$

where $\dot{\underline{x}} = f(\underline{x}, \underline{u})$

Euler-Lagrange Equation

$$\frac{\partial H}{\partial \underline{u}} = 0 \quad (2.3)$$

Adjoint Equation

$$\dot{\underline{\lambda}}(t) = -\frac{\partial H}{\partial \underline{x}} \quad (2.4)$$

Transversality Condition

$$\underline{\lambda}(t_f) = \frac{\partial \bar{E}}{\partial \underline{x}_f} \quad (2.5)$$

Where, $\bar{E}(\underline{v}, \underline{x}(t_f)) := E(\underline{x}(t_f)) + \underline{v}^T e(\underline{x}(t_f))$ is called the Endpoint Lagrangian.

The variable, λ , represents the co-state and while it has no physical meaning, it has corresponding values that mirror the state variables. The adjoint equation represents the co-state dynamics and has a direct relationship to its corresponding state variable via the Hamiltonian equation. The transversality condition looks at the endpoint cost based on the final state in order to find final conditions of the co-states.

C. PONTYAGIN'S PRINCIPLE

In 1955, it was discovered that a problem existed with the Euler-Lagrange equations in that it was impossible to solve for bounded controls. The problem was not with the engineering or the physics of the controls in question, rather with the math. Pontryagin then invented a new theory known as the Hamiltonian Minimization Condition (HMC) which then replaced the Euler-Lagrange equations. The HMC was able to handle bounded controls, which is typically the case in any control system. In most cases, steering or attitude control is unbounded since all the angles in a circle can be described in positive or negative multiples of 2π . In the case of an applied torque or thrust for control, the realities of physics dictate that there will be upper and lower limits to such a control. Therefore, Pontryagin's HMC was therefore a necessary development in the practice of optimal control theory (Ross, 2009).

An example of the constrained control problem can be described in a two-dimensional case of an orbit transfer problem where the state and controls are given by

$\underline{x} = [x, y, v_x, v_y, m]^T$ and $\underline{u} = [T, \beta]^T$. The state is described by the position and velocity in two dimensions, and mass. The control variables describe the magnitude of thrust and angle with respect to the reference frame. The Hamiltonian for this problem becomes:

$$H(\underline{\lambda}, \underline{x}, \underline{u}) = \lambda_x v_x + \lambda_y v_y + \lambda_{v_x} \left(K_x(t) + \frac{T}{m} \cos \beta \right) + \lambda_{v_y} \left(K_y(t) + \frac{T}{m} \sin \beta \right) + \lambda_m \left(-\frac{T}{v_e} \right) \quad (2.6)$$

The portion of the dynamics equations that do not depend on the controls are given by $K_i(t)$. The exhaust velocity, v_e , is constant and is a function of the physical characteristics of the rocket motor. The dynamics portions of the equation are excluded for brevity because they do not contain any control components.

From the Euler-Lagrange equation, the optimal steering law is determined by:

$$\frac{\partial H}{\partial \beta} = -\frac{\lambda_{v_x} T}{m} \sin \beta + \frac{\lambda_{v_y} T}{m} \cos \beta = 0 \quad (2.7)$$

$$\tan \beta = \frac{\lambda_{v_y}}{\lambda_{v_x}} \quad (2.8)$$

However, determining the optimal thrust law proves problematic since T vanishes:

$$\frac{\partial H}{\partial T} = \frac{\lambda_{v_x}}{m} \cos \beta + \frac{\lambda_{v_y}}{m} \sin \beta - \frac{\lambda_m}{v_e} = 0 \quad (2.9)$$

The Euler-Lagrange equations give areas where the slope of the Hamiltonian is zero, thus giving potential locations where maxima and minima may exist. However, if the slope is not zero at the endpoints, then these points would be excluded even though they might also contain maxima and minima. Example Hamiltonian curves are given in

Figure 12 where the Euler-Lagrange equations would give an incorrect value of the controls if the minimized Hamiltonian was only realized where the slope was zero.

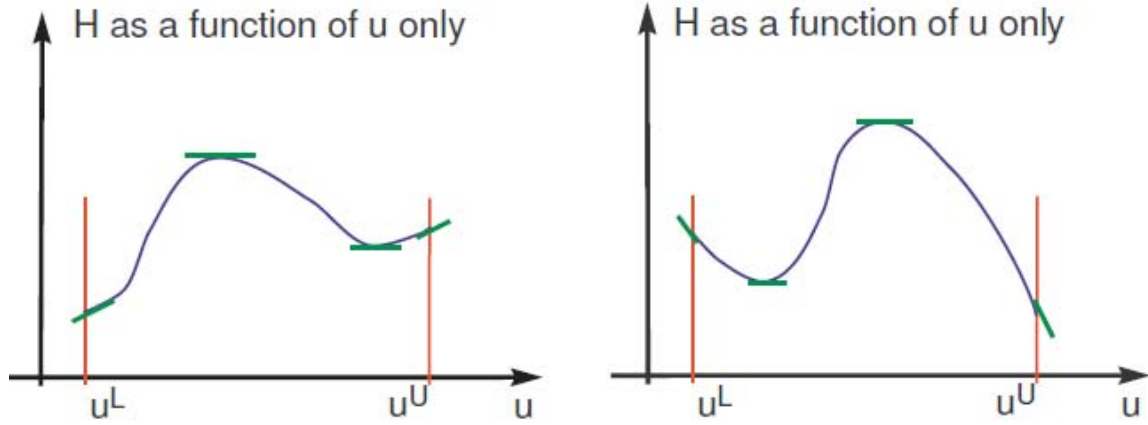


Figure 12. Hamiltonian as a function of \mathbf{u} only (From Ross, 2009)

Pontryagin's HMC, therefore replaces the Euler-Lagrange equation and minimizes $H(\underline{\lambda}, \underline{x}, \underline{u})$ subject to the upper and lower bounds of the control, $\underline{u}^L \leq \underline{u} \leq \underline{u}^U$. He also proved that the minimized Hamiltonian is constant with respect to time and that for *minimum time* problems the constant is equal to zero and for *fixed time, minimum fuel* problems is equal to -1.

It can be shown that from the HMC that a relationship exists between the direction of the thrust vector and the direction of the co-state related to velocity. Equation (3.10) shows that the angle between them is 180 degrees.

$$\frac{\bar{T}}{T} = -\frac{\bar{\lambda}_v}{\lambda_v} \quad (2.10)$$

D. THE SWITCHING FUNCTION

Noting that the Hamiltonian as a function of T is linear, and is bounded subject to $0 \leq T \leq T_{\max}$, the right hand side of (2.9), which is the coefficient of T in H , becomes the switching function, S .

$$S := \frac{\lambda_{vx}}{m} \cos \beta + \frac{\lambda_{vy}}{m} \sin \beta - \frac{\lambda_m}{v_e} \quad (2.11)$$

Figure 13 shows the Hamiltonian as a linear function of T , where S is either the positive or negative slope of the line. This result implies that when the switching function is negative, the thrust is T_{\max} and when positive, the thrust is equal to zero. These two cases refer to what is known as *bang-bang* control, where the control is either maximum or minimum. There is a special case where the switching function is equal to zero which implies that the thrust lies between the maximum and minimum bounds that is covered in the next section. It can be shown that for unconstrained steering controls, the HMC yields the same result as the Euler-Lagrange equation, so Pontryagin's Principle is the general case of the Euler-Lagrange condition (Ross, 2009).

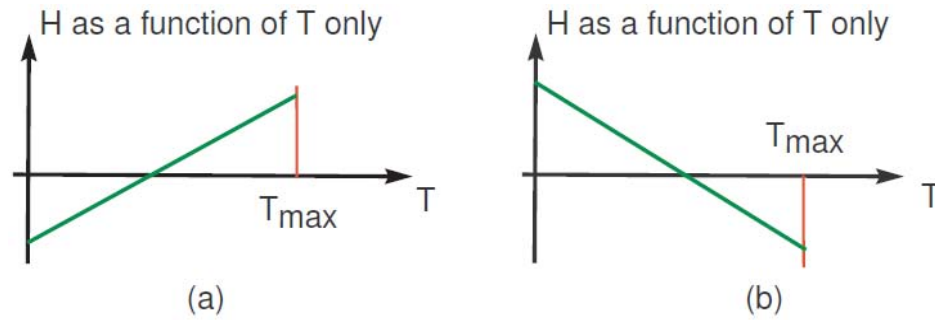


Figure 13. H as a function of T only (From Ross, 2009)

E. NECESSARY CONDITIONS FOR SINGULAR ARC OPTIMALITY

The case where the switching function equals zero occurs when an intermediate, or singular, thrust arc appears as part of the optimal trajectory where the thrust will assume a value between the upper and lower bounds. Singular optimal control theory was developed as a result of the examination of intermediate thrust arcs in central inverse-square gravity fields and what resulted was the Higher Order Maximum Principle. The Principle follows the results of Pontryagin's HMC and then takes the derivative of the switching function repeatedly to develop the necessary conditions for an optimal singular arc. This requires the derivation of an explicit function of the thrust in order to develop a singular optimal control law. Since the switching function equals zero, each subsequent derivative must clearly also equal zero. Taking the derivative of the switching function with respect to time shows that T does not appear explicitly until the fourth derivative, which implies that the problem contains a second order singular control (Park, C., Yan, H. Gong, Q., and Ross, I.M., 2010). Determining that the fourth order derivative is equal to zero is especially important when verifying numerical solutions as the results are typically close, but never exactly equal to zero.

The problem Yan et al. were solving was identical to the problem solved in this thesis, the only difference in that the rocket specifications were for the Orion spacecraft main engines. Since the equations of motion and dynamics of the problems are identical, the derived necessary conditions hold here.

$$\frac{dS}{dt} = \frac{\bar{\lambda}_r \cdot \bar{\lambda}_v}{m\sqrt{\bar{\lambda}_v \cdot \bar{\lambda}_v}} = 0 \quad (2.12)$$

$$\frac{d^2S}{dt^2} = \frac{1}{m\sqrt{\bar{\lambda}_v \cdot \bar{\lambda}_v}} \left[-\bar{\lambda}_r \cdot \bar{\lambda}_r + \left(\frac{\mu}{r^3} + \frac{\mu_i}{r_i^3} \right) (\bar{\lambda}_v \cdot \bar{\lambda}_v) - 3 \left(\frac{\mu (\bar{r} \cdot \bar{\lambda}_v)^2}{r^5} + \frac{\mu_i (\bar{r}_i \cdot \bar{\lambda}_v)^2}{r_i^5} \right) \right] \quad (2.13)$$

$$\frac{d^3S}{dt^3} = \frac{1}{m\sqrt{\bar{\lambda}_v \cdot \bar{\lambda}_v}} \frac{d}{dt} [S_2] \quad (2.14)$$

$$\frac{d^4 S}{dt^4} = \frac{1}{m\sqrt{\bar{\lambda}_v \cdot \bar{\lambda}_v}} \frac{d}{dt} \left[\frac{d}{dt} [S_2] \right] \quad (2.15)$$

The resulting third and fourth order derivative equations are rather long, and the control variable T only appears explicitly at the fourth derivative. The explicit forms for the first through fourth derivatives of S with respect to time are found in Appendix A. With these equations, it is now possible to verify the optimality of singular arcs that appear as part of an optimal earth return trajectory, however as alluded to previously, numerically validating equality to zero can be troublesome. Therefore applying another result using the calculus of variations known as the Generalized Legendre-Clebsch, or General Convexity, condition, see Equation (3.16), the numerical verification is made straightforward (Bryson, 1975). In the equation below, the subscript i represents the terms for the earth and sun. Terms without a sub-script are the terms for the moon.

$$\begin{aligned} (-1)^4 \frac{\partial}{\partial T} \frac{d^4}{dt^4} \left(\frac{\partial H}{\partial T} \right) &= \frac{\partial}{\partial T} \frac{d^4 S}{dt^4} \geq 0 \\ \Rightarrow \frac{1}{m^2} \left[\frac{9\mu(\bar{r} \cdot \bar{\lambda}_v)}{r^5} + \frac{9\mu_i(\bar{r}_i \cdot \bar{\lambda}_v)}{r_i^5} - \frac{15\mu(\bar{r} \cdot \bar{\lambda}_v)^3}{r^7(\bar{\lambda}_v \cdot \bar{\lambda}_v)} - \frac{15\mu_i(\bar{r}_i \cdot \bar{\lambda}_v)^3}{r_i^7(\bar{\lambda}_v \cdot \bar{\lambda}_v)} \right] &\geq 0 \end{aligned} \quad (2.16)$$

F. TRANSVERSALITY CONDITION

The derivation of the transversality conditions are outlined in Appendix B and the following condition holds for the minimum fuel problem.

$$\lambda_m(t_f) = -1 \quad (2.17)$$

G. SUMMARY OF NECESSARY CONDITIONS FOR OPTIMALITY

In summary, the following necessary conditions hold for optimal control:

1. Hamiltonian is constant. (-1 for minimum time, 0 for fixed-time, minimum fuel)
2. $\frac{\bar{T}}{T} = -\frac{\bar{\lambda}_v}{\lambda_v}$
3. $T = \begin{cases} 0, & \text{when } S > 0 \\ T_{\max} & \text{when } S < 0 \\ \text{Singular} & \text{when } S \equiv 0 \end{cases} \text{ where } S = -\frac{\lambda_v}{m} - \frac{\lambda_m}{v_e}$
4. Verify optimality of singular arcs.
 - a. Numerically verify that $\frac{d^4 S}{dt^4} = 0$ for singular arcs.
 - b. Check Generalized Legendre-Clebsch Condition, $\frac{\partial}{\partial T} \frac{d^4 S}{dt^4} \geq 0$
5. $\lambda_m(t_f) = -1$ (for minimum fuel cases only)

H. GENERIC PROBLEM FORMULATION

The format for the problems solved in this thesis follow Pontryagin's method for solving optimal control problems. The format is useful, as the formulation of the problems in DIDO© are made easier as the boundary conditions and constraints are clearly stated. There are primarily two types of optimal controls problems that are solved, namely a *minimum time* and *minimum fuel*. Each type of problem has a special set of boundary conditions that are expressed in the problem formulation. For example, the minimum time solution will have a free condition on the final mass and final time. In the coding of the problem, the final mass will have to be fixed at zero, or close to zero to prevent an unrealistic negative mass solution. In the minimum fuel problem formulation, the final time would be fixed and the final mass would be free.

Each of the problems solved in this thesis include a third physical dimension, z, start with the following format and the conditions derived for the two-dimensional case described earlier still hold.

Generic Problem Formulation

Where $\underline{x} = [x, y, z, v_x, v_y, v_z, m]^T$ and $\underline{u} = [T, \alpha, \beta]$,

$$\left\{ \begin{array}{ll} \text{Minimize} & J[x(\cdot), u(\cdot), t_f] = t_f \text{ or } m_f \\ \text{Subject to} & \dot{\bar{X}} = f(\bar{x}, \bar{u}, t) \\ & \underline{x}(t_0) = \underline{x}^0, \underline{x}(t_f) = \underline{x}^f \\ & \text{And any other boundary conditions and/or constraints} \end{array} \right.$$

IV. USING DIDO©

A. INTRODUCTION

The use of computer-based software packages such as DIDO© allow for solving of complex optimal control problems, however there are many challenges associated with solving the types of problems discussed in this thesis. Primarily, a solid understanding of the underlying physics of the problem being solved should be well understood, especially during the verification and validation process. This also includes an understanding of what is being optimized in the problem and checking to see if the result makes physical sense as well as meeting the necessary conditions for optimality. Finally, an understanding of the limits of numerical computation is useful in order to make the code run more efficiently. The verification and validation steps taken for the problems in this thesis are described, following a brief description of how the problems were formulated in DIDO©.

B. PROBLEM FORMULATION IN DIDO©

DIDO© is a software module that works with Matlab. It implements Legendre pseudospectral methods which are used to solve complex, non-linear optimal control problems (Ross I.M. , 2007). Its primary advantage is that it can solve the problems with as few or many discrete points, or LGL nodes, as defined by the user, which makes the computation time relatively short. However, this requires an iterative process of increasing the number of nodes, until the desired fidelity is achieved. It has a straightforward interface that allows the user to set up an optimal control problem using the previously described Generic Problem Formulation. The problem formulation is broken up into two parts, namely the cost function, which specifies what design parameter is being minimized, and the constraints. The constraints can be further divided into two parts. The spacecraft in each of the problems is constrained to move subject to the equations of motion, or the dynamics. In each of the problems, there is also a set of boundary conditions describing the initial and final states of the spacecraft which were

given parameters. The problem formulation in DIDO© follows this separation of the problem formulation by requiring separate M-files that are called by a main problem file. An additional file may be used to specify a path constraint, but it is not always required, and is typically problem dependent.

The files used in addition to the main program file, then are:

- *Cost Function* – outputs are the endpoint cost and running cost. In the problems being examined, only endpoint costs are required and are problem specific. In the following cases it is either the final time, t_f (minimum time case), or the final mass, m_f (minimum fuel case).
- *Dynamics Function* – provides the differential equation $\dot{\bar{x}}(t) = f(\bar{x}(t), \bar{u}(t), t)$ as described by the problem dynamics. The same set of dynamics equations is used for all cases studied.
- *Events Function* – used to describe the boundary conditions to include the initial and final states of the problem. For example, in the minimum-fuel, constrained-time problem, the initial state is $\bar{x}_0 = [x^0, y^0, z^0, v_x^0, v_y^0, v_z^0, m^0,]$ and the final state is $\bar{x}_f = [x^f, y^f, z^f, v_x^f, v_y^f, v_z^f]$, noting that there is no final mass specified since that is the parameter being solved for.

The main program file calls these files and then requires the establishment of upper and lower bounds on the states and the controls. This is important step for primarily computational reasons. It provides a range of values that the DIDO© algorithm can use in the output of state and control trajectories. Given that the physical displacement and velocities of the spacecraft should be limited to a region near the earth and moon, the upper bounds of the state variables should be provided accordingly. However, if the bounds are too small, the resulting trajectories might result in either an infeasible or non-optimal solution. Excessively large bounds will start to affect computation time. DIDO© also allows for an initial guess of the trajectories that gives the program a starting point, however it is possible to get acceptable results without an

initial guess. The actual algorithm that solves the problem is called in Matlab by a single command line and its outputs are the final cost, as well as *primal* and *dual* structures. The primal structure includes the state and control vectors and associated discrete times with their lengths being equal to the number of LGL nodes used. The dual structure includes the co-state and Hamiltonian vectors, also equal to the number of nodes. These outputs can then be used for further analysis for verification of optimality and feasibility.

C. BEST PRACTICES

1. Scaling

Most computational numerical methods make use of unit scaling, without loss of generality, to increase computational efficiency by increasing rate of convergence while increasing accuracy (Ross I.M., 2009). There are no set ground rules on how to scale units, however a uniform range of values can make the program run smoother (Betts, 2001). In astrodynamics problems in particular, scaling becomes an important factor in problem formulation because of the scale at which spacecraft are operating. Typically, the range of values for the distances travelled can be on the order of 10^7 meters, but the timeframe of interest may only be on the order of a few hours. Also to be considered are the values of forces in kilonewtons, for example, which depend on the standard units of mass, distance, and time.

For the problems discussed in this thesis, the following “canonical” units were used to scale the variables for computation.

- 1 Displacement Unit (DU) = 1,737 km (mean radius of the Moon)
- 1 Mass Unit (MU) = 20,339.9 kg (wet mass of spacecraft)

$$\bullet \quad 1 \text{ Time Unit (TU)} = \sqrt{\frac{DU^3}{\mu_M}} = \sqrt{\frac{(1,737 \text{ km})^3}{4,902.8 \text{ km}^3/\text{sec}^2}} \cong 1,033.9 \text{ sec}$$

Where μ_M is the moon's gravitational constant.

$$\bullet \quad 1 \text{ Velocity Unit} = \frac{1DU}{1TU} = \frac{1,737 \text{ km}}{1,033.9 \text{ sec}} = 1.68 \text{ km / sec}$$

- $1 \text{ Force Unit} = \frac{1MU \cdot 1DU}{1TU^2} = \frac{20,339.9 \text{ kg} \cdot 1,737 \text{ km}}{(1,003.9 \text{ sec})^2} \cong 33.1 \text{ kN}$

The units scaled in this fashion are sufficiently close in order of magnitude to maintain computational efficiency and are able to be converted to and from the actual (un-scaled) values for analysis.

2. LGL Nodes

Typically, these types of complex optimal control problems cannot be solved in a single step with a large number of LGL nodes primarily due to computation time. The software used allows the user to choose the number of discrete points as the output and allows for taking the output of a lower node solution and using it as a guess for a higher node solution. If the problems are well scaled and the problem is properly formatted, this allows for a rapidly converging solution without excess computational time. In the problems studied in this thesis, the typical starting point was at 30 or 40 LGL points and then each incremental step increase in nodes was of the same order. The exception was the study of the high thrust singular arc in which a much lower number of nodes was used to start because of the short time duration of the event.

3. Providing an Initial Guess

It is possible, though not required, to provide DIDO© with a “guess” trajectory for the controls and states. Providing a reasonable guess will, in most circumstances, produce a faster result. Each of the cases studied in this thesis started with a low number of LGL nodes and with no initial guess, however as the number of nodes and subsequent fidelity of the solutions were increased, the preceding solutions were used as an initial guess for the next iteration. This concept of using an initial guess was used in two different ways depending on the situation.

Starting at the low fidelity solution, typically 30 to 40 LGL nodes, it is possible to take the resulting primal structure (controls, discrete time values, and states) and use them as the initial guess for a subsequent run of DIDO© at a higher number of nodes. Experience shows that increasing in increments of no more than 30 to 40 works best.

This method is called bootstrapping, but cannot be used without analysis of the preceding result so as not to propagate errors caused by bad problem formulation, scaling, etc. Therefore, each step of the problem solution process should be checked for optimality conditions, feasibility, and other verification and validation techniques discussed below.

The difficulty with the angles is that as previously mentioned they are unbounded controls, however, in coding the problem it is typically unwise to allow infinite bounds for computational reasons. The problem as coded must establish small enough bounds so that it can be handled by the computer, but must also be large enough to facilitate the possible range of solutions. With $\alpha, \beta \in [-2\pi, 2\pi]$, this allowed for a wide range of angles from which the solution could be found.

The resulting control angles are allowed within the program to reach the limits of the bounded region, however when this happens it is difficult to determine whether the control has hit a “physical” limit imposed by the code or the angle is equal to that limit, which in this case is zero degrees. Because of the non-unique nature of trigonometric functions, a one-to-one mapping of solutions is not possible and computer algorithms typically cannot discern the difference between them (i.e. $\sin(\pi/2) = \sin(5\pi/2) = 1$). Therefore, for any computer algorithm additional conditions may have to be imposed.

In certain cases, angle reduction formulas could be used to convert the output angles into a set of angles that fall between $\alpha, \beta \in [-\pi, \pi]$ which would then provide the full range necessary for the problem solution. From Equation (1.16), the Cartesian components of the thrust vector can be re-written as:

$$\begin{aligned} T_x &= T \cos(\alpha) \cos(\beta) \\ T_y &= T \sin(\alpha) \cos(\beta) \\ T_z &= T \sin(\beta) \end{aligned} \tag{4.1}$$

From these equations, explicit formulas for the angles can be derived.

$$\alpha = \tan^{-1}\left(\frac{T_y}{T_x}\right)$$

$$\beta = \sin^{-1}\left(\frac{T_z}{|T|}\right), \quad |T| = \sqrt{T_x^2 + T_y^2 + T_z^2} \quad (4.2)$$

Noting that a singular condition occurs when $|F|=0$, this can be neglected by the fact that any combination of angles has no effect on a spacecraft's trajectory when the thrust is zero, therefore when this is the case the angles can be forced to zero with no loss of generality to the problem. Figures 14 and 15 show how a set of resulting angles from DIDO© can be recalculated using Equation (4.2) which can then be used as the initial guess for the angles for the next iteration.

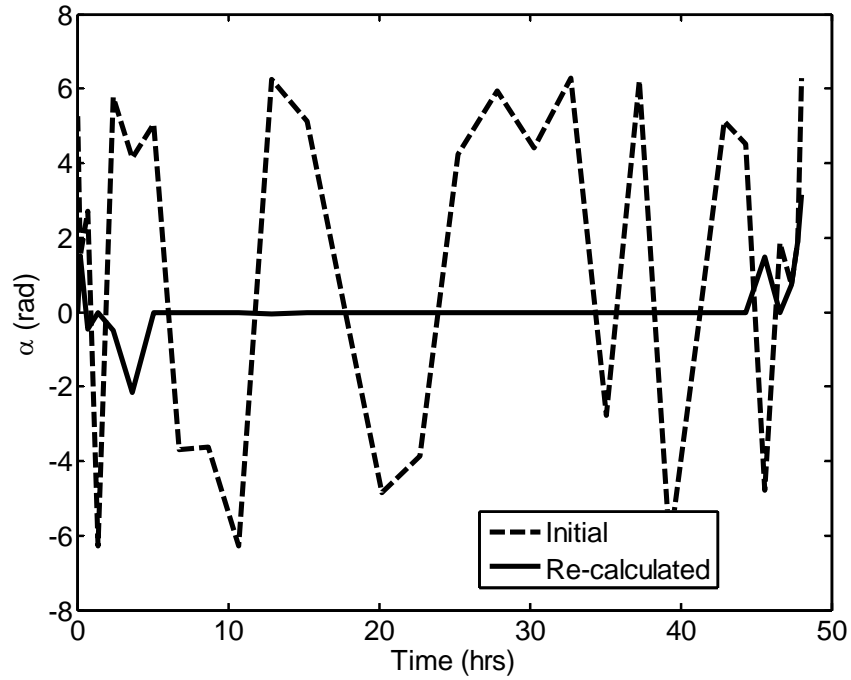


Figure 14. Recalculation of Azimuth Control Angle

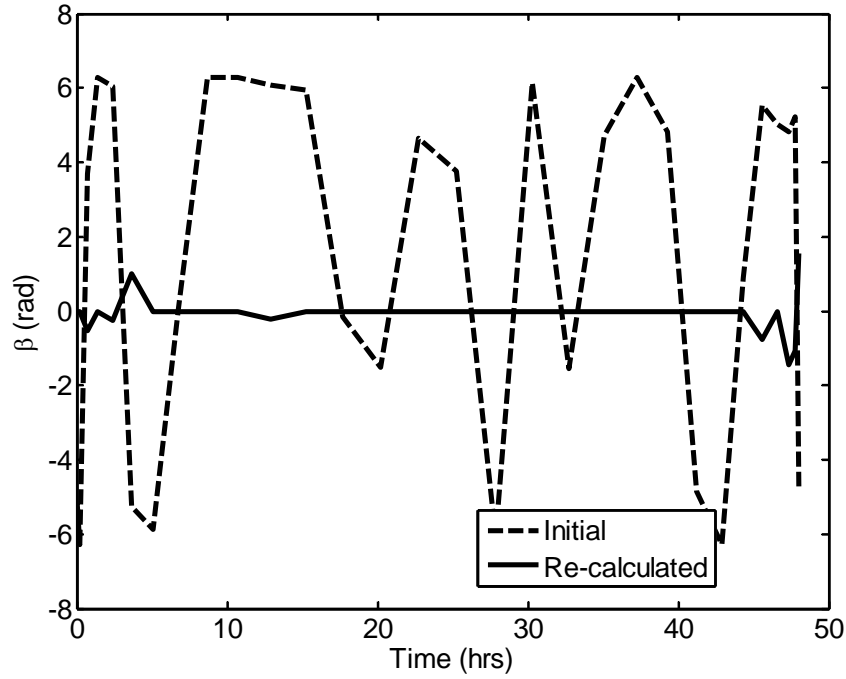


Figure 15. Recalculation of Elevation Control Angle

As the problem increases in fidelity and the control angles start to fall within a tighter range of values, it is then possible to tighten up the coded bounds to help speed up computation.

D. VERIFICATION AND VALIDATION

1. Examining Initial Output

One of the first steps in the analysis conducted was to generate plots of the state and control trajectories as well as the evolution of the Hamiltonian and the co-states. One of the first checks is to determine if any unexpected or undesired limits of the imposed bounds were met. In the case of thrust, the limits are expected because of the actual physical limitations of the thruster (no negative thrust and a maximum attainable thrust). Hitting the bounds on the control angles was covered above. For a minimum time problem, the final time should not hit the upper bound because it usually results in an

infeasible solution indicating that the time horizon should be longer. In the minimum fuel problem, the upper time bound is typically fixed, and therefore coded appropriately.

2. Checking Necessary Conditions for Optimality

From the *dual* variables output of DIDO© the Hamiltonian and co-state vectors can be plotted with respect to time and using the necessary conditions from Chapter III can be used to verify the optimality of the solution.

3. Checking Feasibility

The DIDO© endpoint conditions can be validated against the given endpoint conditions, however the purpose of performing the feasibility analysis is to validate the DIDO© solution and determine if the solution has enough fidelity to be “flyable.” A method of verifying the feasibility of the solution is to take the same initial conditions for the problem and propagate the same dynamics, using Matlab’s *ode45* solver, over the same timeframe to evaluate how closely the state trajectories follow the DIDO© solution. This requires an interpolation of the generated controls for areas between the nodes since there many more points used in the *ode45* solver compared to the sparse number of points generated by DIDO©. Plotting the DIDO© and propagated state trajectories simultaneously can provide a good visual indicator of whether the solution is making physical sense, assuming the dynamics are correct. However, for problems that cover a large time horizon, the results will tend to diverge as time goes on and this is primarily a result of interpolation and propagation errors inherent to numerical solutions.

A technique that has been proven to be successful in reducing the propagation errors of the interpolated controls from the optimal solution generated by DIDO© is called the Bellman Pseudospectral (PS) Method (Ross, I.M., Gong, Q., and Sekhavat, P., 2008). Its application is based on the Bellman Principle of Optimality that states that for an optimal path between two points, any point taken along the path will follow the optimal path to the final point.

The Bellman Principle of Optimality states that along a given optimal trajectory, a segment starting from some intermediate point on that trajectory and ending at the

original termination point will also be optimal. If some trajectory \overline{AB} meets the necessary conditions for optimality, then a segment starting from point C *on the path* will follow the same optimal path to the final point. In Figure 16 the total cost of the optimal trajectory \overline{AB} is J_0 . If the point C lies on the trajectory \overline{AB} , then the trajectory from C to B will also be an optimal path on \overline{AB} , and $J_0 = J_1 + J_2$ (Kirk, 1970).

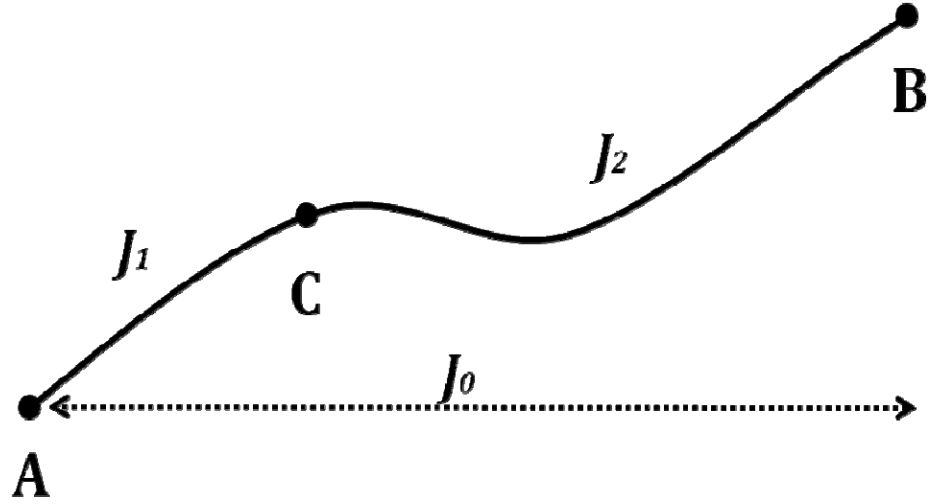


Figure 16. Bellman Principle

Yan et al. use the Bellman PS Method as a means for mesh refinement and taking advantage of DIDO© node distribution which puts a higher concentration of nodes near the beginning and end of the time horizon of the optimal trajectories. Hence, the resolution of data near the beginning and end of the trajectory is higher than in areas in the middle. Increasing the number of nodes would only offer a limited increase in resolution near the middle of the trajectory which would come at a high cost in computational efficiency. They found that by applying the technique in this manner, the interpolation and propagation errors were significantly mitigated by a few orders of magnitude (Yan et al., 2010). The application of the corollary statement was used in the

detailed analysis of the singular arc which used two points on the trajectory prior to and after the second TEI maneuver of the main engine solution as a segment which lay on an existing optimal path.

4. Comparison to Previous Studies

Finally, the results of the case studies in this thesis can be compared to the results by Yan et al. study of optimal moon to earth trajectories using the Orion spacecraft main engines as well as the study conducted by Park et al. on numerical verification of singular arcs for the same problem using a low thrust engine. The rocket engine parameters, resulting fuel consumption, and control maneuvers can be compared for analysis.

V. AUXILIARY ENGINE FOR MOON TO EARTH RETURN MISSION

For the three cases for the moon to earth return mission, the scenario depicted is a loss of the main engine with the same mission time requirement and fuel constraint. The initial position and velocity, or state, of the spacecraft is at a designated point in a low-lunar orbit from which the mission commences. The final state achieves the conditions that will take the spacecraft to the earth interface point without any further burn maneuvers. The initial epoch is given as April 4, 2024, 15:30:00 TDT. Each of the three cases studied, the final position and velocity remain the same and the results of changing the boundary conditions on time and fuel consumed are examined for the purpose of determining the overall feasibility of using the auxiliary engines as an alternative to the main engines for the return mission.

The spacecraft characteristics and fixed initial and terminal conditions are as follows (Scarritt, S., Marchand, B., and Weeks, M., 2009):

- Initial Mass: 20,339.9 kg (wet mass)
- Total Fuel Mass: 8,063.65 kg
- Auxiliary Engine Thrust: 4,448.0 N
- Auxiliary Engine Isp: 309 sec
- Initial State in the J2000 Moon centered inertial frame:

$$\begin{bmatrix} x_0 \\ y_0 \\ z_0 \\ v_{x0} \\ v_{y0} \\ v_{z0} \end{bmatrix} = \begin{bmatrix} -1,236.7970783385588 \text{ km} \\ 1,268.1142350088496 \text{ km} \\ 468.38317094160635 \text{ km} \\ 0.0329108058365355 \text{ km / sec} \\ 0.589269803607714 \text{ km / sec} \\ -1.528058717568413 \text{ km / sec} \end{bmatrix}$$

- Final State (to reach specified earth interface point)

$$\begin{bmatrix} x_f \\ y_f \\ z_f \\ v_{xf} \\ v_{yf} \\ v_{zf} \end{bmatrix} = \begin{bmatrix} 2,106.40349727063 \text{ km} \\ 3,596.40440859595 \text{ km} \\ 608.167937792834 \text{ km} \\ -0.151018343429892 \text{ km / sec} \\ -0.321178999121464 \text{ km / sec} \\ -1.79844521633271 \text{ km / sec} \end{bmatrix}$$

A. THE MINIMUM TIME, FUEL FREE PROBLEM

1. Problem Formulation

The first case of this problem was formulated as a minimum time solution with the final mass allowed to be free, but limited to a lower bound of 10% of the total spacecraft wet mass. While this problem did not satisfy the fuel requirements, it was an important first step in determining an overall feasible engineering solution. By making both the time and fuel constraints ‘free,’ it was possible to first determine the feasibility of the mission time requirement imposed on this segment of the return mission. With time as the cost function to be minimized, the spacecraft was allowed to burn as much fuel as needed, even beyond the maximum fuel capacity of 8,063.65 kg. In the Matlab code, however, an artificial lower limit of 10% of the spacecraft dry mass was imposed to prevent the mass from going negative. Provided an optimal solution existed, the goal was to determine if the minimal final time was less than the 48-hour mission constraint. This in turn implied that the use of the specified auxiliary engine would be feasible, at least in terms of the mission time constraint.

Minimum Time Formulation

Where $\underline{x} = [x, y, z, v_x, v_y, v_z, m]^T$ and $\underline{u} = [T, \alpha, \beta]$,

$$\left\{ \begin{array}{ll} \text{Minimize} & J[x(\bullet), u(\bullet), t_f] = t_f \\ \text{Subject to} & \dot{x} = v_x \\ & \dot{y} = v_y \\ & \dot{z} = v_z \\ & \dot{v}_x = -\ddot{x}_M - \frac{\mu_M x}{r_M^3} - \frac{\mu_E (x - x_E)}{r_E^3} - \frac{\mu_S (x - x_S)}{r_S^3} + \frac{T \cos \alpha \cos \beta}{m} \\ & \dot{v}_y = -\ddot{y}_M - \frac{\mu_M y}{r_M^3} - \frac{\mu_E (y - y_E)}{r_E^3} - \frac{\mu_S (y - y_S)}{r_S^3} + \frac{T \sin \alpha \cos \beta}{m} \\ & \dot{v}_z = -\ddot{z}_M - \frac{\mu_M z}{r_M^3} - \frac{\mu_E (z - z_E)}{r_E^3} - \frac{\mu_S (z - z_S)}{r_S^3} + \frac{T \sin \beta}{m} \\ & \dot{m} = -\frac{T}{v_e} \\ & \underline{x}(t_0) = \underline{x}^0, \underline{x}(t_f) = \underline{x}^f \\ & t_f \text{ and } m(t_f) \text{ are free} \\ & 0 \leq T \leq T_{\max} \end{array} \right.$$

2. Results and Analysis

This case was solved, starting at 30 LGL nodes and bootstrapping the solution up to 80 LGL nodes in order to achieve a smooth and convergent solution. As expected, in order to achieve the desired end point condition in minimum time, the spacecraft will burn fuel at a maximum rate, using maximum thrust, throughout the maneuver as depicted in Figure 17. Figures 18 and 19 show that the azimuth and elevation control angles are continuous and while they are not physical constraints on the problem, the angles do not hit the bounds specified in the Matlab code. While the fuel mass consumed exceeds the actual fuel capacity of the spacecraft, the total time of the maneuver is much less than the 48 hours required by the mission. This implies that the auxiliary engines,

subject to the dynamics of the problem, can be used and will satisfy the time requirements of the mission. Further analysis follows to verify that the auxiliary engines can be used to meet the fuel requirements as well.

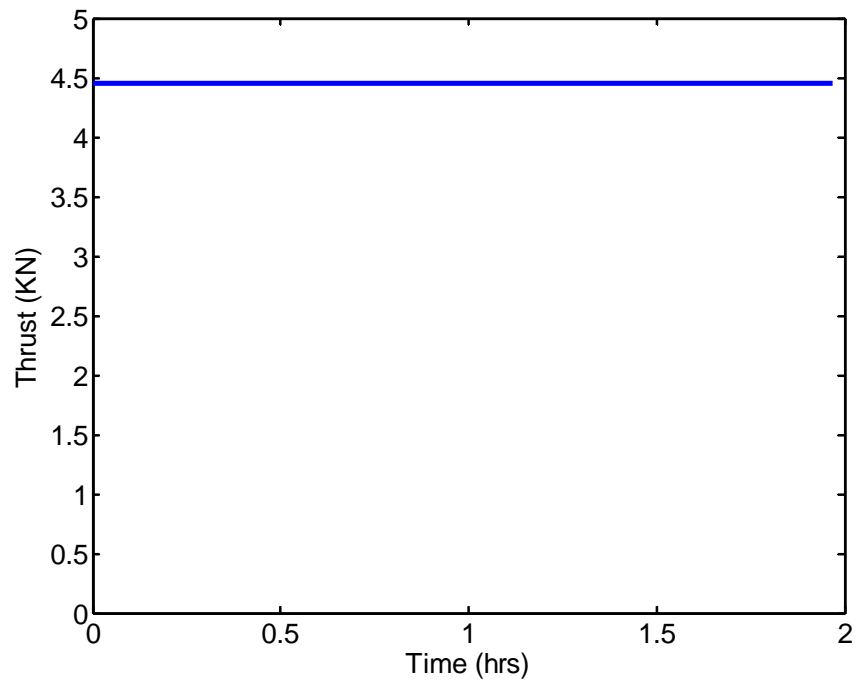


Figure 17. Thrust Profile

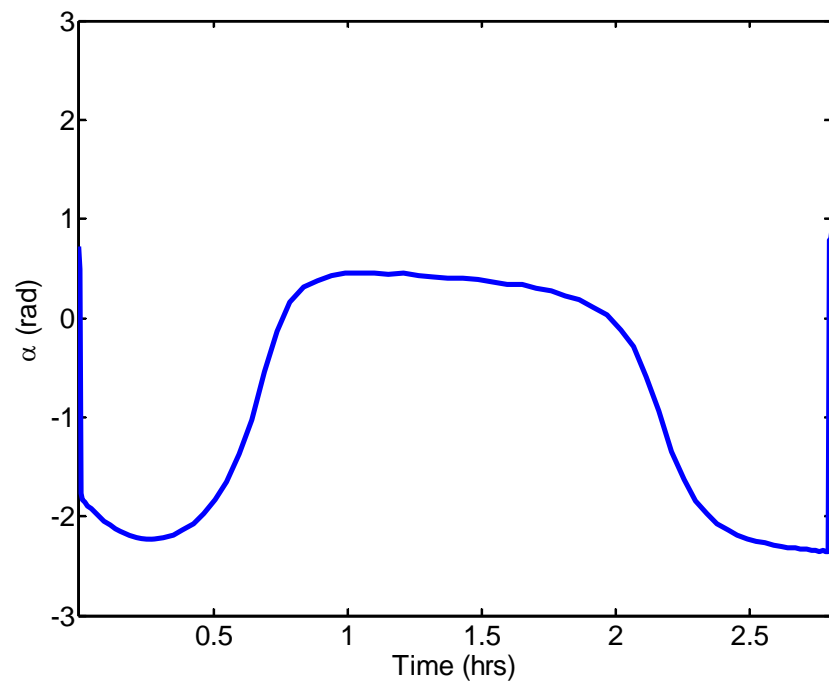


Figure 18. Azimuth Control Profile

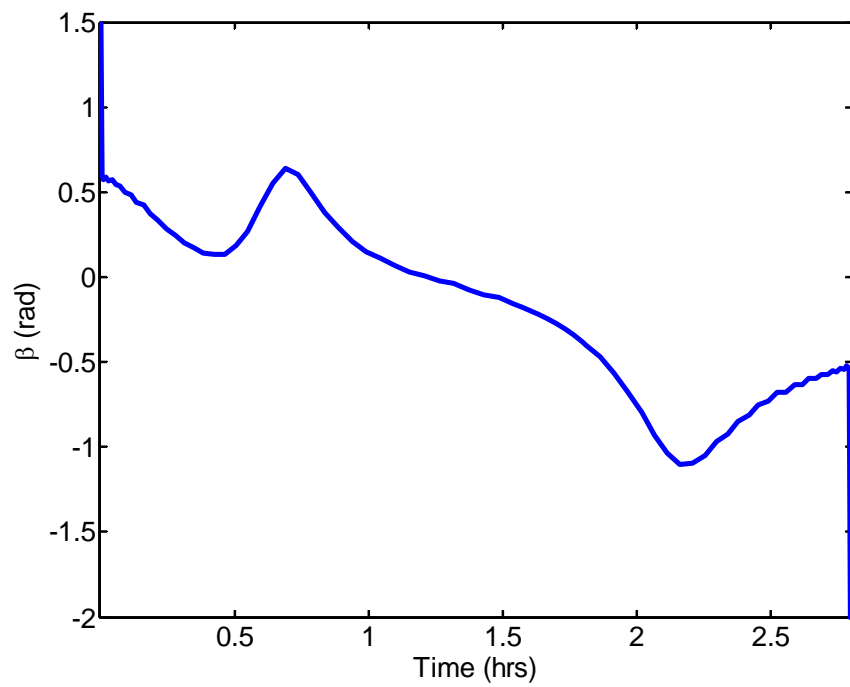


Figure 19. Elevation Control Profile

a. Feasibility of the Solution

As part of the feasibility analysis, the solution is propagated using the *ode45* function in Matlab, using the initial boundary condition and interpolating the controls over the course of the trajectory and comparing the continuous solution against the DIDO© solution of discrete points. By examining the profiles of the state vectors for position, velocity, and mass, it was found that the DIDO© solution follows the propagated solution and is deemed a feasible solution. Figures 20, 21, and 22 show the displacement, velocity, and mass trajectories. Table 3 shows the differences between the DIDO© and the propagated solutions. While the DIDO© solution achieves the specified boundary conditions, the propagated solution shows an error greater than the required limits of 1 km for displacement and 1 m/s for velocity.

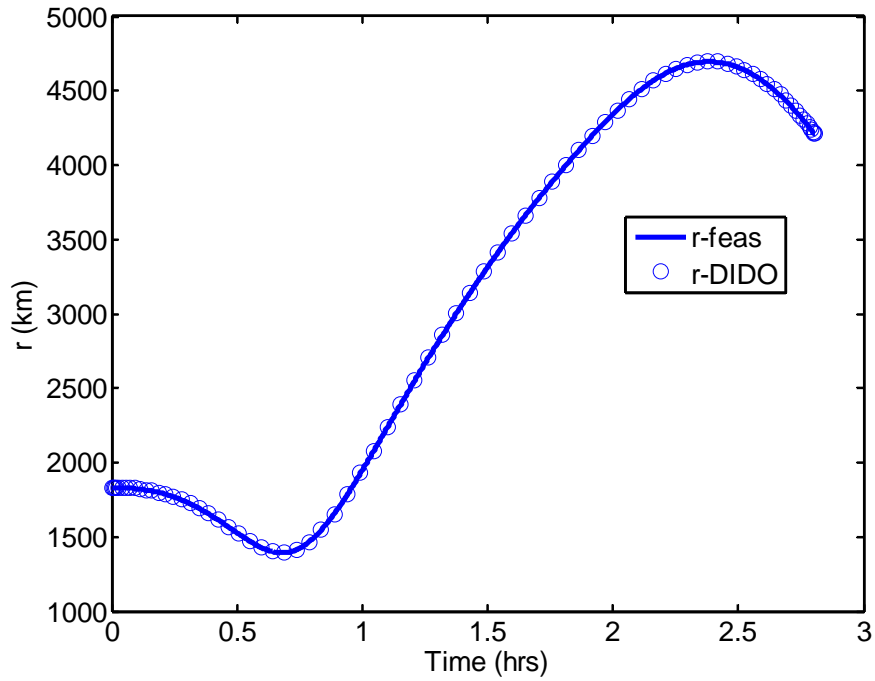


Figure 20. Displacement Vector

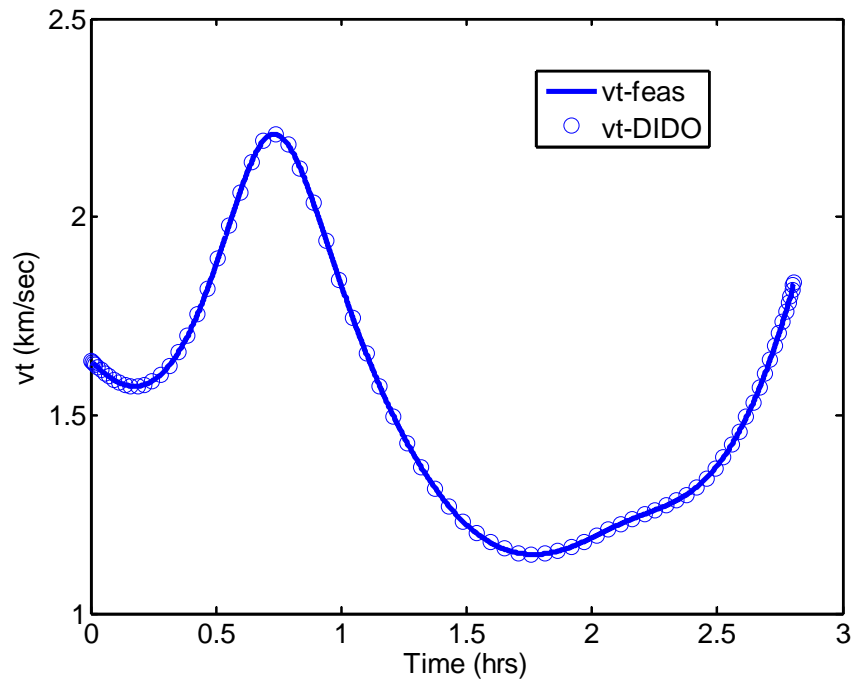


Figure 21. Tangential Velocity Vector

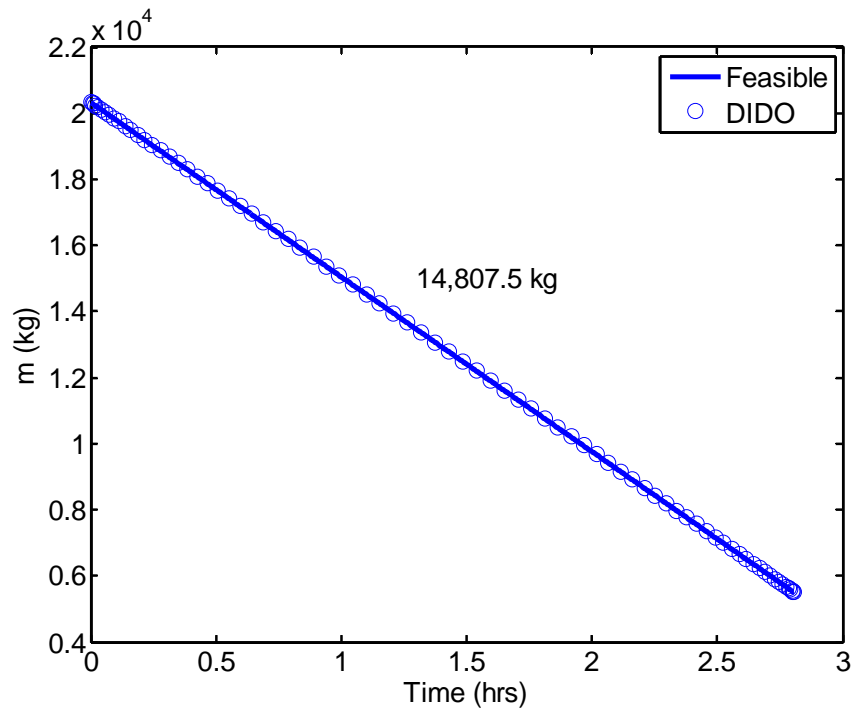


Figure 22. Fuel Consumption

	Final Position Error (km)	Final Velocity Error (m/s)
DIDO©	4.5e-13	2.2e-13
Propagated Solution	17.0	4.2

Table 3. DIDO vs. Propagated Solution

The discrepancies in the final position and velocities are due to the numerical sensitivities of this type of problem. Very slight interpolation errors at the start of the orbit transfer can cause very large errors at the terminal position (Yan et al., 2010). In this particular problem, the total time horizon is shorter than the 48-hour requirement and thus results in a relatively small error. Within two iterations of the Bellman technique, the required end-point errors are achieved. For brevity, the Bellman technique is demonstrated for this problem only, but can be used to resolve the difference between the DIDO© solution and the propagated solution in the minimum fuel case.

The Bellman pseudo-spectral (PS) technique is summarized as follows (Ross et al., 2008):

1. Solve the optimal control problem using a reasonably low number of LGL nodes to generate a discrete time solution.
2. Partition the time interval $[t_0, t_f]$ into Bellman segments $t^0 < t^1 < \dots < t^{N_B} = t^n$. The segments do not need to be uniformly spaced, however extend from a specified time until the terminal time, t_f .
3. Propagate the system dynamics from t^0 to t^1 using \bar{x}_0 as the initial condition and any method of continuous-time reconstruction of the controls, $\bar{u}_1(t), t \in [t^0, t^1]$.
4. Set $\bar{x}_0 = x^1(t^1)$ and $t^0 = t^1$ and go back to Step 1.
5. This algorithm ends when the final required conditions are met.

Using the Bellman technique in two iterations, the final required accuracy was attained. The first Bellman segment $[t_1, t_f]$ was set to start at 0.8363 hours. For simplicity, a time associated with one of the discrete time points was chosen. For the second Bellman segment $[t_2, t_f]$, a start time of 0.9640 hours was chosen. Table 4 shows the segment partition and the resulting final position and velocity errors. After two iterations, the required errors for both position and velocity are attained.

	Position Error (km)	Velocity Error (m/s)
Without Bellman technique	17.0	4.2
First Bellman segment	1.2	0.31
Second Bellman segment	0.29	0.16

Table 4. Effects of the Bellman PS Technique

Another verification of the feasibility of the solution is to examine the osculating orbital elements throughout the maneuver. Figure 23 shows the evolution of the changing semi-major axis throughout the maneuver. Towards the end of the maneuver, the semi-major axis goes to infinity which is consistent with a parabolic trajectory, but then completes the maneuver at a finite semi-major axis value. Figure 24 shows the eccentricity constantly changing throughout the orbit and eventually passes through $e = 1$, a parabola, and ends on a value greater than one which defines a hyperbolic trajectory. Both parabolic and hyperbolic trajectories imply that a spacecraft has sufficient energy to overcome the gravity well of the body which it has been orbiting (Curtis, 2005). This result shows that the spacecraft in this case has escaped the moon's gravity. Finally, Figure 25 shows a continual change in the inclination of the trajectory with respect to the moon's equator. The final states of the semi-major axis, eccentricity, and inclination are consistent with the end point conditions found for the minimum fuel solution for the main engines (Yan et al., 2010).

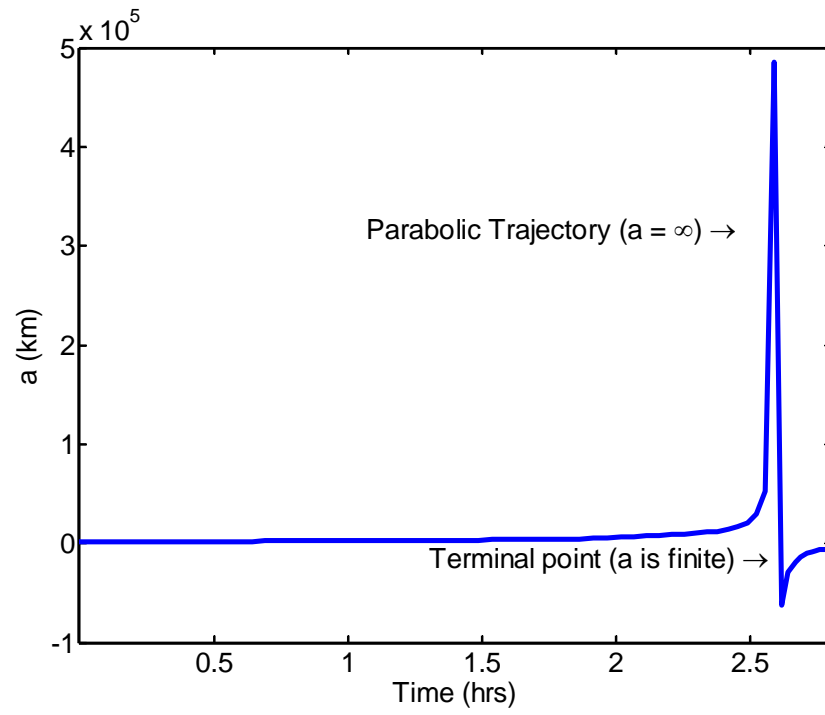


Figure 23. Semi-major Axis

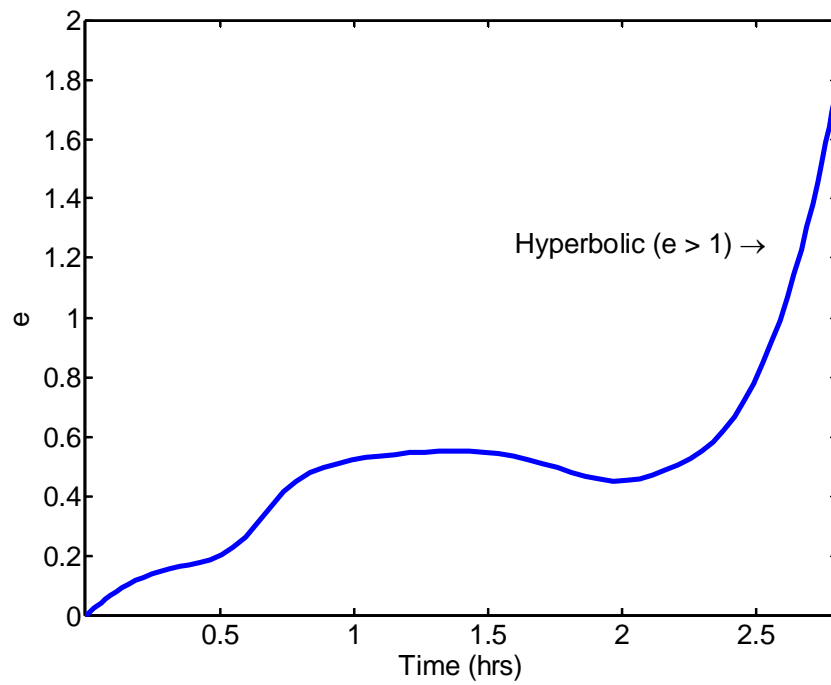


Figure 24. Eccentricity

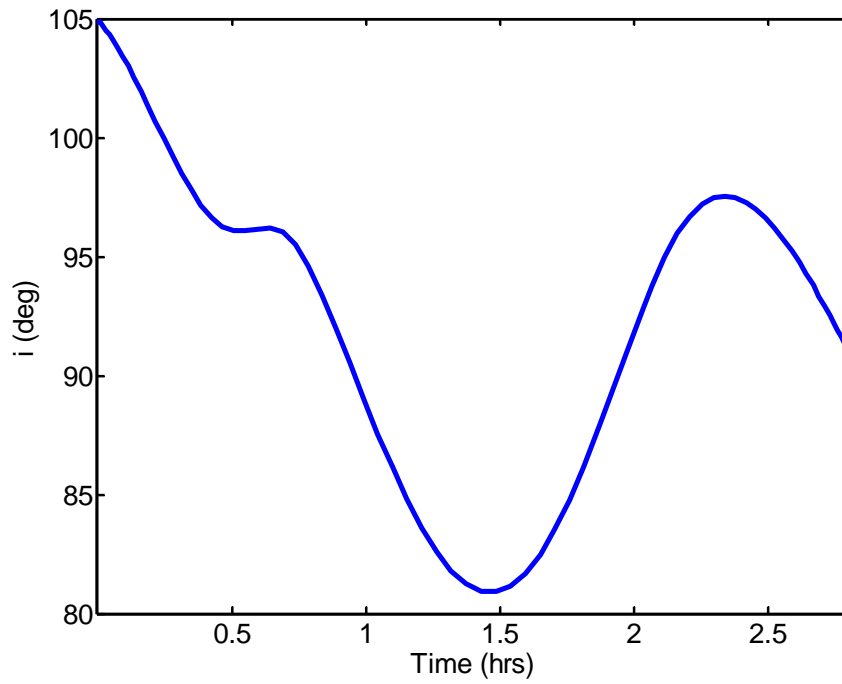


Figure 25. Inclination

b. Verification of the Optimality of the Solution

The necessary conditions for optimality are met and are examined as prescribed in Chapter III. In Figure 26, the Hamiltonian is constant throughout the maneuver and its value is consistent for a minimum time solution. From the transversality condition, the co-state related to mass has a terminal value equal to zero as shown in Figure 27.

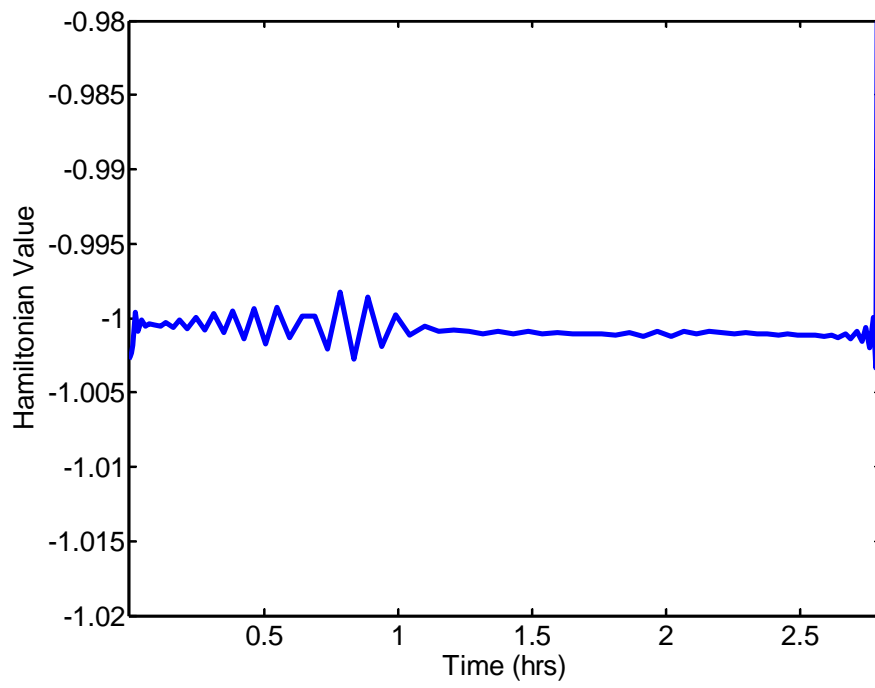


Figure 26. Hamiltonian Evolution

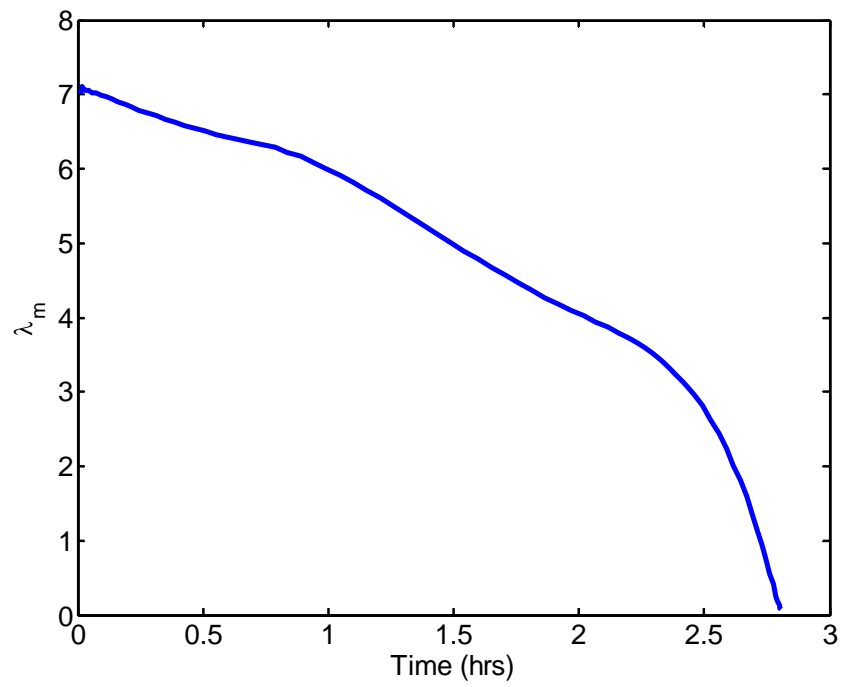


Figure 27. Co-state (λ_m) Evolution

The condition derived from the HMC that the angle of thrust is opposite the velocity co-state is depicted in Figure 28. During the maneuver, the angle maintains a value of 180 degrees as the thrust is “on” throughout. And finally, the Switching Function as defined by the HMC should be negative if the constrained control, thrust, is at maximum which is true in this case. Figure 29 shows that the switching function is indeed negative throughout the maneuver which is consistent with the thrust being at its maximum value throughout the maneuver.

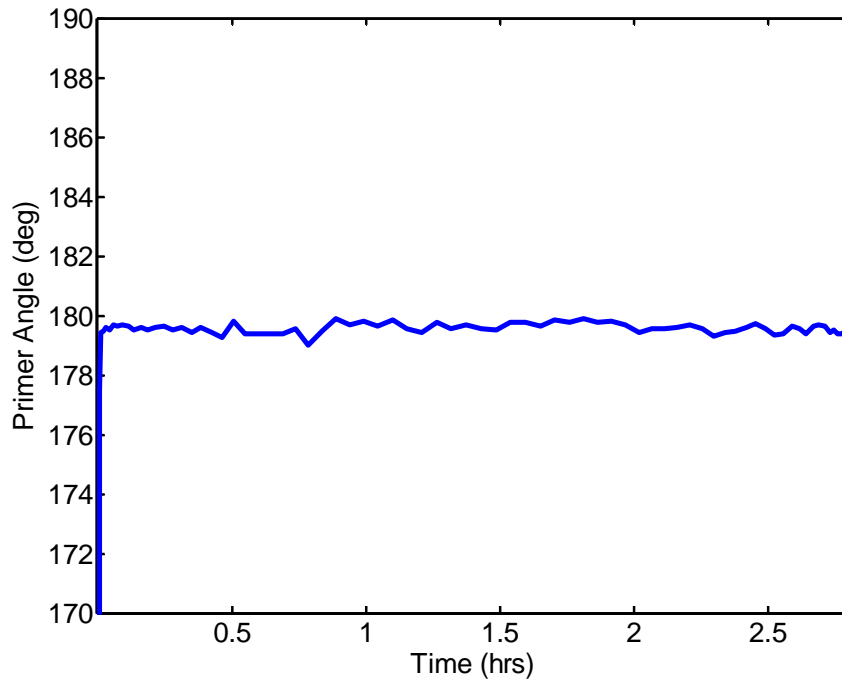


Figure 28. Primer Angle

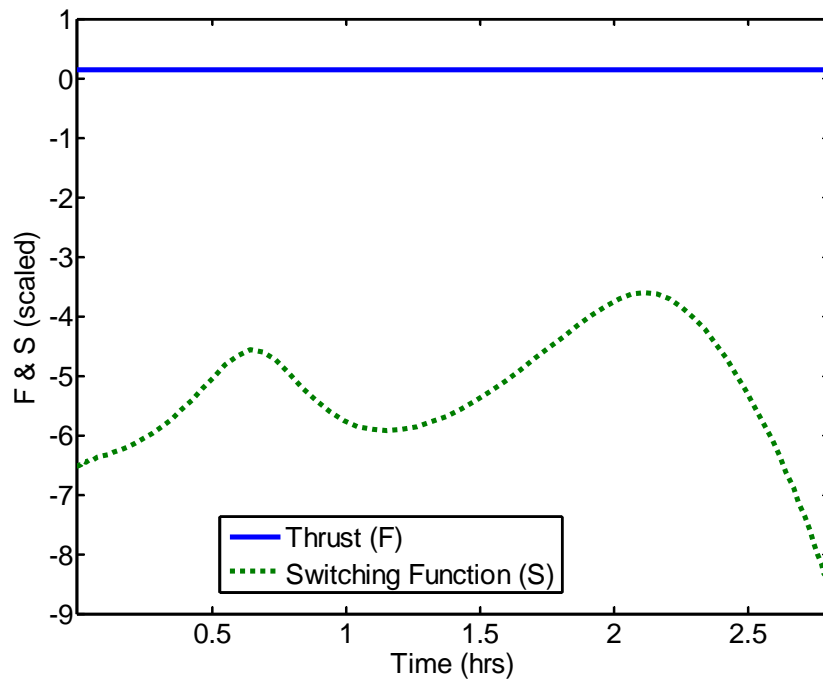


Figure 29. Switching Function

3. Conclusion for Minimum Time Case

The results show that the solution determined in the minimum time problem is optimal with respect to time. The maneuver achieves the final boundary conditions well within the 48-hour time constraint for the TEI maneuvers for the moon to earth return mission, which informs that the auxiliary engines are capable for meeting the mission time requirements. The next step is to determine the minimum fuel required that satisfies the mission time requirements and determine the feasibility of using the auxiliary engines subject to the fuel capacity constraints of the spacecraft.

B. THE MINIMUM FUEL, FIXED TERMINAL TIME PROBLEM

1. Problem Formulation

The auxiliary engine specifications as well as the initial and terminal boundary conditions remain the same as in the minimum time optimal control problem formulation. In this case, the problem is formulated as to minimize the fuel consumption over a fixed time horizon. The time horizon is constrained to 48 hours and represents the allowable window for the Orion spacecraft to conduct the TEI burns for an expedited return to earth. The goal was to find a feasible solution to the problem of conducting the return mission using solely the auxiliary engines. Because of the rocket characteristics, the auxiliary engine uses more fuel for a given duration of burn than does the main engine. This solution, if found, was to show that the spacecraft would have enough fuel onboard to conduct the return mission. Additionally, verification of the optimality of the solution is necessary.

Minimum Time Formulation

Where $\underline{x} = [x, y, z, v_x, v_y, v_z, m]^T$ and $\underline{u} = [T, \alpha, \beta]$,

$$\left\{ \begin{array}{ll} \text{Minimize} & J[x(\bullet), u(\bullet), t_f] = m_0 - m_f \\ \text{Subject to} & \dot{x} = v_x \\ & \dot{y} = v_y \\ & \dot{z} = v_z \\ & \dot{v}_x = -\ddot{x}_M - \frac{\mu_M x}{r_M^3} - \frac{\mu_E (x - x_E)}{r_E^3} - \frac{\mu_S (x - x_S)}{r_S^3} + \frac{T \cos \alpha \cos \beta}{m} \\ & \dot{v}_y = -\ddot{y}_M - \frac{\mu_M y}{r_M^3} - \frac{\mu_E (y - y_E)}{r_E^3} - \frac{\mu_S (y - y_S)}{r_S^3} + \frac{T \sin \alpha \cos \beta}{m} \\ & \dot{v}_z = -\ddot{z}_M - \frac{\mu_M z}{r_M^3} - \frac{\mu_E (z - z_E)}{r_E^3} - \frac{\mu_S (z - z_S)}{r_S^3} + \frac{T \sin \beta}{m} \\ & \dot{m} = -\frac{T}{v_e} \\ & \underline{x}(t_0) = \underline{x}^0, \underline{x}(t_f) = \underline{x}^f \\ & t_f - t_0 = 48 \text{ hrs}, m(t_f) \text{ is free} \\ & 0 \leq T \leq T_{\max} \end{array} \right.$$

2. Results and Analysis

Figures 30, 31, and 32 show the resulting control profiles for the minimum fuel problem. The problem was initially started using 30 LGL nodes and then bootstrapping the solution to a final solution using 300 LGL nodes. The goal was to balance computation time by limiting the number of nodes at the same time as achieving a smooth and viable control solution. As the number of LGL nodes was increased for each iteration of the solution, the control angles were forced to zero whenever the thrust was zero. This helped speed up the computation of the DIDO© results and was assumed that this would have no effect on the optimal solution since the control angles only influence the spacecraft trajectory whenever there is a thrust associated with them. The thrust

profile is similar to the main engine trajectory solved by Yan et al. in that it contains three distinct TEI maneuvers, with the second burn having the characteristics of a singular arc.

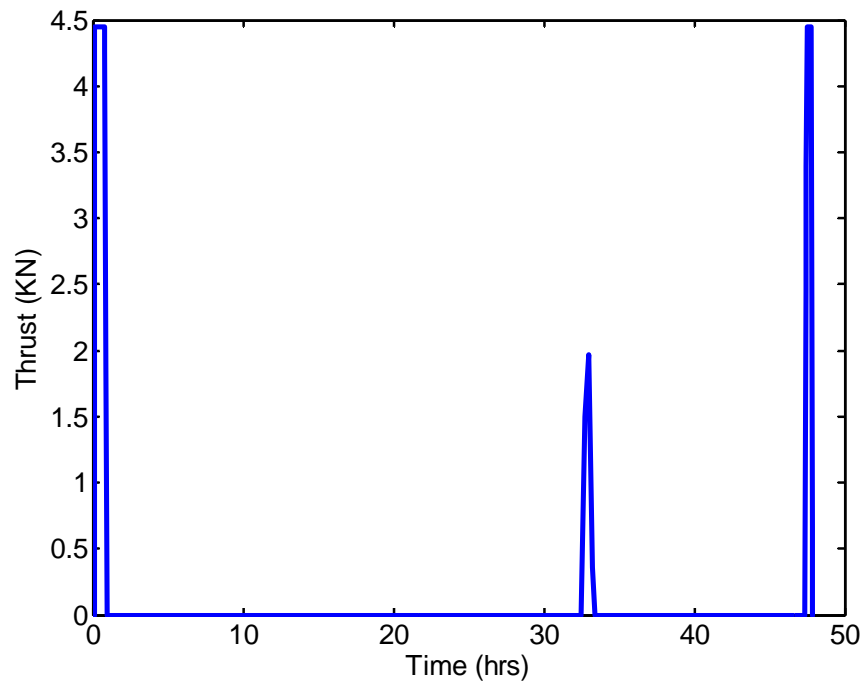


Figure 30. Thrust Control Structure

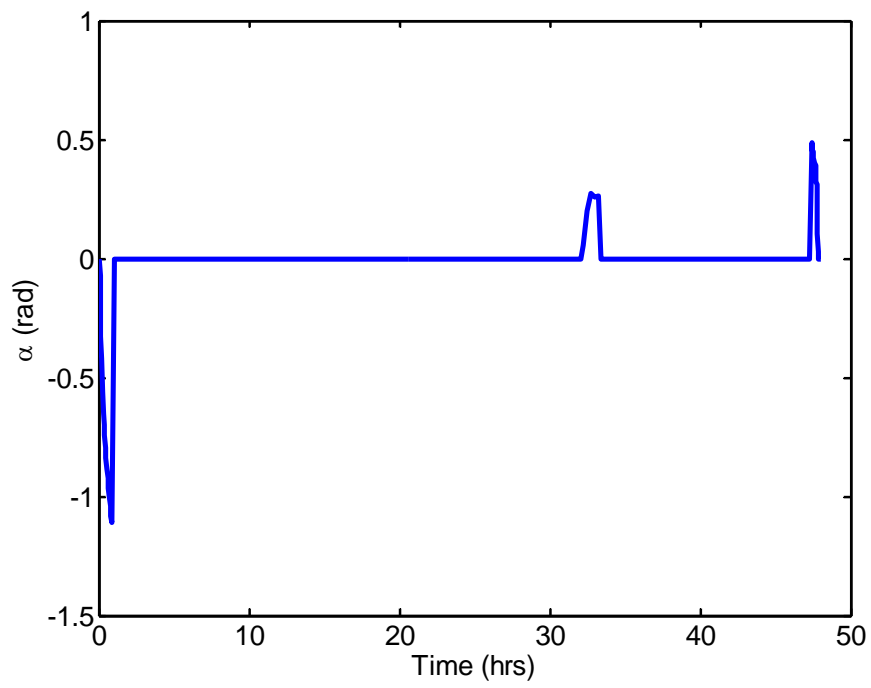


Figure 31. Azimuth Control Angle

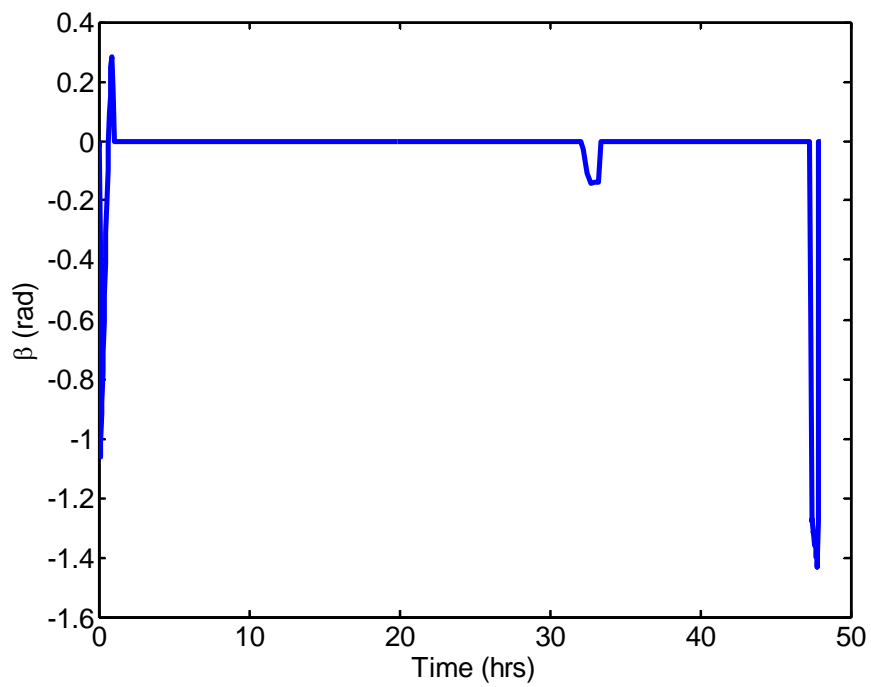


Figure 32. Elevation Control Angle

The entire series of maneuvers are completed within the bounded time horizon and, as depicted in Figure 33, uses a total of 7,215.6 kg of fuel, less than the given fuel capacity of the spacecraft which is 8,063.65 kg.

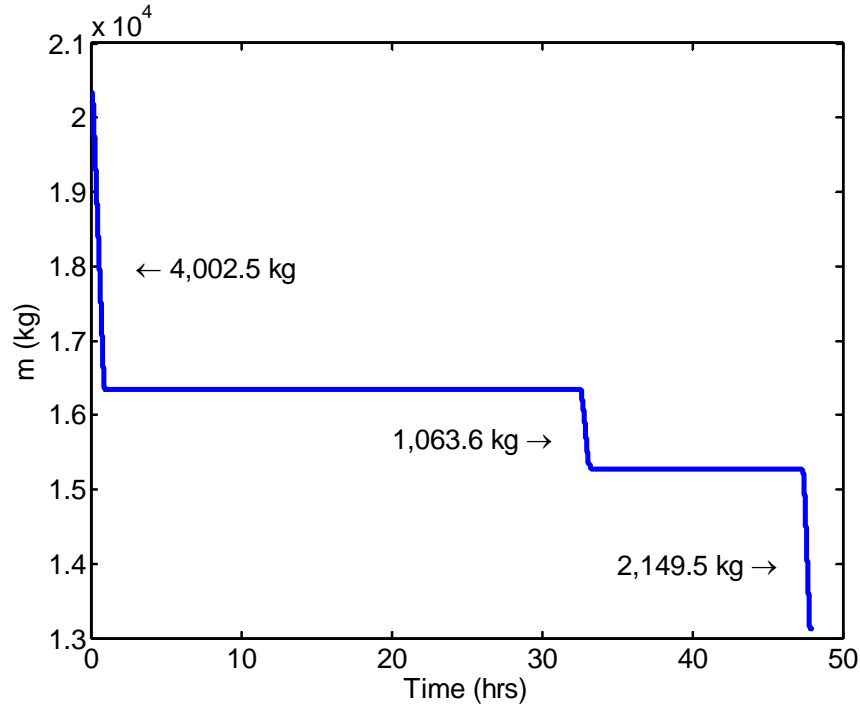


Figure 33. Fuel Consumption

a. Feasibility of the Solution

A feasibility analysis of the solution was conducted, similarly to the previous case, where the solution is propagated using the Matlab *ode45* function. The controls are interpolated over the propagated dynamics to see how well the discrete DIDO© solution maps to the integrated solution. Figures 34 and 35 illustrate that the displacement and tangential velocities of the discrete solution follow the propagated state trajectories. Some divergence exists towards the end of the trajectory due to numerical propagation errors. The difference in the terminal condition of the propagated solution and the DIDO© solutions are 502.1 km in displacement and 0.10 km/sec in velocity. The variation in final mass was approximately 0.1 kg. While DIDO© finds a solution that

meets the given boundary conditions, a resolution to the validation and verification of the results need be conducted since the propagated solution does not meet the displacement error and velocity error requirements of 1 km and 1 m/s respectively. These errors can be eliminated using the Bellman technique described in the minimum time problem. However, the initial analysis shows that since the propagated solution and discrete solutions are closely matched, the solution appears feasible.

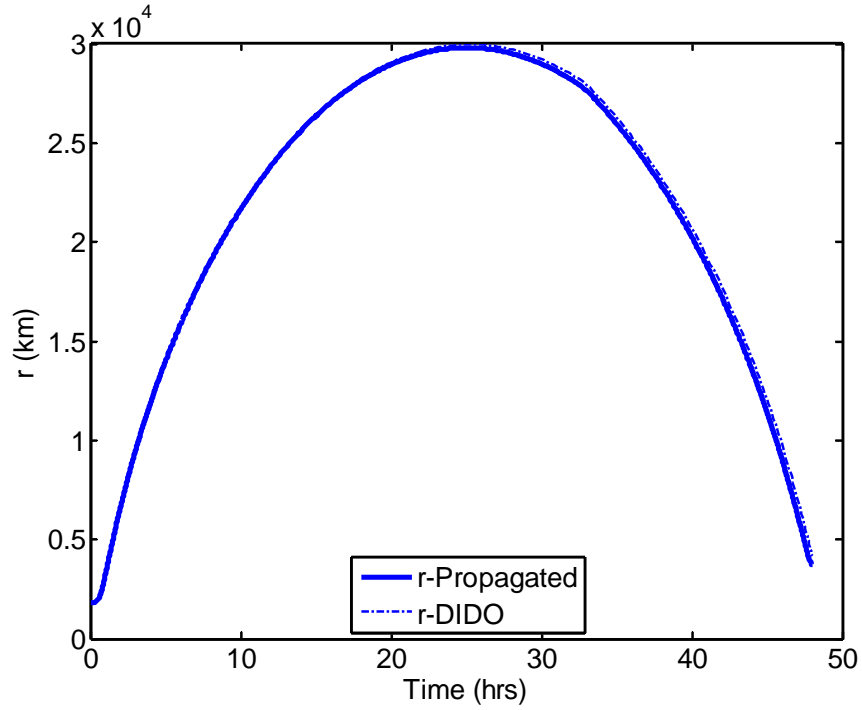


Figure 34. Displacement State Trajectory

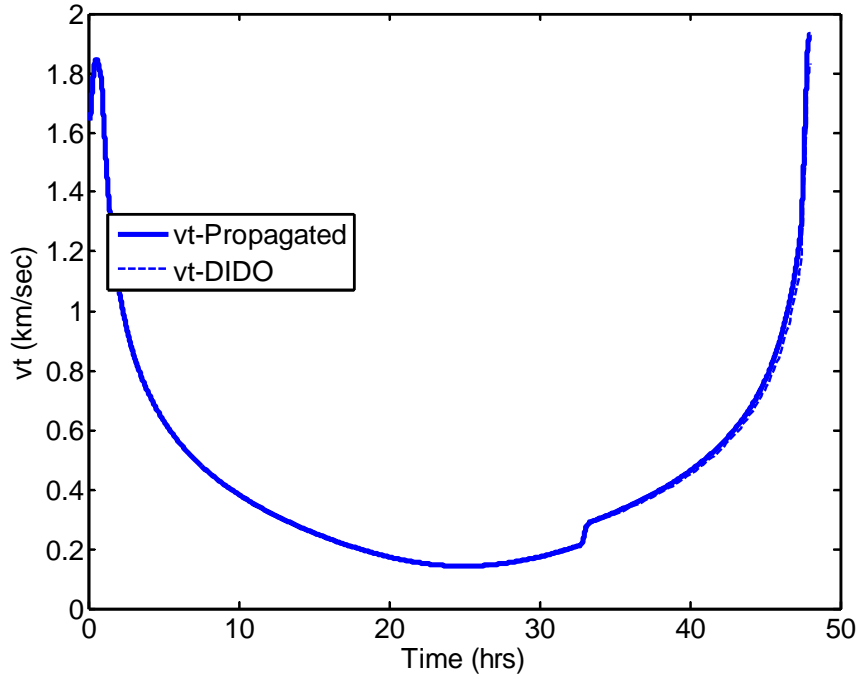


Figure 35. Velocity State Trajectory

Again, like the analysis performed in the minimum time problem, the evolution of the osculating orbital elements was investigated. In Figure 36, the semi-major axis changes primarily due to the first and last TEI burns. The first burn is an apoapsis raising maneuver and the final burn provides the kinetic energy required for the spacecraft to achieve escape velocity from the moon. In a parabolic trajectory, the semi-major axis is not defined, hence the singular spike in the figure. Figure 37 shows that the eccentricity of the orbit increases to a value greater than one, which means that the spacecraft departs the moon's orbit on a hyperbolic trajectory, requiring a transition through a parabolic trajectory where the eccentricity equals exactly one. Figure 38 shows an inclination change of about 15 degrees corresponding to the second, singular arc maneuver. The terminal values of the osculating orbital elements match those of the main engine TEI maneuver sequence (Yan et al., 2010). It should be noted that in each of the TEI burns, a combination of inclination and eccentricity changes is found. This appears to be the case since each of the maneuvers is finite in duration, rather than

impulsive. This effect is amplified because of the lower thrust engine which requires a longer burn time to perform a given maneuver than one with higher thrust.

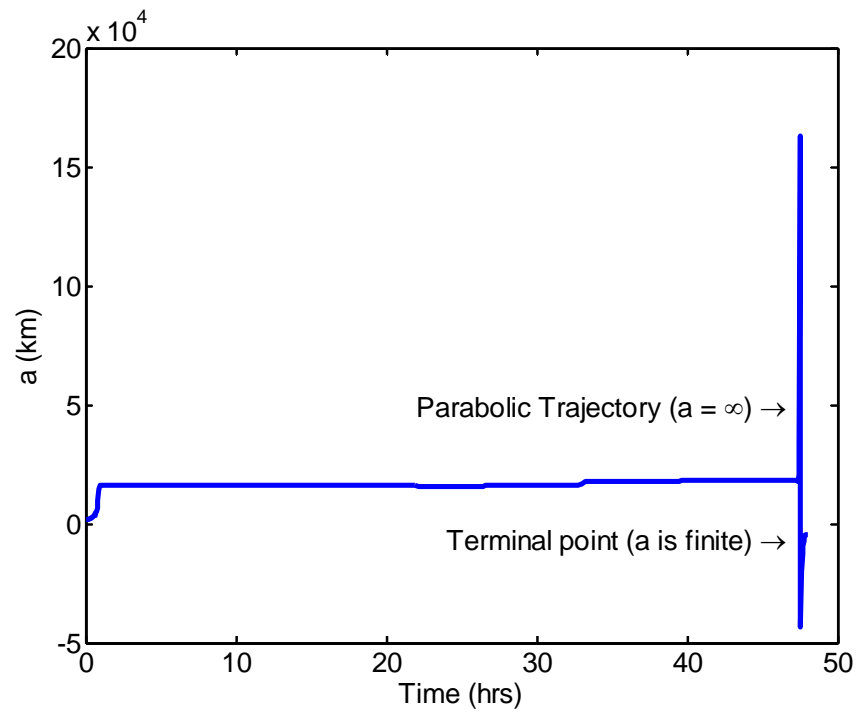


Figure 36. Semi-major Axis With Respect to Moon Centered Frame

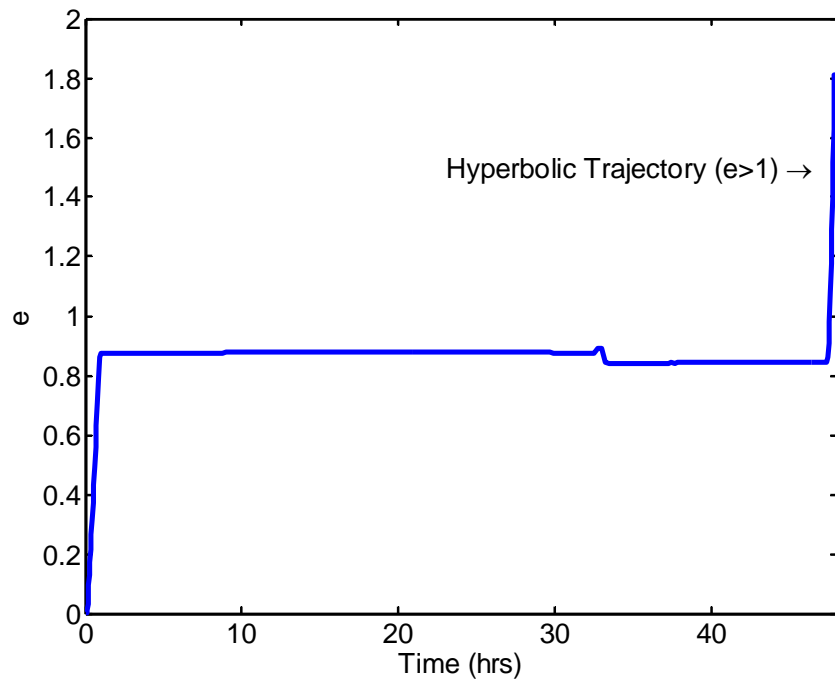


Figure 37. Eccentricity With Respect to Moon Centered Frame

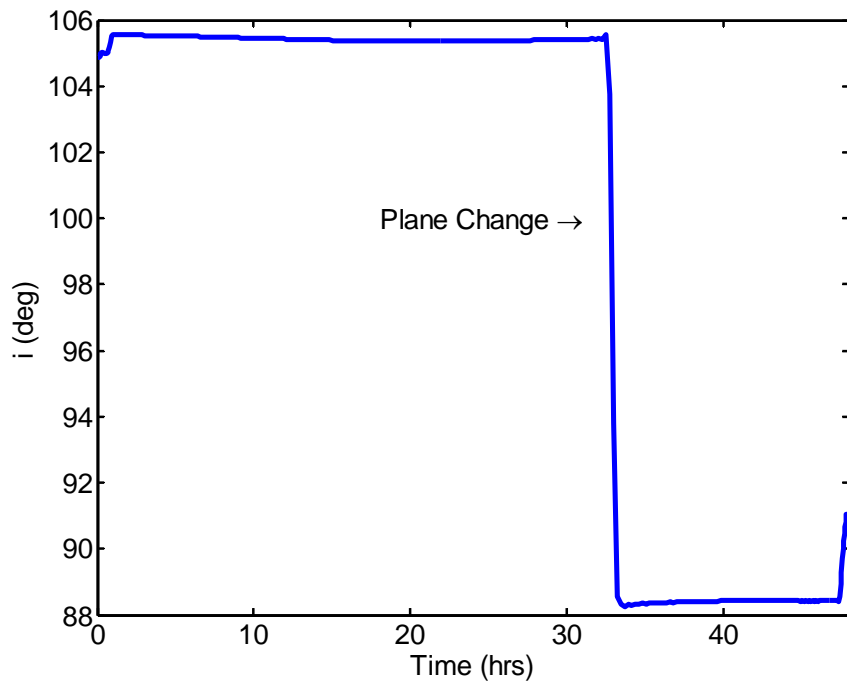


Figure 38. Inclination With Respect to Moon Centered Frame

A final check to ascertain the feasibility of the solution is to compare the final fuel consumption to the results from several authors who solved the same minimum fuel earth return problem using the same initial and final boundary conditions, but used different engine characteristics. In Yan et al., as previously described solve the problem using the main engine with a thrust of 33.6 kN and an Isp of 326 seconds. Park et al. used a rocket engine with a thrust of 3 kN and an Isp of 326 seconds. The results in Table 5 show the resulting fuel consumption of the present problem using only the auxiliary engines for the entire return mission compared to each of these cases. The fuel consumption value of 7,215.6 kg should be close to the value reached by Park with similar engine characteristics and greater than the main engine which with a higher thrust can perform the maneuvers with shorter burn durations and greater fuel efficiency (greater Isp).

Engine Configuration	Isp (sec)	LGL Nodes	Fuel Consumed (kg)
Auxiliary Engines (4.4 kN)	309	300	7,215.6
Auxiliary Engines (3 kN)	326	160	7,245.1
Main Engines (33.6 kN)	326	500	6,657.3

Table 5. Fuel Consumption Comparison

b. Verification of the Optimality of the Solution

Figures 39 and 40 show the Hamiltonian constant at a value of zero, and the transversality condition of the co-state related to mass equal to -1 at the terminal point.

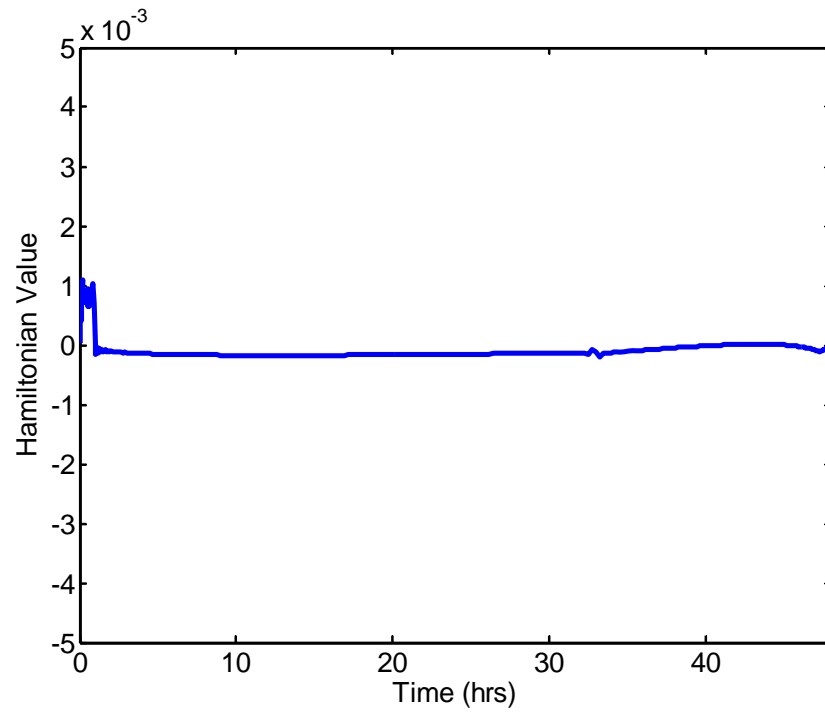


Figure 39. Hamiltonian Evolution

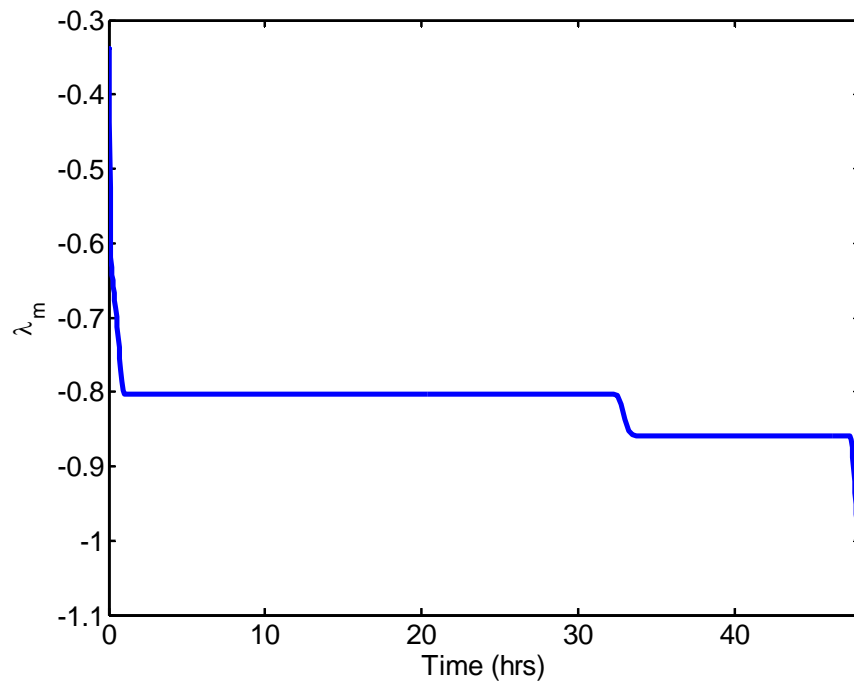


Figure 40. Co-state (λ_m) Evolution

Figure 41 shows the evolution of the switching function over the entire maneuver sequence. The switching function is negative for maximum thrust and positive for zero thrust, however at the singular arc the switching function also appears to be negative. The singular arc is demonstrated to be optimal by examining the derivatives of the switching function up to the fourth derivative. Figure 42 shows that the fourth derivative is equal to zero during the singular arc. The generalized Legendre-Clebesch convexity condition during the singular arc burn is shown in Figure 43. Figure 44 is included solely to demonstrate that it is possible to have regions where the Legendre-Clebesch condition is non-positive.

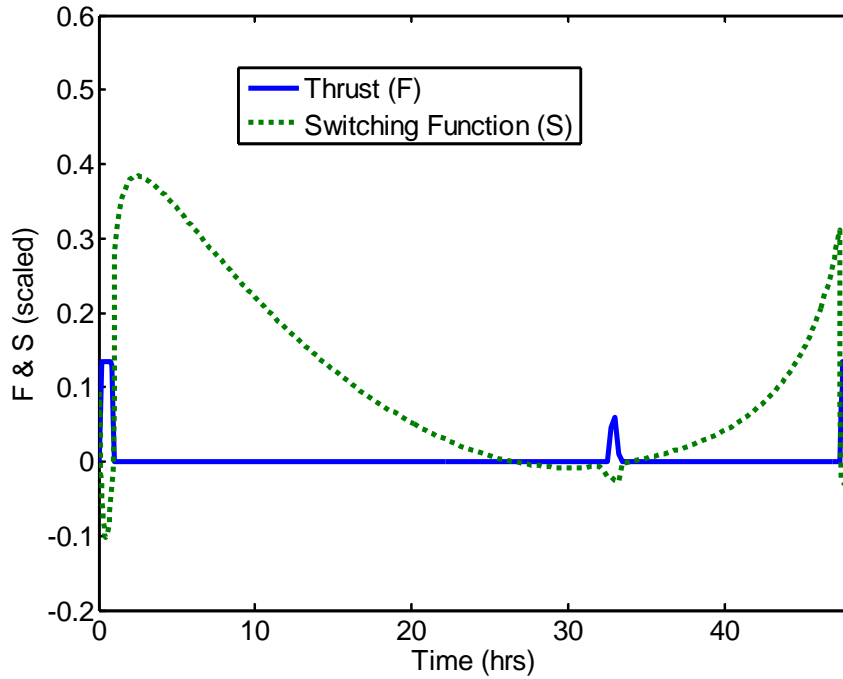


Figure 41. Thrust and Switching Function

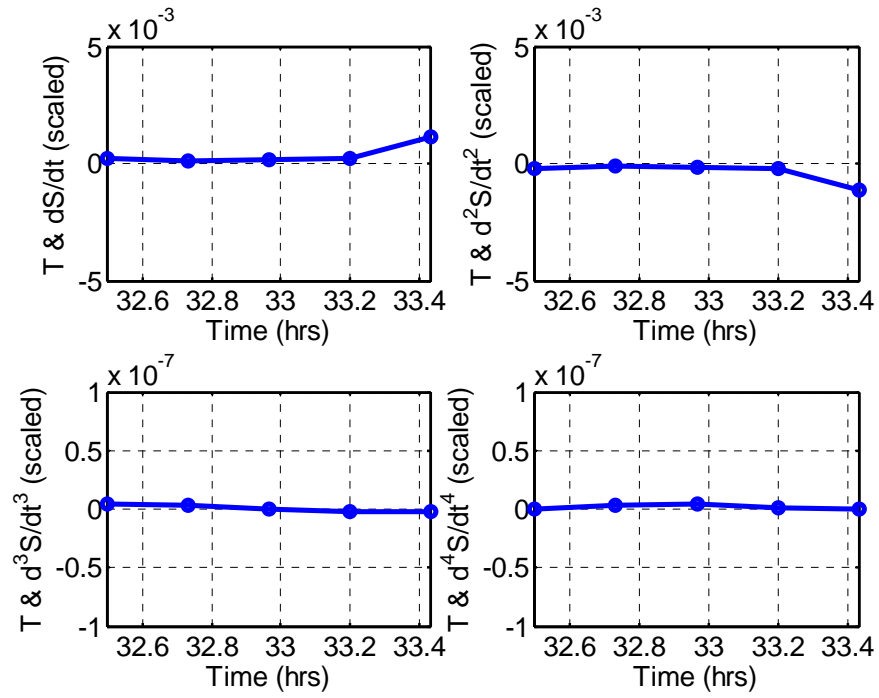


Figure 42. Derivatives of the Switching Function During Singular Arc

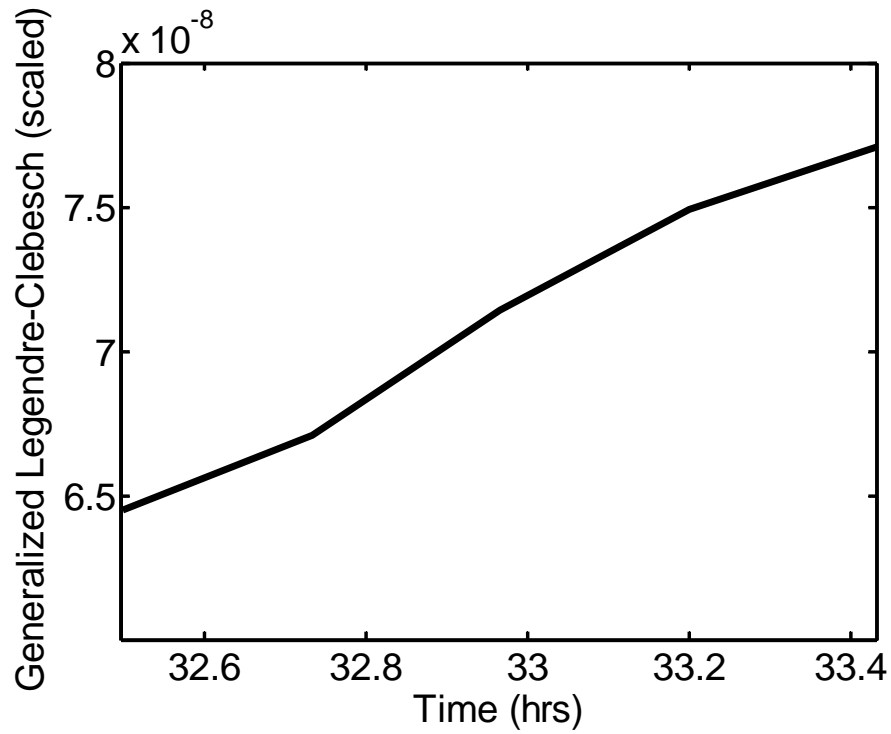


Figure 43. Generalized Legendre-Clebsch Condition During Singular Arc

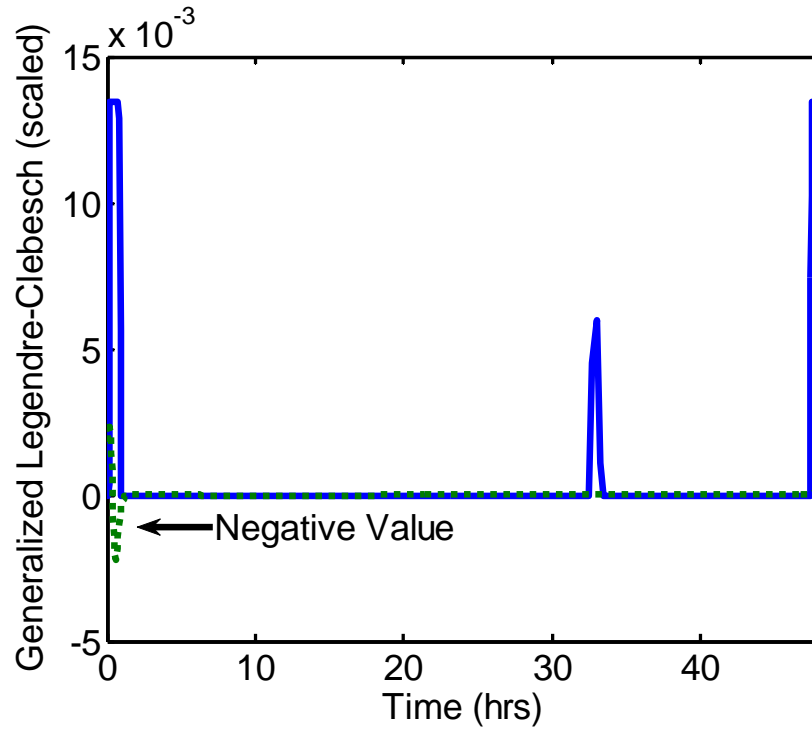


Figure 44. Generalized Legendre-Clebesch Condition Over Entire Trajectory

Figures 45, 46, and 47 show in detail the features of the TEI burns; they show the thrust and control angles and also that for each burn, the primer angle between the thrust and the velocity co-vector is equal to 180 degrees as necessary to meet the Hamiltonian Minimization Condition. With the exception of the sparse nature of the control trajectory of the second, singular TEI burn, the control solution appears smooth enough for a control solution. From a practical control perspective, however, it is desired to increase the fidelity of the discrete solutions into a more continuous solution.

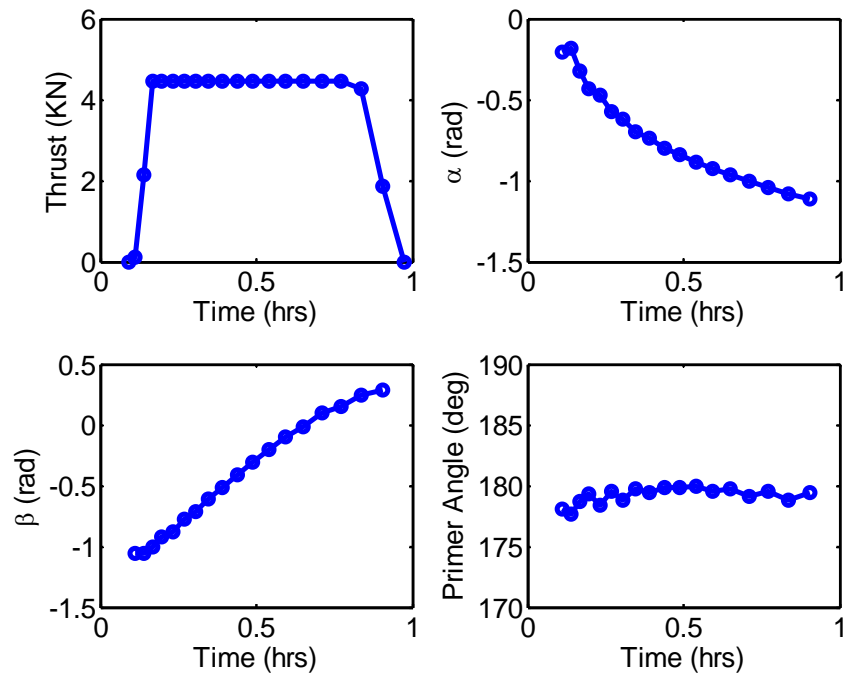


Figure 45. First TEI Burn

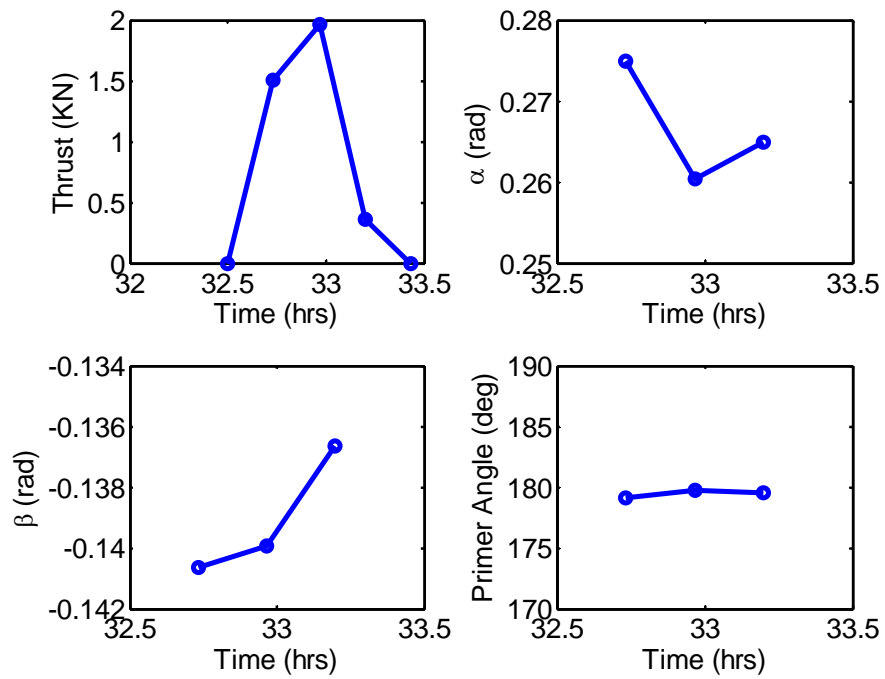


Figure 46. Second TEI Burn

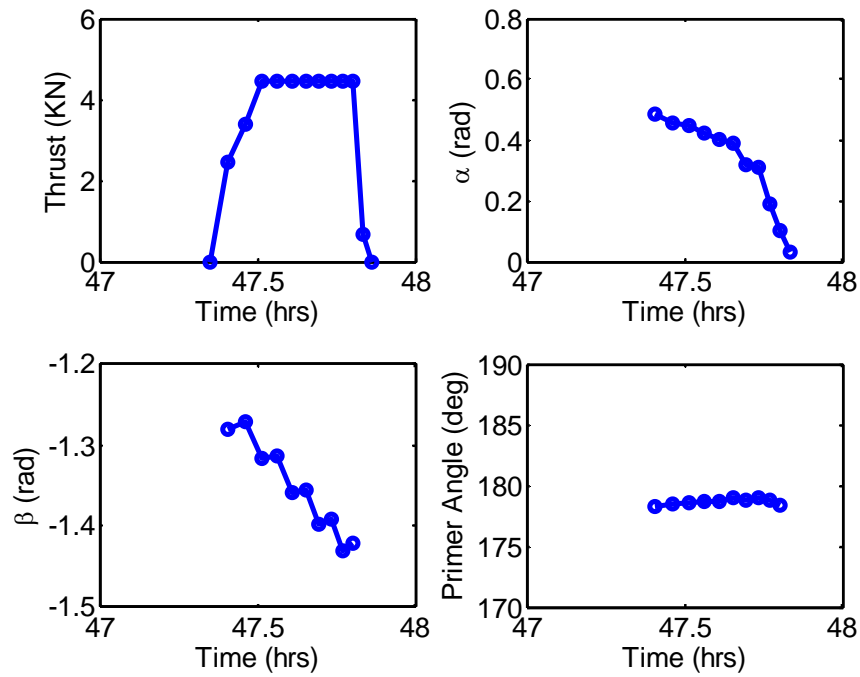


Figure 47. Third TEI Burn

As pointed out in the feasibility analysis, the final displacement and velocity errors are due to the interpolation errors propagated over a long time horizon. Figures 48 and 49 show how the error between the DIDO© solution and the interpolated solution increases over the entire solution trajectory. Using the Pseudospectral Bellman Technique used by Ross et al., and demonstrated in the minimum time problem, it is possible to minimize the errors caused by interpolation of the controls.

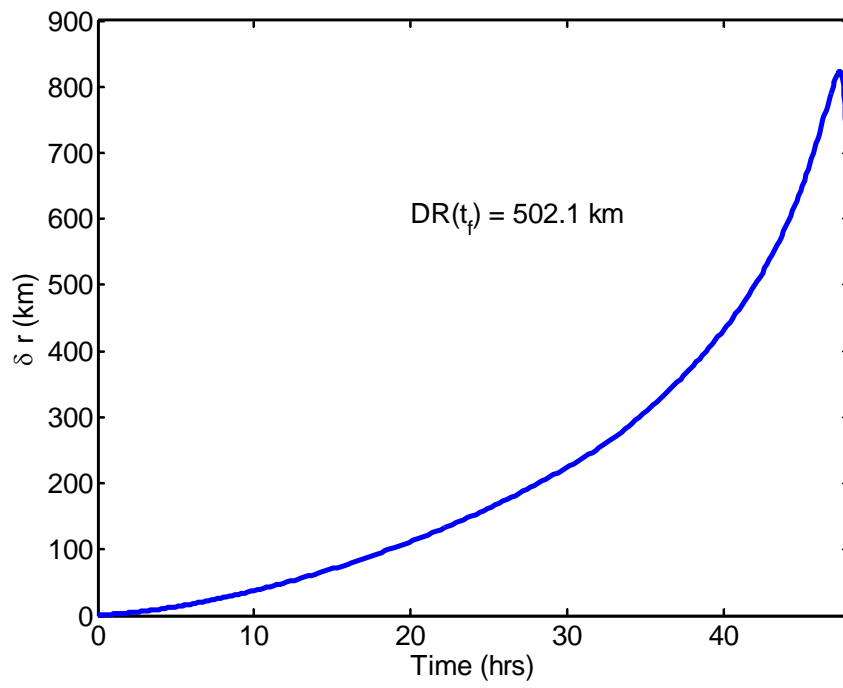


Figure 48. Displacement Error

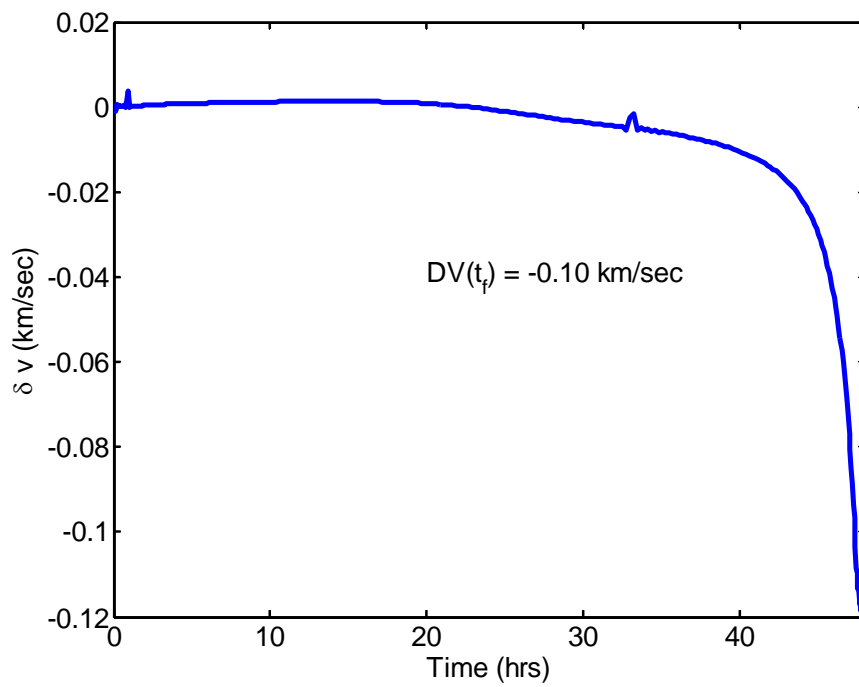


Figure 49. Velocity Error

C. CONCLUSIONS FOR USE OF AUXILIARY ENGINES FOR RETURN MISSION

The resulting optimal control trajectory shows that in the event of a total main engine failure, the auxiliary engines could be used for the entire return mission, meeting the 48-hour minimum time requirement to complete the third TEI maneuver. Additionally, the fuel optimal solution shows that 7,215.6 kg is the theoretical minimum required fuel to be carried onboard, not including any design margins. This result then potentially reduces the total amount of fuel required, thus freeing up additional mass for other aspects of the spacecraft design.

VI. MAIN ENGINE SINGULAR ARC ANALYSIS

The Yan et al. results for the minimum fuel solution for the earth return mission using the main engines, they found a singular arc as part of the control trajectory for the second TEI maneuver. In their solution, the singular burn is made up of only three distinct, non-zero thrust points. Since a high fidelity control solution is desired, it would be advantageous to have additional points from which to approximate a continuous solution. As a secondary investigation, NASA is interested in determining the feasibility of using the auxiliary engines in place of the main engines for the singular arc TEI maneuver. Therefore, the purpose of the singular arc study is to:

- (1) Generate a higher fidelity control solution from the existing singular arc data generated by Yan et al.
- (2) Determine the feasibility of using the auxiliary engines for the singular arc and ascertain the fuel penalty if any
- (3) Verify and validate the necessary conditions for optimality for any feasible solution(s) generated

The separation between the nodes from the original main engine solution is due primarily to its location along the entire trajectory solution. The output data points from DIDO© are non-uniformly spaced, being more dense at the beginning and end of the trajectory and sparse in the middle. The singular arc was in the sparse region of the original solution covering a time span of approximately 29 minutes. The data points around the singular arc were spaced approximately 7 minutes apart as compared to the points around the final TEI burn had a spacing range of approximately 0.4 to 0.8 minutes between them. The approach therefore was to examine the singular arc by fixing boundary conditions close to and around the start and completion of the maneuver. Since the goal is to increase the number of discrete points for a solution with higher resolution,

the problem uses a small number of LGL nodes to compute a solution and then using the bootstrap technique to increase the nodes until the control trajectories converge in a smooth fashion.

Recalling that the Bellman Principle of Optimality states that along a given optimal trajectory, a segment starting from some intermediate point on that trajectory and ending at the original termination point will also be optimal. It says nothing about an intermediate segment. Suppose there are two points, C and D , forming a segment along the same optimal trajectory. Even though the original optimal trajectory can pass through these points, it does not mean that the original path on \overline{AB} between them is optimal on the path between C and D . There exists an optimal path \overline{CD} that may not lie on \overline{AB} as shown in Figure 50. If the minimized cost along \overline{AB} is J_0 , and the sum of the segments on \overline{AB} is $J_0 = J_1 + J_2 + J_3$, then the cost of an optimal trajectory \overline{CD} not on \overline{AB} must be $J_2' \geq J_2$. Put another way, $J_1 + J_2 + J_3 \leq J_1 + J_2' + J_3$.

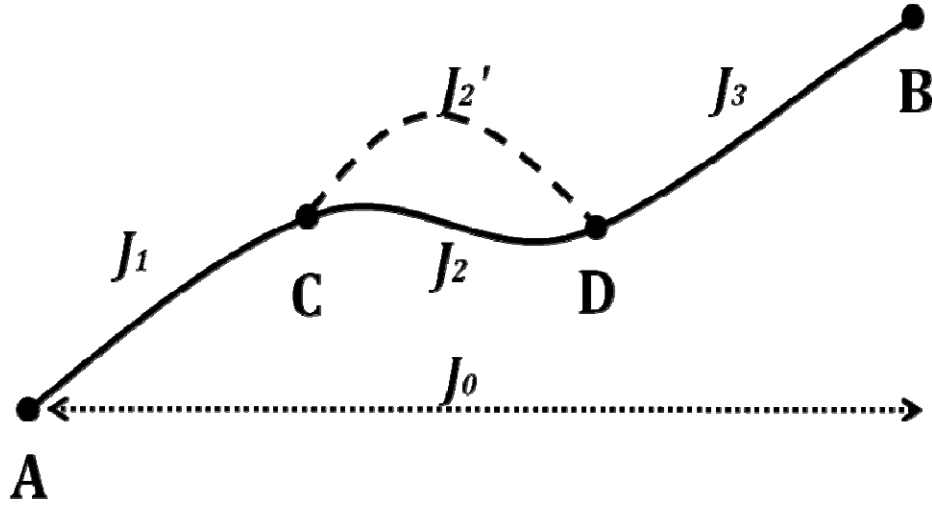


Figure 50. Bellman Curve and Segment

The singular arc generated from the Yan et al. solution can be said to lie on a segment of a fuel-optimal trajectory. In order to maintain the same cost along that segment, so that from the example above, $J_2' = J_2$, then the dashed line trajectory must lie on the solid line \overline{CD} . This implies that the segment has fixed state and time horizon boundaries and the control and state trajectories will lie on the original trajectory. In the problem formulation in DIDO© this poses a difficulty since to solve an optimal control problem, one needs to determine the cost to be minimized. If both mass (part of the state) and time are fixed boundary conditions, then there is no cost to minimize. Therefore, the problem was formulated to minimize the final fuel cost, fixing the initial boundary condition at some $\bar{x}_0 = [x^0, y^0, z^0, v_x^0, v_y^0, v_z^0, m^0,]$ and the final boundary condition at some $\bar{x}_f = [x^f, y^f, z^f, v_x^f, v_y^f, v_z^f]$ such that the initial and final states are relatively close to the initiation and termination of the maneuver. This problem is solved with the knowledge that an optimal solution can be found on the segment, but that the cost can be no less than the segment on the original optimal path.

A total of six experiments were run, using three different sets of boundary conditions each associated with a different time horizon around the original singular arc (TH1, TH2, and TH3). For each specified time horizon, DIDO© was supplied with two initial guesses to choose from: (1) the original, coarse solution bound by the time horizon, and (2) a two-point guess using only the initial and final nodes of the original primal solution bounded by the time horizon. Figure 51 shows the thrust profile for the singular arc in the original main engine solution and the three time horizons examined.

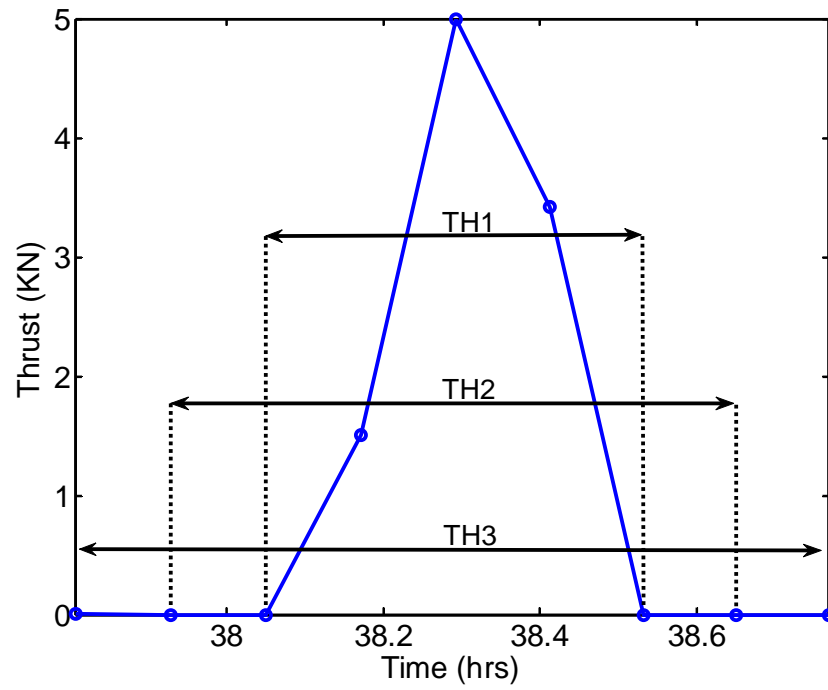


Figure 51. Three Time Horizons Around Original Main Engine Singular Arc

The spacecraft main engine characteristics (Scarritt et al., 2009) and fixed initial and terminal conditions are as follows:

- Main Engine Thrust: 33,631.6621 N
- Main Engine Isp: 326 sec
- Initial and terminal boundary conditions for TH1

$$\begin{bmatrix} x_0 \\ y_0 \\ z_0 \\ v_{x0} \\ v_{y0} \\ v_{z0} \\ m_0 \end{bmatrix} = \begin{bmatrix} -3,130.762702562802 \text{ km} \\ -5,554.427470301326 \text{ km} \\ 23,156.51130870926 \text{ km} \\ -0.073217640485400 \text{ km/sec} \\ 0.189457232407054 \text{ km/sec} \\ -0.246837168808192 \text{ km/sec} \\ 16,799.81436532424 \text{ kg} \end{bmatrix} \quad \begin{bmatrix} x_f \\ y_f \\ z_f \\ v_{xf} \\ v_{yf} \\ v_{zf} \\ m_f \end{bmatrix} = \begin{bmatrix} -3,069.163608399203 \text{ km} \\ -5,150.061768188334 \text{ km} \\ 22,667.78130088386 \text{ km} \\ 0.173269593413525 \text{ km/sec} \\ 0.288498099224656 \text{ km/sec} \\ -0.324760205524167 \text{ km/sec} \\ \text{Free} \end{bmatrix}$$

- Initial and terminal boundary conditions for TH2

$$\begin{bmatrix} x_0 \\ y_0 \\ z_0 \\ v_{x0} \\ v_{y0} \\ v_{z0} \\ m_0 \end{bmatrix} = \begin{bmatrix} -3,098.602243204757 \text{ km} \\ -5,637.287708143786 \text{ km} \\ 23,263.91379554111 \text{ km} \\ -0.073590413655685 \text{ km/sec} \\ 0.188562680976605 \text{ km/sec} \\ -0.243173237675902 \text{ km/sec} \\ 16,799.81436532424 \text{ kg} \end{bmatrix} \quad \begin{bmatrix} x_f \\ y_f \\ z_f \\ v_{xf} \\ v_{yf} \\ v_{zf} \\ m_f \end{bmatrix} = \begin{bmatrix} -2,995.8032622945048 \text{ km} \\ -5,026.665289857207 \text{ km} \\ 22,528.09830807556 \text{ km} \\ 0.169676878511166 \text{ km/sec} \\ 0.287787468988926 \text{ km/sec} \\ -0.327515426089892 \text{ km/sec} \\ \text{Free} \end{bmatrix}$$

- Initial and terminal boundary conditions for TH3

$$\begin{bmatrix} x_0 \\ y_0 \\ z_0 \\ v_{x0} \\ v_{y0} \\ v_{z0} \\ m_0 \end{bmatrix} = \begin{bmatrix} -3,066.151333338768 \text{ km} \\ -5,720.134711415117 \text{ km} \\ 23,370.19755922657 \text{ km} \\ -0.073812293999072 \text{ km/sec} \\ 0.187756011321829 \text{ km/sec} \\ -0.239609189112516 \text{ km/sec} \\ 16,798.21977554951 \text{ kg} \end{bmatrix} \quad \begin{bmatrix} x_f \\ y_f \\ z_f \\ v_{xf} \\ v_{yf} \\ v_{zf} \\ m_f \end{bmatrix} = \begin{bmatrix} -2,923.002666940919 \text{ km} \\ -4,903.646847991885 \text{ km} \\ 22,387.55942551430 \text{ km} \\ 0.171736936444797 \text{ km/sec} \\ 0.289275403273065 \text{ km/sec} \\ -0.331764528528468 \text{ km/sec} \\ \text{Free} \end{bmatrix}$$

Theoretically, the initial mass for each of time horizon should be the same, since from the original solution the thruster is not firing, thus not burning fuel at the first three nodes of TH3. The differences come from the sensitivity of the scaled mass values. The scaled initial mass value for TH3 starts to differ at the fourth significant digit and results in a difference of about 1.6 kg.

- TH1 and TH2 Initial Mass = 0.825953636218675
- TH3 Initial Mass = 0.825875239089155

A. PROBLEM FORMULATION

The problem formulations for each time horizon are identical, with only the initial and terminal boundary conditions changed for each case. For each case, two different initial guesses were provided, which in each case influenced the final solution.

Minimum Time Formulation

Where $\underline{x} = [x, y, z, v_x, v_y, v_z, m]^T$ and $\underline{u} = [T, \alpha, \beta]$,

$$\left\{ \begin{array}{ll} \text{Minimize} & J[x(\cdot), u(\cdot), t_f] = m_f \\ \text{Subject to} & \dot{x} = v_x \\ & \dot{y} = v_y \\ & \dot{z} = v_z \\ & \dot{v}_x = -\ddot{x}_M - \frac{\mu_M x}{r_M^3} - \frac{\mu_E (x - x_E)}{r_E^3} - \frac{\mu_S (x - x_S)}{r_S^3} + \frac{T \cos \alpha \cos \beta}{m} \\ & \dot{v}_y = -\ddot{y}_M - \frac{\mu_M y}{r_M^3} - \frac{\mu_E (y - y_E)}{r_E^3} - \frac{\mu_S (y - y_S)}{r_S^3} + \frac{T \sin \alpha \cos \beta}{m} \\ & \dot{v}_z = -\ddot{z}_M - \frac{\mu_M z}{r_M^3} - \frac{\mu_E (z - z_E)}{r_E^3} - \frac{\mu_S (z - z_S)}{r_S^3} + \frac{T \sin \beta}{m} \\ & \dot{m} = -\frac{T}{v_e} \\ & \underline{x}(t_0) = \underline{x}^0, \underline{x}(t_f) = \underline{x}^f \\ & m(t_f) \text{ is free} \\ & 0 \leq T \leq T_{\max} \end{array} \right.$$

B. TH1 RESULTS

Solving this problem using the TH1 boundary conditions and supplying two different initial guesses to DIDO© results in two different solutions, each satisfying the necessary conditions for optimality. The solutions are each solved up to 80 LGL points each. Comparing the two cases, the control and state trajectories differ between the fixed boundary conditions, however both use the same amount of fuel. Figures 52, 53, and 54

show the resulting control trajectories compared to the initial guess trajectory provided. Note that the coarse guess is the same trajectory given by the original problem using the main engine. Also, the differences in the fuel consumed are negligible as shown in Table 6. The solutions for each of the time horizons are compared against the original coarse solution for the corresponding time horizon. The fuel consumed for each region has differences due to numerical variations of the scaled mass in the original coarse solution, therefore the fuel consumed in each of the regions appear to have different values. In scaled units the differences are small between the time horizons.

	Fuel Consumed (kg)	Variation
Original Coarse Solution	1,360.2	—
Using Coarse Guess	1,361.0	0.0006 %
Using 2-point Guess	1,361.2	0.0007 %

Table 6. TH1 Fuel Consumption

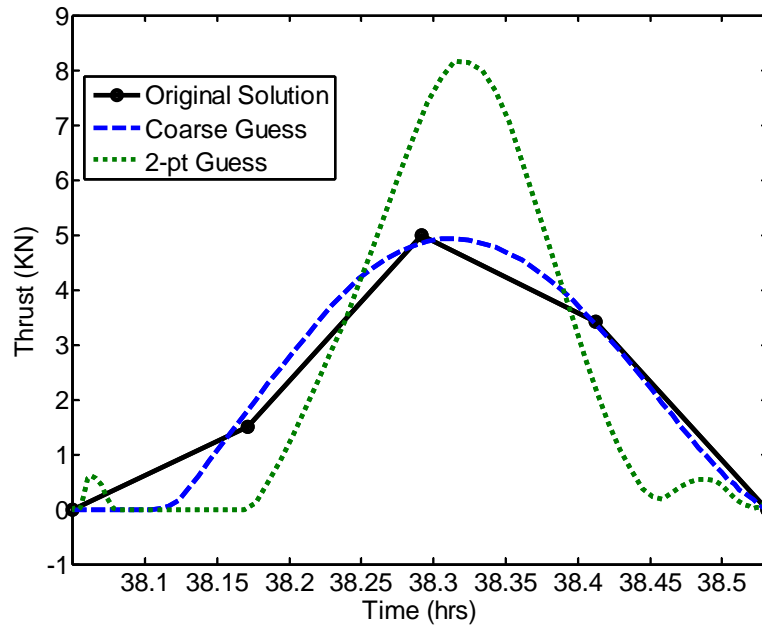


Figure 52. Thrust Trajectories for TH1

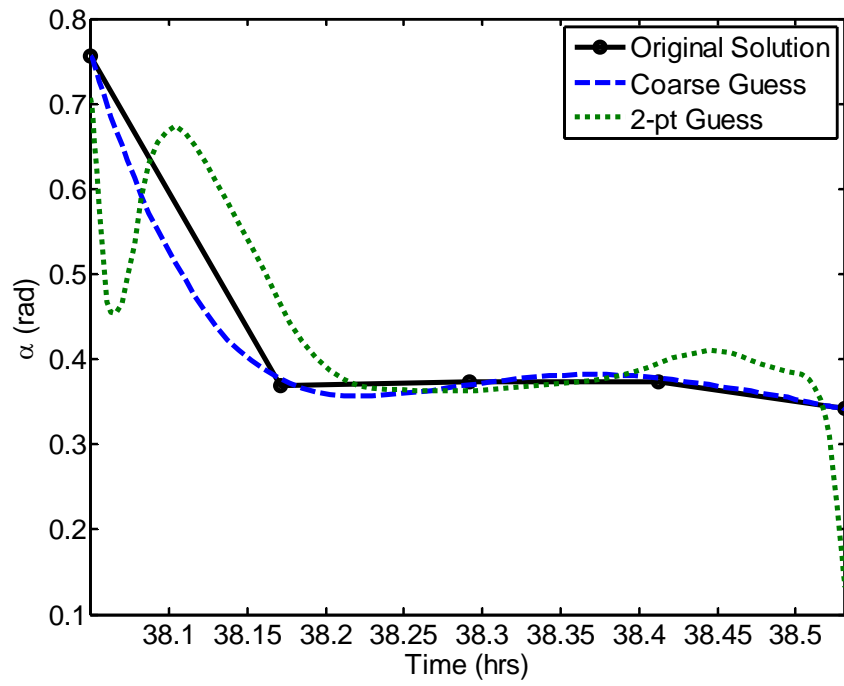


Figure 53. Azimuth Angle Trajectories for TH1

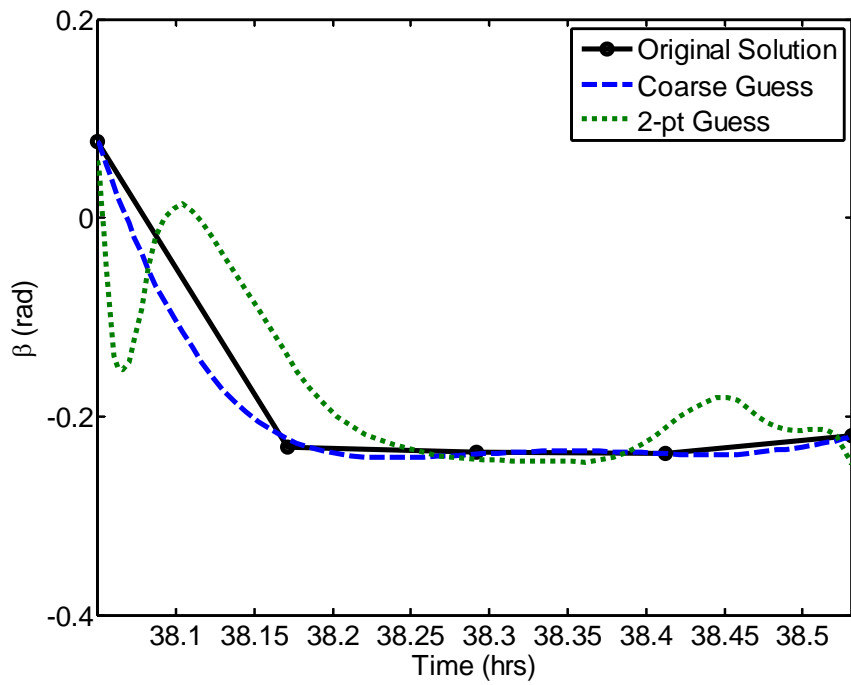


Figure 54. Elevation Angle Trajectories for TH1

Of note is the aliasing that occurs when the initial coarse solution is used as an initial guess (Ross, I.M., Gong, Q., and Sehkavat, P., 2007). The higher fidelity solution follows closely with the original solution. Similarly, the state trajectories are also closely aliased when given the original solution. Using the two-point guess, the state and control trajectories deviate from the original solution; however, the final minimized cost is the same. Therefore, both of these solutions appear feasible and as described below they both meet the necessary conditions for optimality.

Figures 55, 56, and 57 show that the Hamiltonian is constant, the end point transversality condition is met, and the primer angle is equal to 180 degrees and thus, the Hamiltonian Minimization Conditions are met. Additionally, both solutions meet the necessary conditions for optimality for singular arcs and the Legendre-Clebsch condition as shown in Figures 58–63.

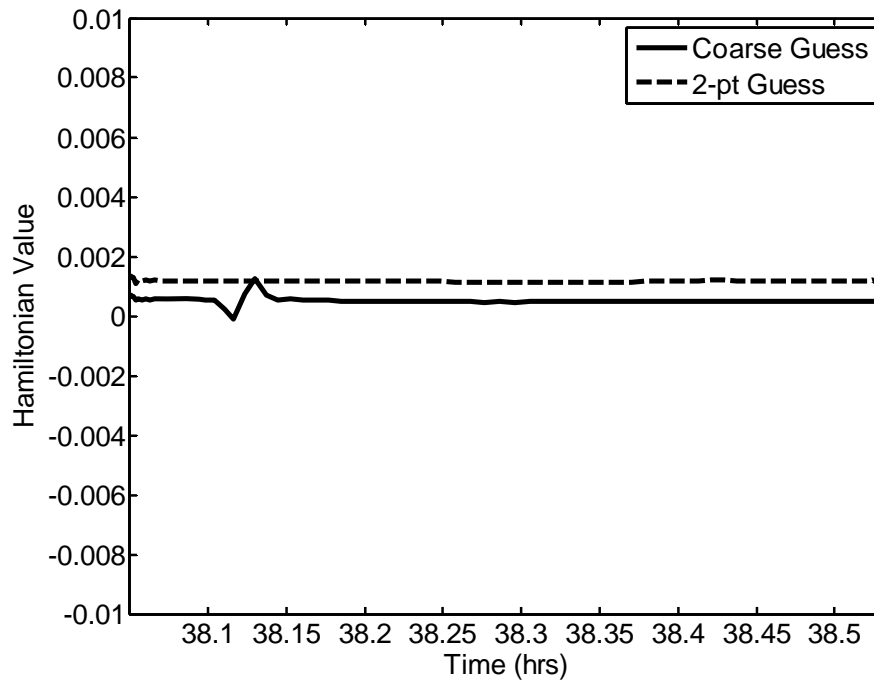


Figure 55. Hamiltonian Evolution (TH1)

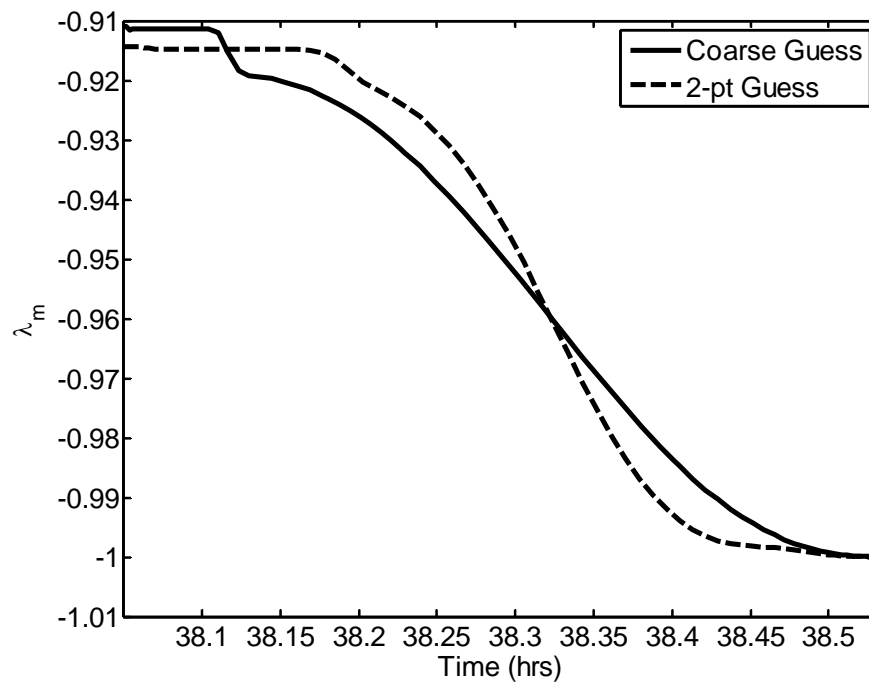


Figure 56. End-point Transversality Condition (TH1)

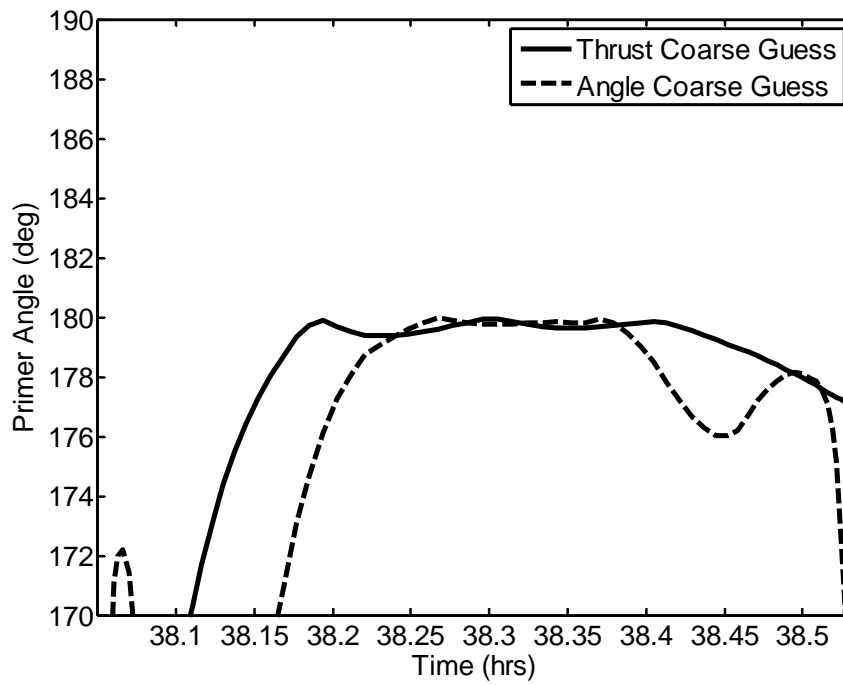


Figure 57. Primer Angle (TH1)

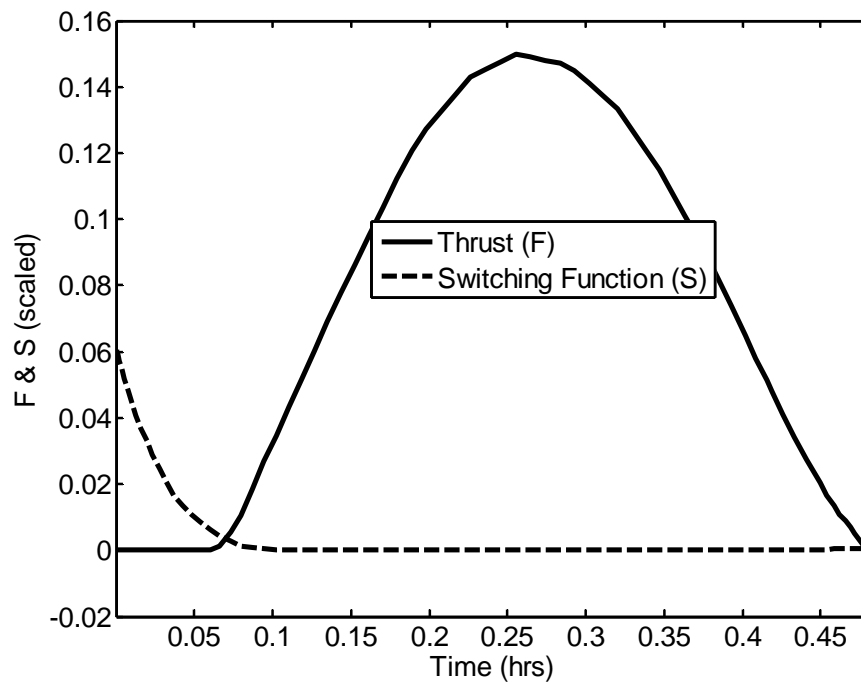


Figure 58. Switching Function For Coarse Guess Solution

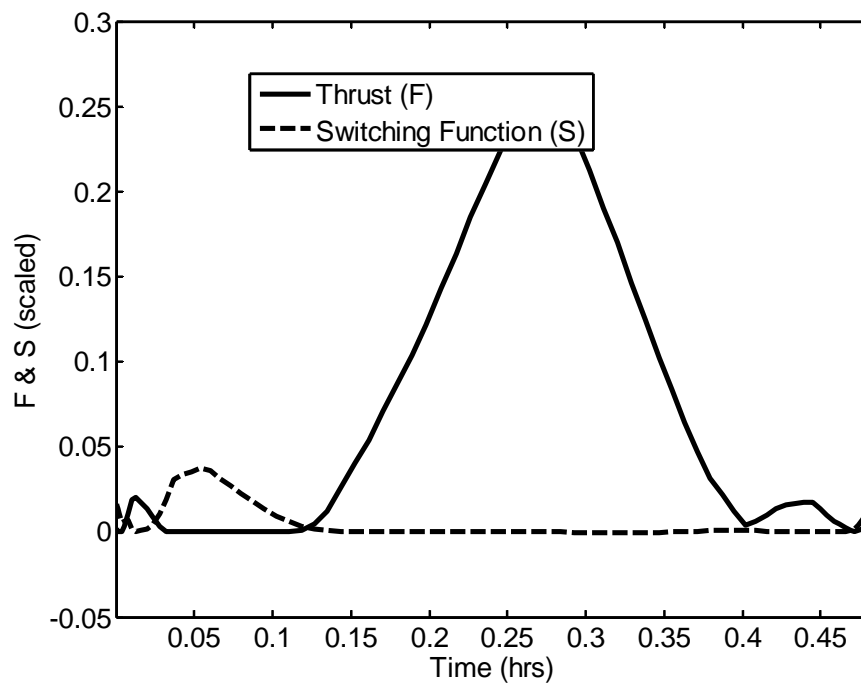


Figure 59. Switching Function for 2-Point Guess Solution

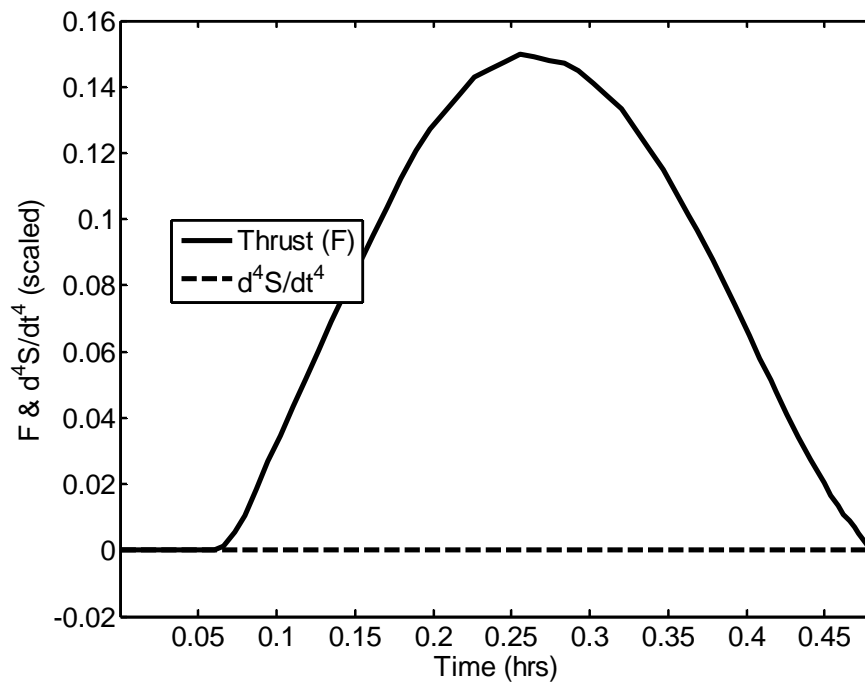


Figure 60. Fourth Time Derivative of Switching Function for Coarse Guess Solution

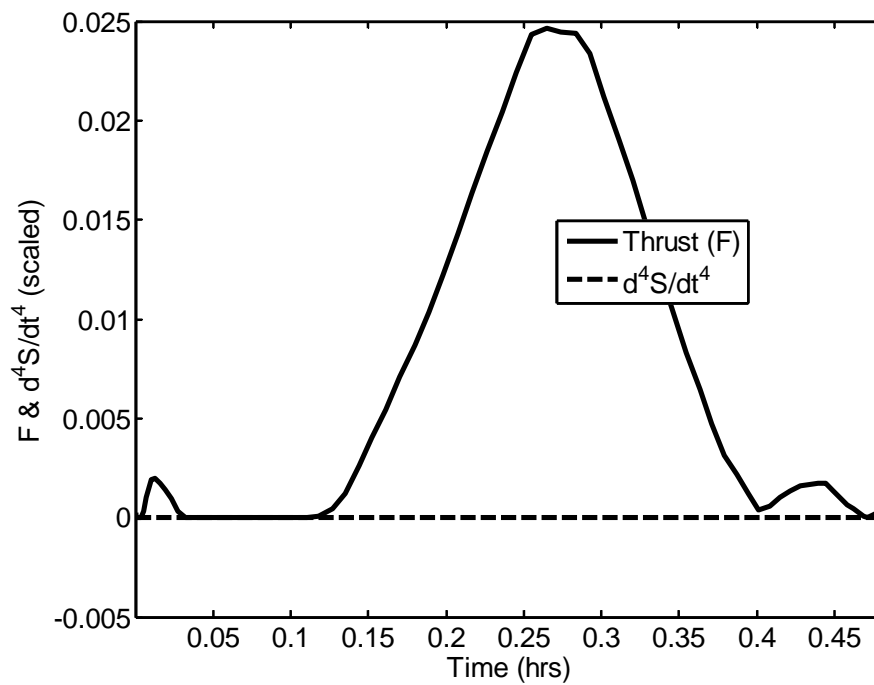


Figure 61. Fourth Time Derivative of Switching Function for 2-Point Guess Solution

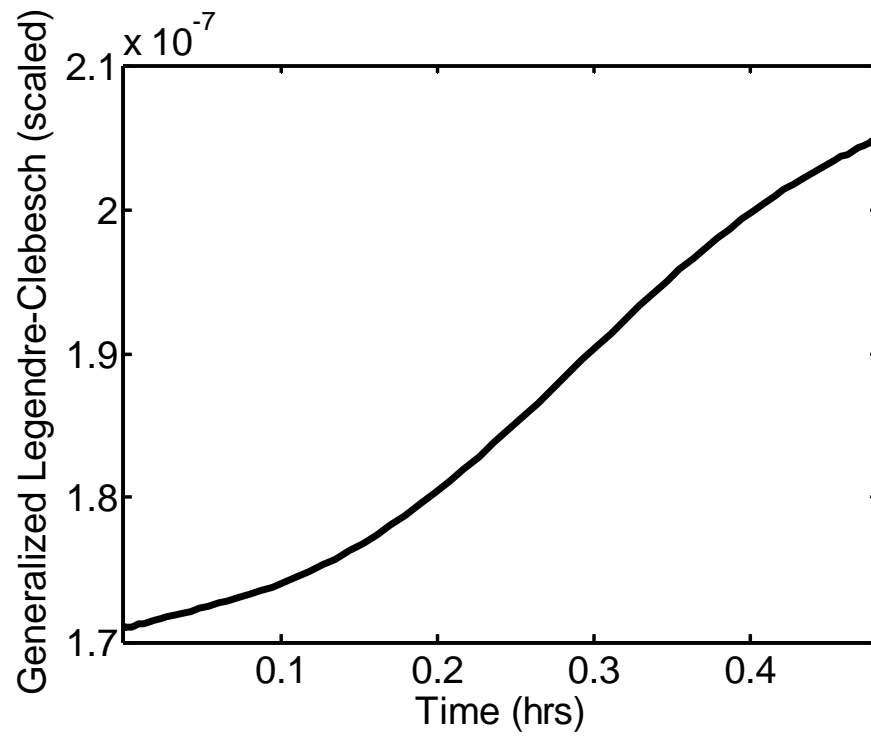


Figure 62. Generalized Legendre-Clebsch Condition for Coarse Guess Solution

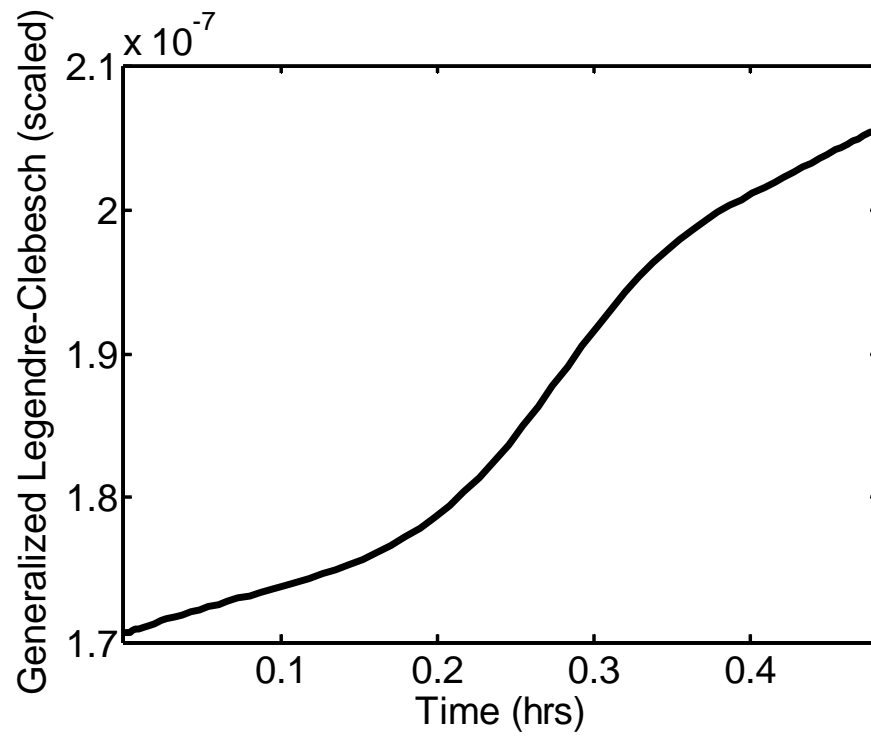


Figure 63. Generalized Legendre-Clebsch Condition for 2-Point Guess Solution

Examination of the state vector trajectories shows that each of the two cases for the TH1 bounds start and complete the maneuver at the specified state boundary conditions. While the final mass was not posed as a constraint on the problem, the resulting final mass is the same as in the original main engine problem within very tight tolerances. In Figures 64 and 65, the position and velocity state vector trajectories for the TH1 singular arc problem are shown and are described below. The position, or displacement, state trajectories differ slightly, however the velocity state trajectories are more varied due to the immediate relationship between thrust and change in velocity.

$$\bar{r} = \sqrt{\bar{x}^2 + \bar{y}^2 + \bar{z}^2}$$

$$\bar{v} = \sqrt{\bar{v}_x^2 + \bar{v}_y^2 + \bar{v}_z^2}$$

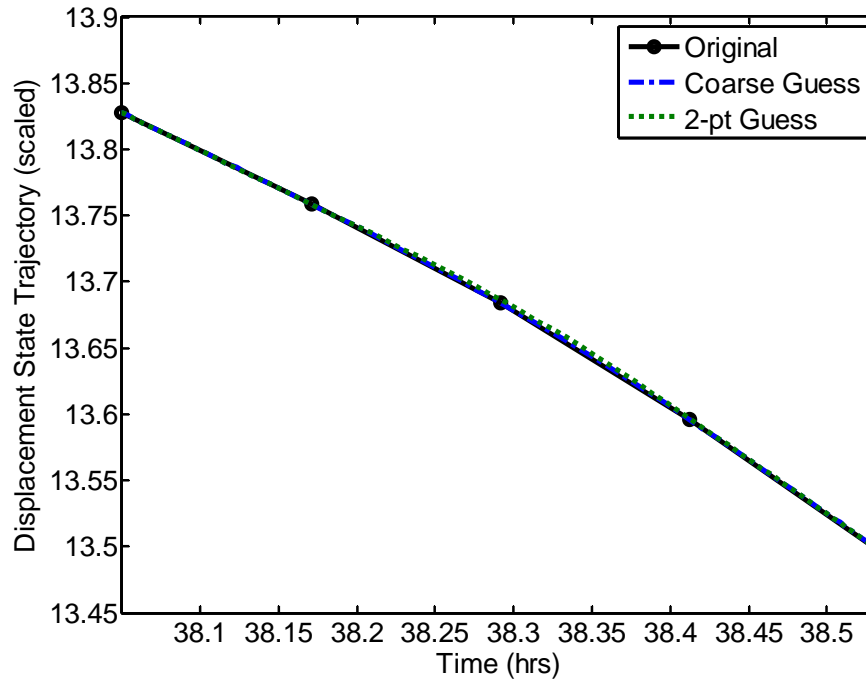


Figure 64. Displacement State (\bar{r}) Trajectories for TH1

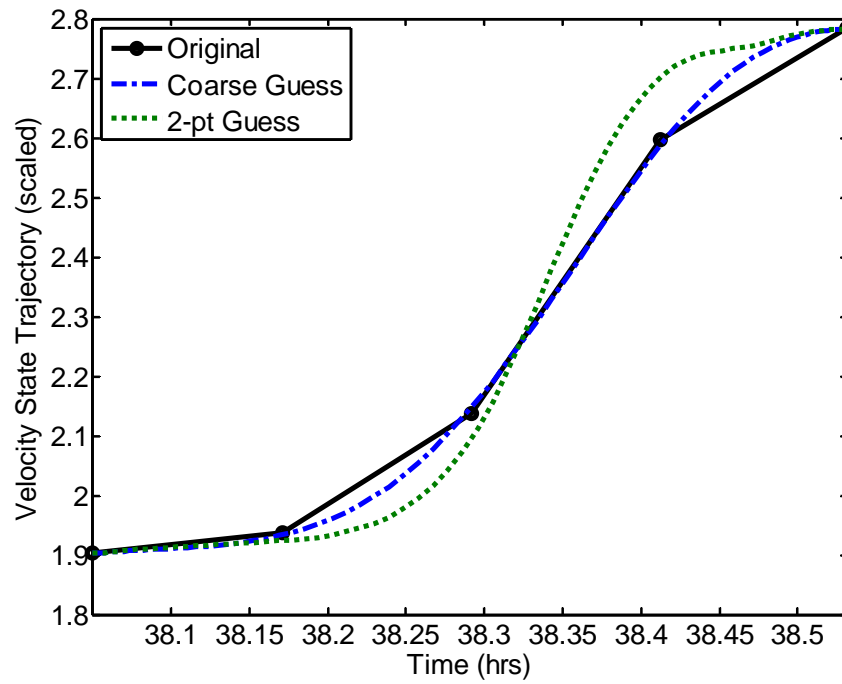


Figure 65. Velocity State (\bar{v}) Trajectories For TH1

The overall change in mass is the same for the two feasible solutions as shown in Figure 66. The mass state trajectory is clearly related to the shorter duration, but higher magnitude of thrust in the 2-point guess solution as compared to the solution from the coarse guess.

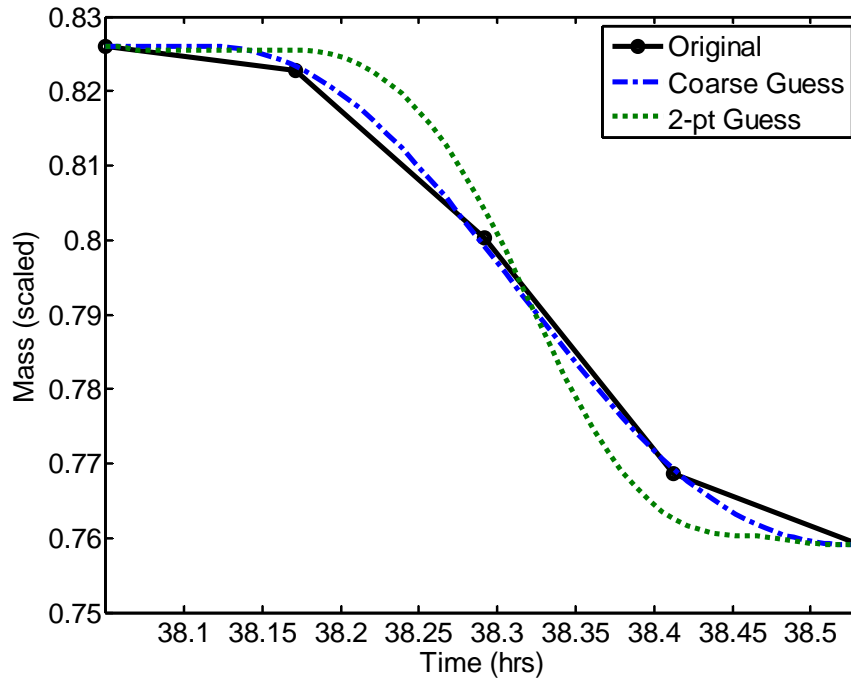


Figure 66. Fuel Consumption for TH1

C. TH2 RESULTS

The same analysis conducted for the TH1 solutions was performed for TH2 and TH3. The Hamiltonian Minimization Conditions for optimality were met, as well as the additional conditions for singular arcs. Each case resulted in different feasible solutions for the controls, with the state variable trajectories satisfying the fixed boundary conditions. And while the state trajectories vary slightly between the cases, the fuel consumption is the same between the original coarse solution and the optimal solutions. These results further indicate the range of possibilities for conducting the singular arc maneuver.

In TH1, the maximum thrust exceeded the maximum thrust of the auxiliary engines; however the resulting control trajectories for TH2 and TH3 achieved maximum thrust less than the auxiliary engines (4.4 kN). This gives some indication that the

auxiliary engines can indeed be used for the singular burn maneuver; however the fuel consumption will necessarily be greater due to the lower rocket specific impulse as compared to the main engines.

Figures 67, 68, and 69 show the control trajectories for TH2. The maximum thrust for both solutions is about the same, around 4 kN. The control angles during the burn are identical to the angles arrived at in the TH1 solutions. They are also found to be equal in the TH3 solutions as well. Clearly, a rocket engine with maximum thrust of 4.4 kN would be able to execute these maneuvers. The difference will be in fuel consumption alone.

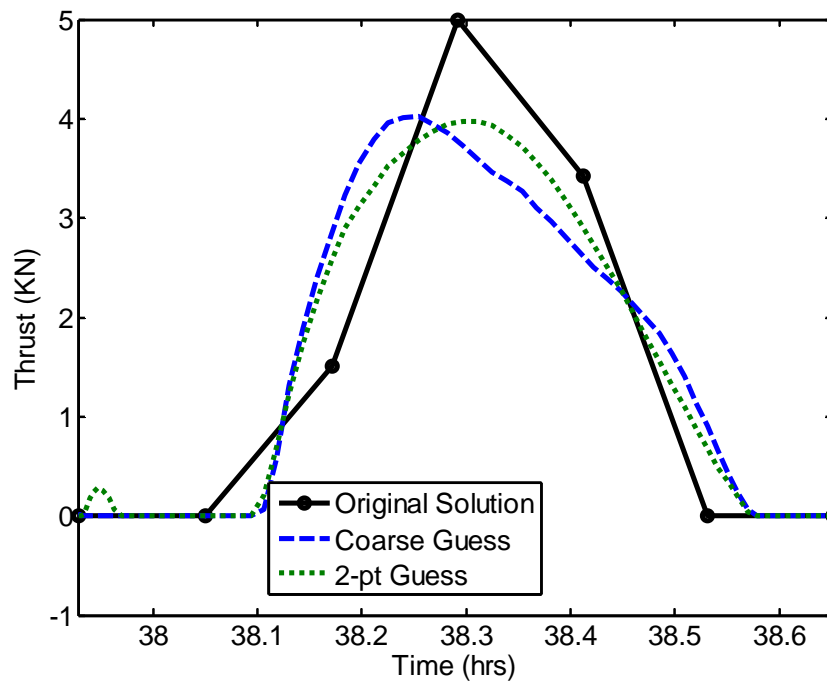


Figure 67. Thrust Trajectories for TH2

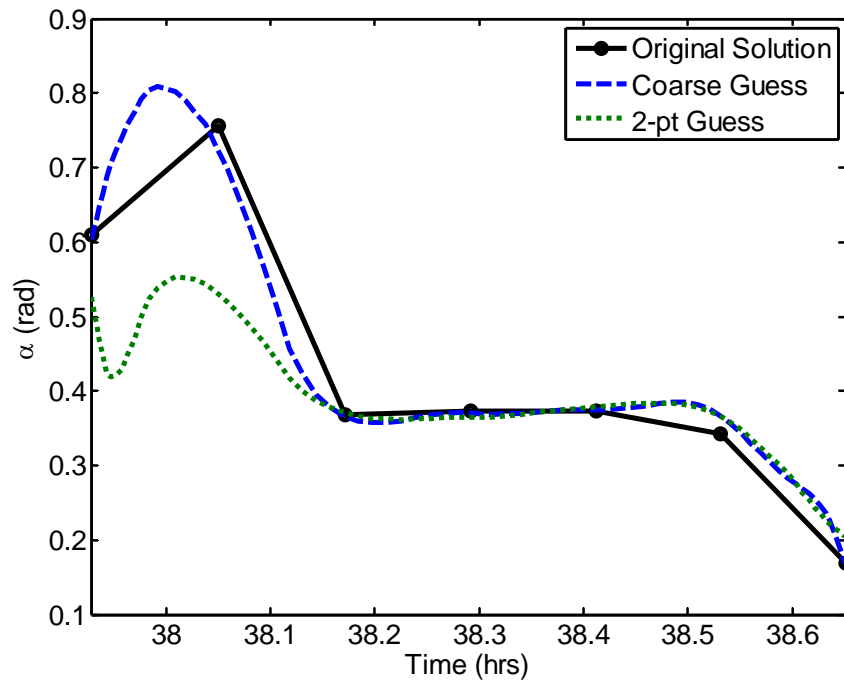


Figure 68. Azimuth Angle Trajectories for TH2

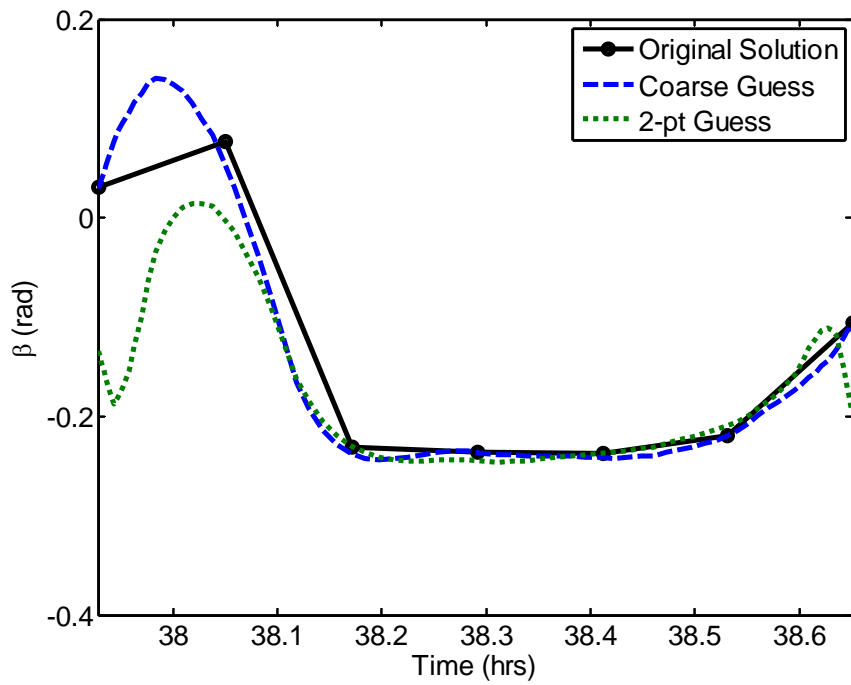


Figure 69. Elevation Angle Trajectories for TH2

Neither of the state trajectories have the same aliasing that was seen in TH1, however the two solutions, using different initial starting guesses, are very similar as seen by the control trajectories above and the state trajectories shown in Figures 70, 71 and 72.

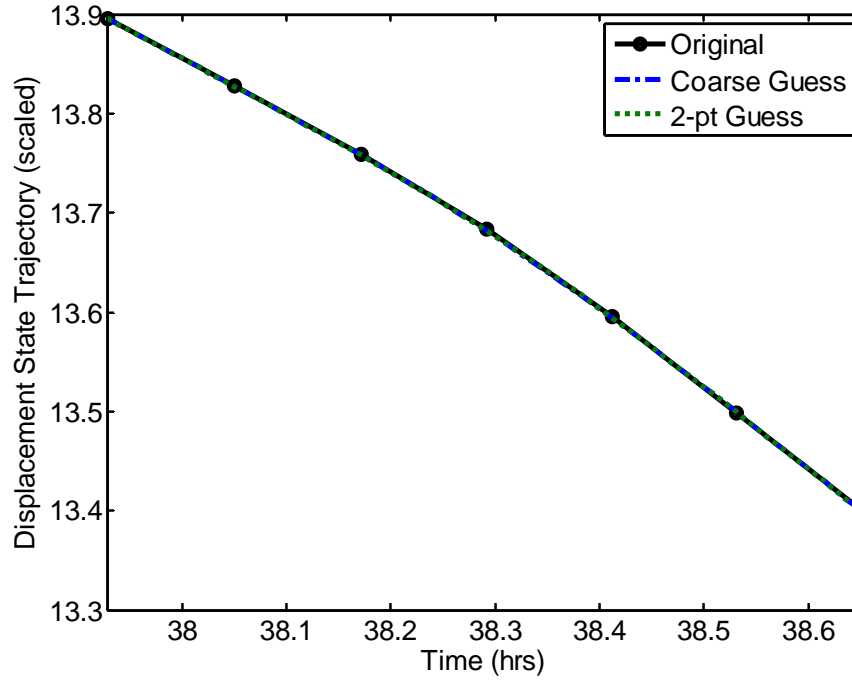


Figure 70. Displacement State (\bar{r}) Trajectories for TH2

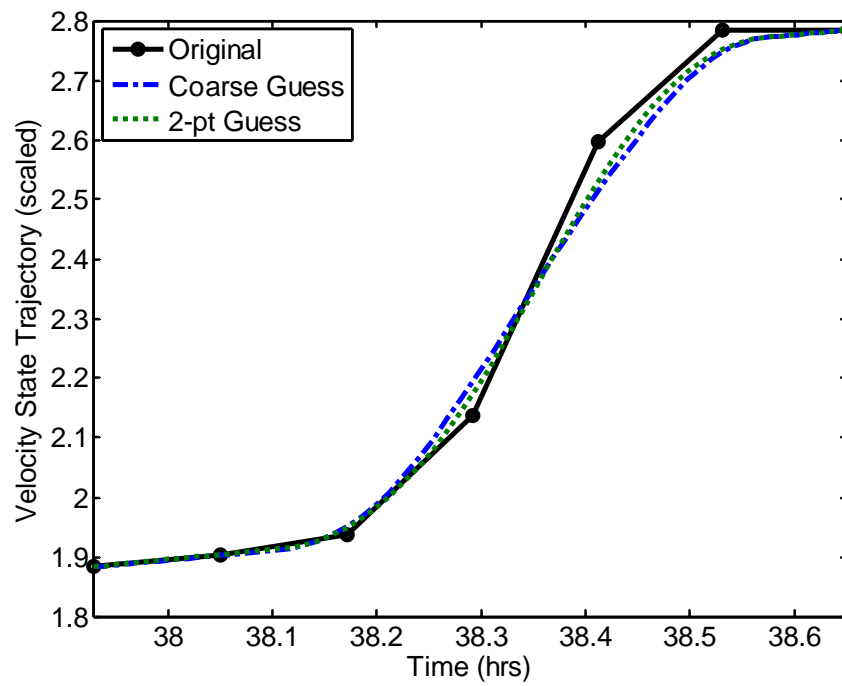


Figure 71. Velocity State (\bar{v}) Trajectories for TH2

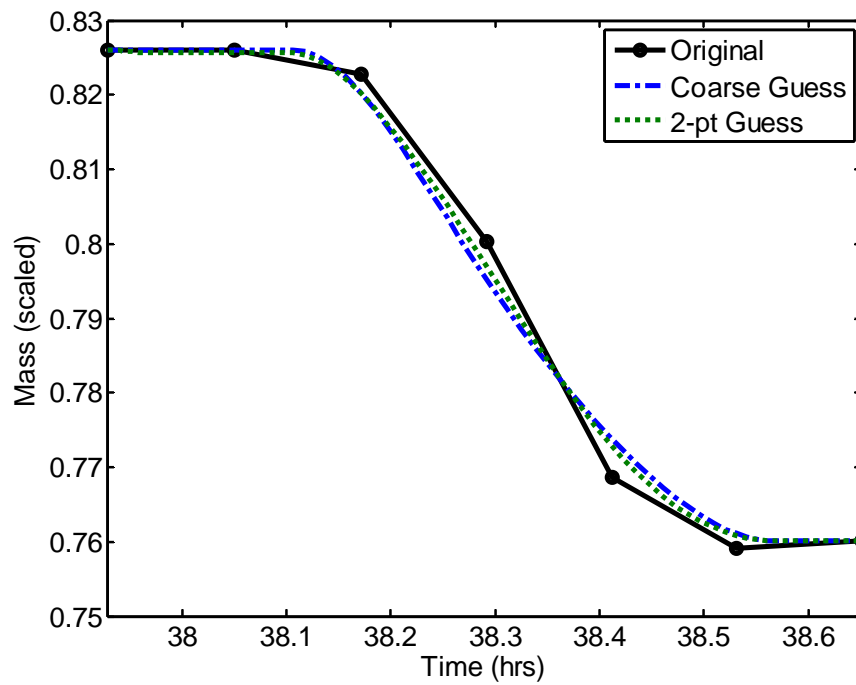


Figure 72. Fuel Consumption for TH2

The fuel consumption for TH2 is listed in Table 7 and the differences are again negligible as compared to the original coarse solution within the specific time horizon.

	Fuel Consumed (kg)	Variation
Original Coarse Solution	1,339.7	--
Using Coarse Guess	1,339.1	0.0007 %
Using 2-point Guess	1,339.2	0.0004 %

Table 7. TH2 Fuel Consumption

D. TH3 RESULTS

By expanding the time horizon to TH3, the control trajectories begin to deviate from the original solution. These solutions also meet the optimality conditions for singular arcs and are also feasible solutions. In both solutions arrived at from different initial guesses, the maximum thrust is again less than 4.4 kN indicating that this particular control profile could be used with the auxiliary engines. The solution from the 2-point guess is interesting in that the thrust profile is starting to appear as a bang-bang maneuver, however in this situation remains a singular arc solution. In general, these solutions are not as “clean” from a control perspective because neither solution has a zero to zero thrust trajectory. In both cases there is a non-zero initial thrust as seen in Figure 73. In Figures 74 and 75 the control angles are approximately the same for both initial guesses even though the coarse gain has a single burn while the 2-point guess solution has a two burn solution.

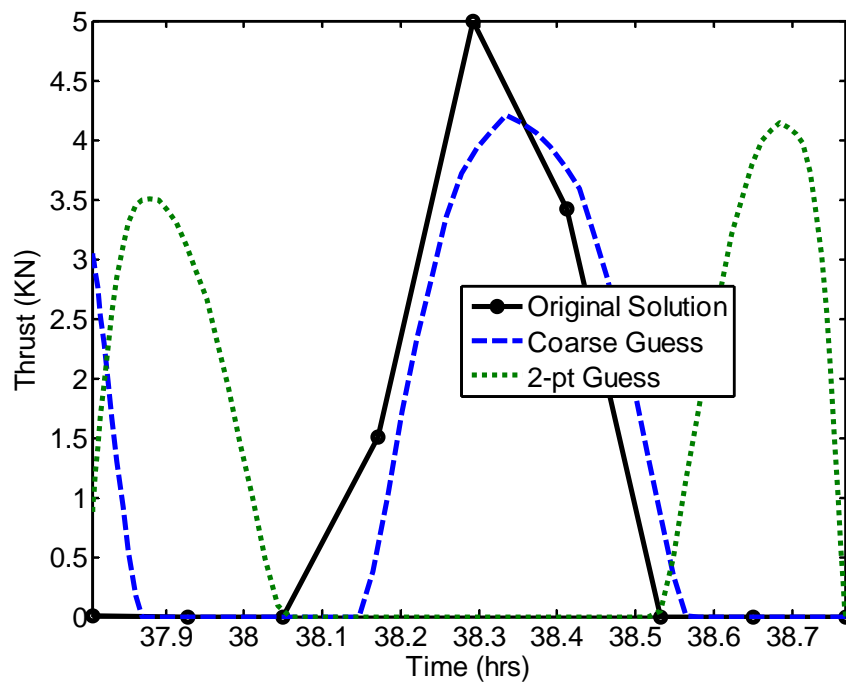


Figure 73. Thrust Trajectories for TH3

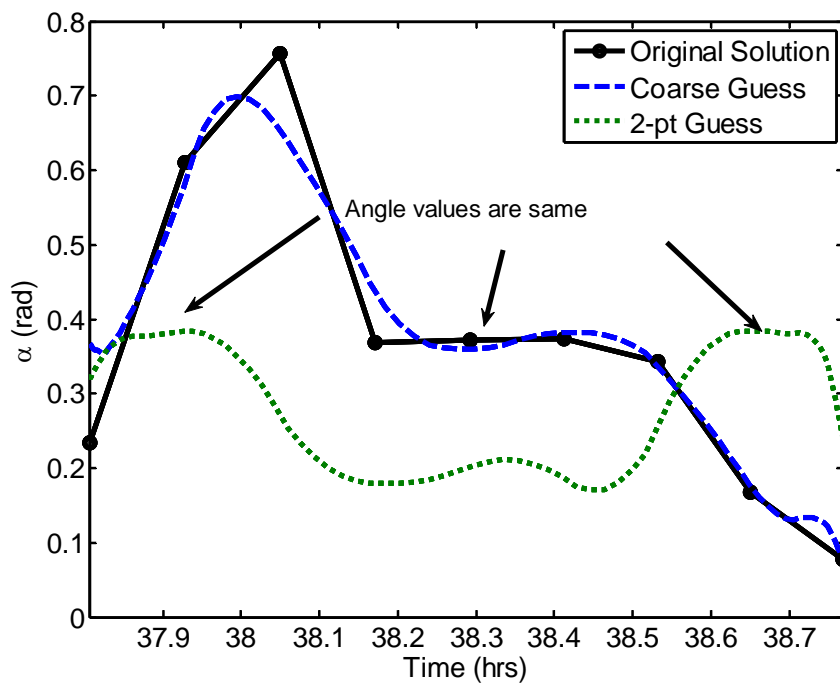


Figure 74. Azimuth Angle Trajectories for TH3

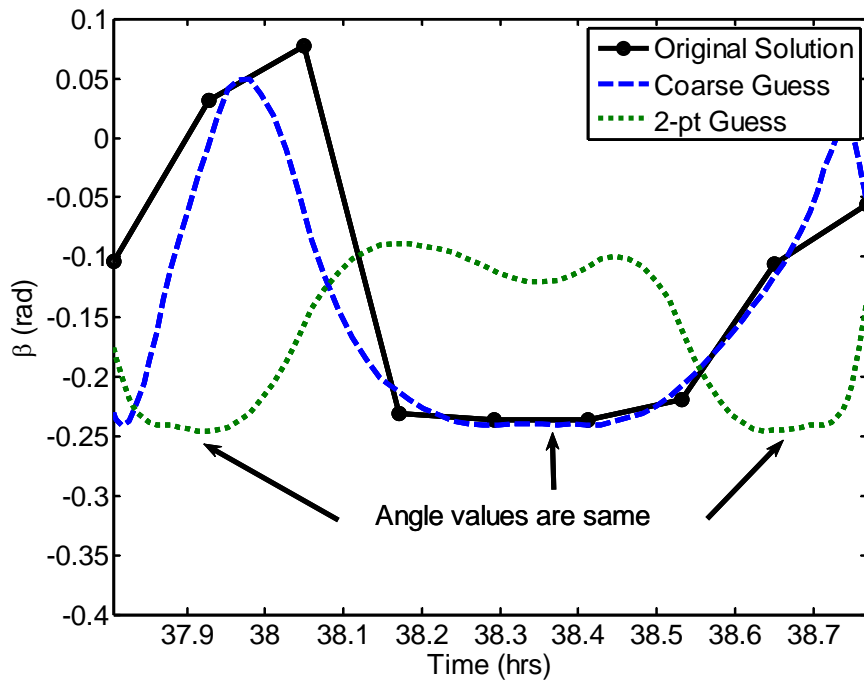


Figure 75. Elevation Angle Trajectories for TH3

The state trajectories as shown in Figures 76, 77, and 78 illustrate a more extreme example of varying state trajectories with the minimized cost of fuel being equal, emphasizing the result that multiple local minimal solutions exist around the singular arc. Table 8 shows the negligible difference in fuel from the original coarse solution for the given time horizon.

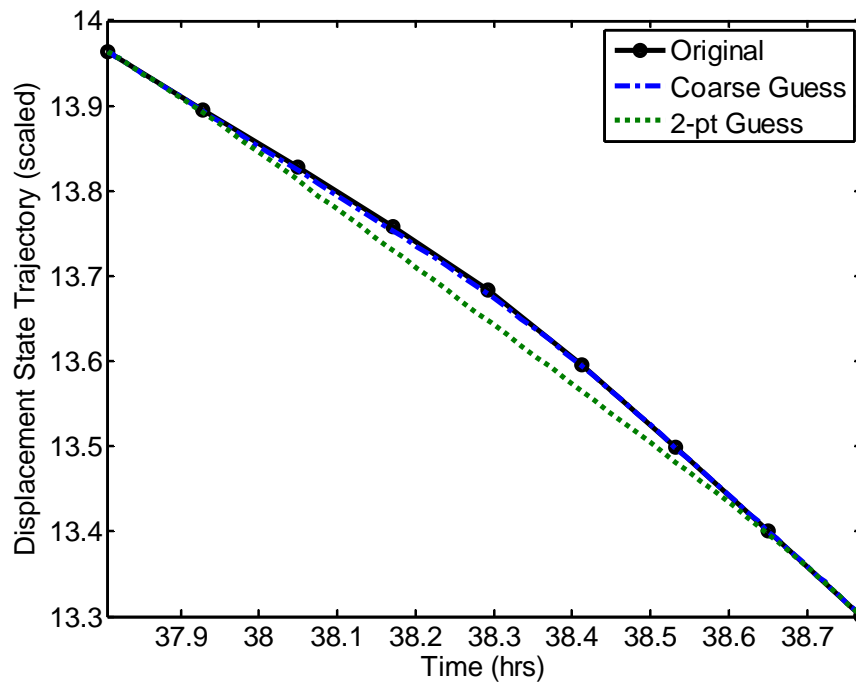


Figure 76. Displacement State Trajectories (TH3)

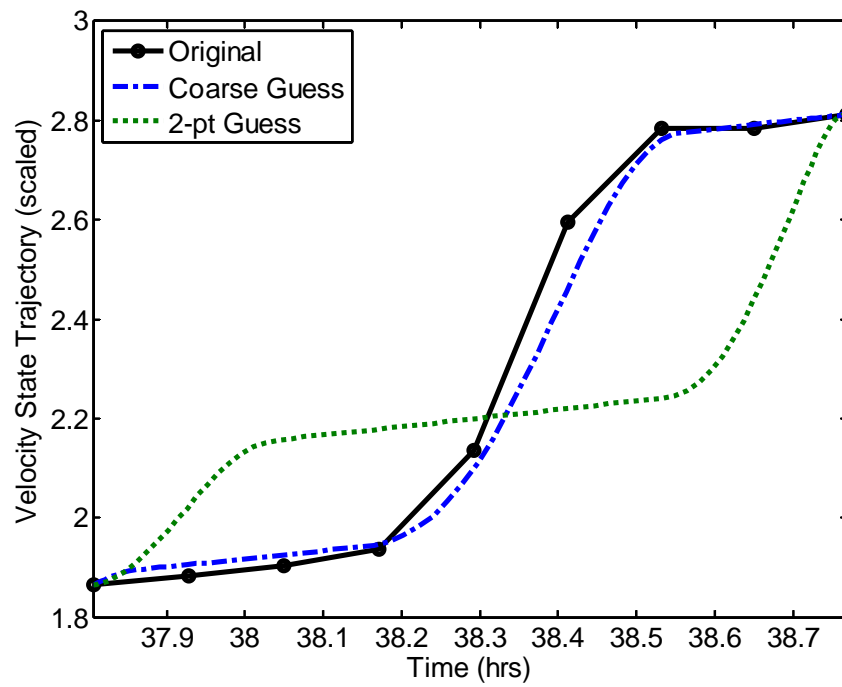


Figure 77. Velocity Trajectories (TH3)

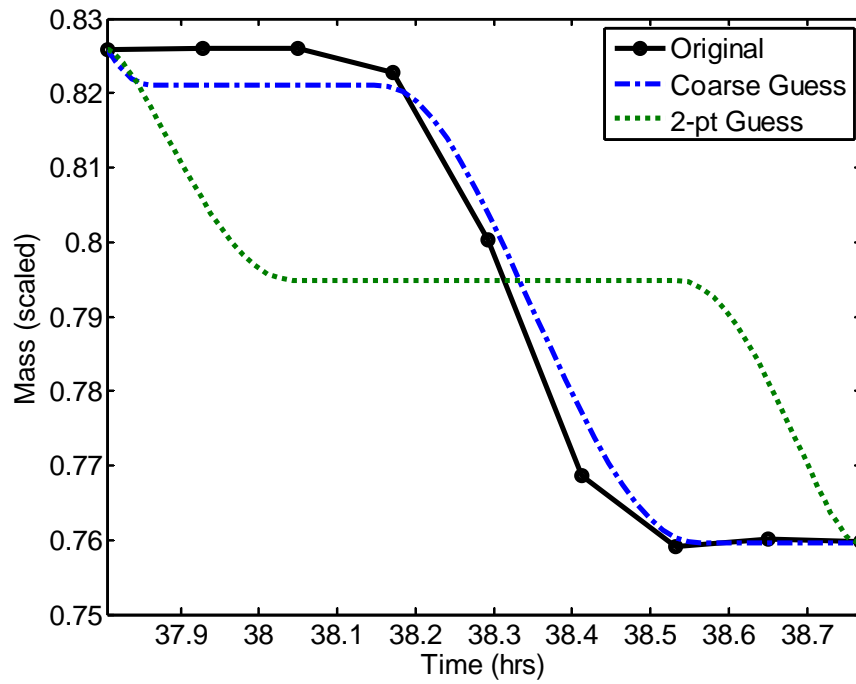


Figure 78. Fuel Consumption (TH3)

	Fuel Consumed (kg)	Variation
Original Coarse Solution	1,345.8	--
Using Coarse Guess	1,346.3	0.0007 %
Using 2-point Guess	1,346.7	0.0004 %

Table 8. Fuel Consumption for TH3

E. FEASIBILITY OF USING AUXILIARY ENGINES FOR SINGULAR ARC MANEUVER

In the analysis of the singular arc using the main engine, it was found that for the TH2 and TH3 time horizons, it appeared feasible to use the auxiliary engines in place of the main engines to conduct the singular arc maneuver. However, the TH1 solutions

using the main engine resulted in thrust profiles that exceeded the capacity of the auxiliary engines. It was expected that the lower Isp would result in a higher fuel consumption as compared to the main engine, given the same magnitude of thrust. The same six simulations as examined in the previous section were performed using the same optimal control problem formulation, but using the thrust and Isp parameters for the auxiliary engines.

As expected, the control profiles around TH2 and TH3 using the auxiliary engines were identical to those found using the main engines. The TH1 solution for the auxiliary engines however, was constrained in maximum thrust and resulted in a different, yet feasible control structure. Figure 79 shows the different thrust profiles attained in the TH1 time horizon using the same initial primal guess from the main engine singular arc. In this case, the two different initial guesses resulted in very similar control profiles.

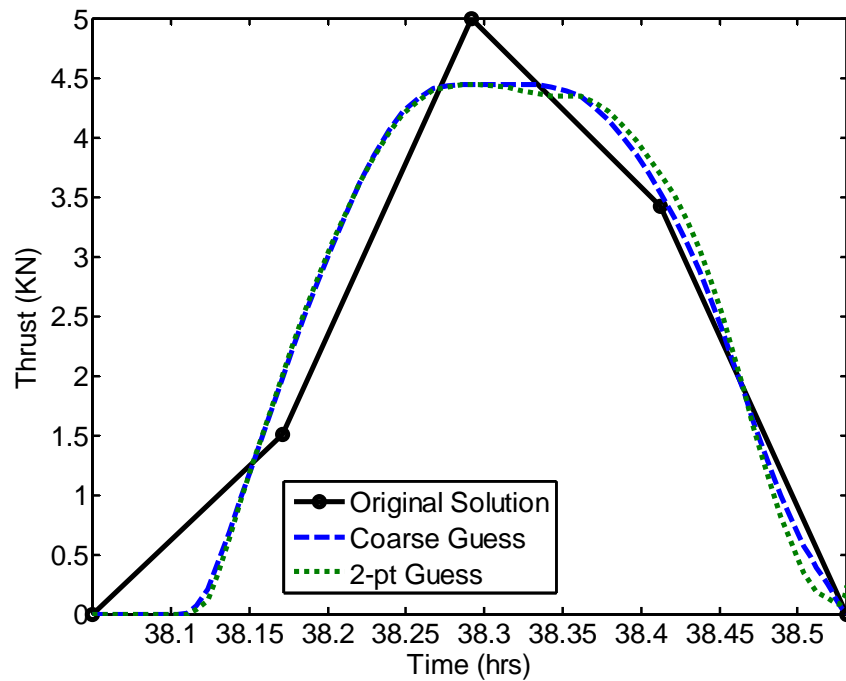


Figure 79. Auxiliary Engine Thrust Profile (TH1)

In all three time horizons, using the auxiliary engines resulted in an increase in fuel consumption as shown in Table 9. The results show that for a relatively small increase of fuel, the singular arc maneuver can be conducted using the auxiliary engines. In order to solve for the total trajectory fuel consumption where the main engines are used for the first and third TEI burn and the auxiliary engine is used for the singular arc maneuver, another step using the minimum fuel problem formulation needs to be conducted between the boundary conditions of the singular arc time horizon and the original boundary conditions provided to solve the full moon-to-earth trajectory problem.

	Main Engine (33.1 kN)	Aux Engine (4.4 kN)
Singular Arc on Full Trajectory (Yan et al., 2010)	1,333.6 kg	---
TH1	1,361.0 kg	1,432.6 kg
TH2	1,339.1 kg	1,409.6 kg
TH3	1,346.3 kg	1,417.1 kg

Table 9. Fuel Consumption Comparison Between Main Engine and Auxiliary Engines Over Singular Arc

F. CONCLUSIONS

The reason that multiple feasible and optimal solutions appear is because of the existence of the singular arc. Recalling that the switching function equals zero for a singular arc, it is clear that the resulting magnitude of thrust can lie between the minimum and maximum thrust. If the initial and final boundary conditions are established at varying positions in time before and after the singular arc, it is possible to generate different control solutions and thus, different state trajectories that are also optimal solutions. This gives rise to the possibility of multiple feasible solutions between two given boundary conditions with a singular arc between them. From an engineering point of view, this offers greater flexibility in designing a solution that closer resembles the

imposed physical constraints on the available controllers. The difficulty though, is in finding a fuel optimal solution that meets the given constraints and requirements from a possible myriad of solutions. For example, while some modern rocket engines may have the ability to throttle, many typical rockets are forced to apply a bang-bang type control. In seeking for a bang-bang solution to perform the same maneuver as the singular arc, additional constraints will have to be imposed, thus changing the problem formulation. It is possible to use pseudo-spectral tools such as DIDO© to find a range of optimal bang-bang solutions, however it is likely that the fuel cost will be greater.

The singular arc maneuver results in a slight change in the orbits eccentricity (semi-major axis); however it appears that the maneuver is used primarily to change the orbit plane (inclination). Further study of orbit maneuvers may show that singular arcs will appear in fuel optimal orbit transfers whenever an inclination change occurs, assuming that the rocket thrust is allowed the full range from null to maximum. To further examine the nature of fuel-optimal plane change maneuvers, it would be prudent to examine pure plane change maneuvers as well as combined plane change and apogee raising (or lowering) maneuvers using similar n-body dynamics equations as used here.

APPENDIX A. SINGULAR ARC NECESSARY CONDITIONS

From Park et al., 2010:

Switching function

$$S = -\frac{\sqrt{\bar{\lambda}_v \cdot \bar{\lambda}_v}}{m} - \frac{\lambda_m}{v_e} = 0$$

First derivative

$$\frac{dS}{dt} = \frac{\bar{\lambda}_r \cdot \bar{\lambda}_v}{m\sqrt{\bar{\lambda}_v \cdot \bar{\lambda}_v}} = 0$$

Second derivative

$$\frac{d^2S}{dt^2} = \frac{1}{m\sqrt{\bar{\lambda}_v \cdot \bar{\lambda}_v}} \left[-\bar{\lambda}_r \cdot \bar{\lambda}_r + \left(\frac{\mu}{r^3} + \frac{\mu_i}{r_i^3} \right) (\bar{\lambda}_v \cdot \bar{\lambda}_v) - 3 \left(\frac{\mu (\bar{r} \cdot \bar{\lambda}_v)^2}{r^5} + \frac{\mu_i (\bar{r}_i \cdot \bar{\lambda}_v)^2}{r_i^5} \right) \right]$$

Third derivative

$$\begin{aligned} \frac{d^3S}{dt^3} &= \frac{1}{m\sqrt{\bar{\lambda}_v \cdot \bar{\lambda}_v}} \left[-\frac{3\mu (\bar{r} \cdot \bar{v}) (\bar{\lambda}_v \cdot \bar{\lambda}_v)}{r^5} - \frac{3\mu_i (\bar{r}_i \cdot \bar{v}_i) (\bar{\lambda}_v \cdot \bar{\lambda}_v)}{r_i^5} \right. \\ &\quad - \frac{6\mu (\bar{r} \cdot \bar{\lambda}_v) (\bar{v} \cdot \bar{\lambda}_v)}{r^5} - \frac{6\mu_i (\bar{r}_i \cdot \bar{\lambda}_v) (\bar{v}_i \cdot \bar{\lambda}_v)}{r_i^5} \\ &\quad - \frac{12\mu (\bar{r} \cdot \bar{\lambda}_r) (\bar{r} \cdot \bar{\lambda}_v)}{r^5} - \frac{12\mu_i (\bar{r}_i \cdot \bar{\lambda}_r) (\bar{r}_i \cdot \bar{\lambda}_v)}{r_i^5} \\ &\quad \left. - \frac{15\mu (\bar{r} \cdot \bar{v}) (\bar{r} \cdot \bar{\lambda}_v)^2}{r^7} - \frac{15\mu_i (\bar{r}_i \cdot \bar{v}_i) (\bar{r}_i \cdot \bar{\lambda}_v)^2}{r_i^7} \right] \\ &= \frac{1}{m\sqrt{\bar{\lambda}_v \cdot \bar{\lambda}_v}} [S_{3,1} + S_{3,5} + S_{3,2} + S_{3,6} + S_{3,3} + S_{3,7} + S_{3,4} + S_{3,8}] = 0 \end{aligned}$$

Fourth derivative

$$\begin{aligned}
\frac{d^4 S}{dt^4} &= \frac{d}{dt} \left(\frac{1}{m\sqrt{\bar{\lambda}_v \cdot \bar{\lambda}_v}} \right) [S_3] + \frac{1}{m\sqrt{\bar{\lambda}_v \cdot \bar{\lambda}_v}} \frac{d}{dt} [S_3] \\
&= \frac{1}{m\sqrt{\bar{\lambda}_v \cdot \bar{\lambda}_v}} \frac{d}{dt} [S_3], \quad \text{where } [S_3] = \sum_{j=1}^8 S_{3,j} \\
&= \frac{1}{m\sqrt{\bar{\lambda}_v \cdot \bar{\lambda}_v}} \sum_{j=1}^8 S_{4,j}, \quad \text{where } S_{4,j} = \frac{dS_{3,j}}{dt} \\
\\
S_{4,1} &= \mu \left[\frac{3(\bar{v} \cdot \bar{v})(\bar{\lambda}_v \cdot \bar{\lambda}_v)}{r^5} - \frac{15(\bar{r} \cdot \bar{v})^2(\bar{\lambda}_v \cdot \bar{\lambda}_v)}{r^7} - \frac{3\mu(\bar{r} \cdot \bar{r})(\bar{\lambda}_v \cdot \bar{\lambda}_v)}{r^8} - \frac{3\mu_i(\bar{r} \cdot \bar{r}_i)(\bar{\lambda}_v \cdot \bar{\lambda}_v)}{r^5 r_i^3} \right. \\
&\quad \left. - \frac{3(\bar{r} \cdot \bar{a}_M)(\bar{\lambda}_v \cdot \bar{\lambda}_v)}{r^5} + \frac{3(\bar{r} \cdot \bar{\lambda}_v)\sqrt{\bar{\lambda}_v \cdot \bar{\lambda}_v}}{r^5} \frac{T}{m} \right] \\
\\
S_{4,2} &= \mu \left[-\frac{15(\bar{v} \cdot \bar{v})(\bar{r} \cdot \bar{\lambda}_v)^2}{r^7} - \frac{30(\bar{r} \cdot \bar{v})(\bar{r} \cdot \bar{\lambda}_v)(\bar{v} \cdot \bar{\lambda}_v)}{r^7} + \frac{30(\bar{r} \cdot \bar{v})(\bar{r} \cdot \bar{\lambda}_r)(\bar{v} \cdot \bar{\lambda}_v)}{r^7} \right. \\
&\quad + \frac{105(\bar{r} \cdot \bar{v})^2(\bar{r} \cdot \bar{\lambda}_v)^2}{r^9} + \frac{15\mu(\bar{r} \cdot \bar{r})(\bar{r} \cdot \bar{\lambda}_v)^2}{r^{10}} + \frac{15\mu_i(\bar{r} \cdot \bar{r}_i)(\bar{r} \cdot \bar{\lambda}_v)^2}{r^7 r_i^3} \\
&\quad \left. + \frac{15(\bar{r} \cdot \bar{a}_M)(\bar{r} \cdot \bar{\lambda}_v)^2}{r^7} - \frac{15(\bar{r} \cdot \bar{\lambda}_v)^3}{r^7 \sqrt{\bar{\lambda}_v \cdot \bar{\lambda}_v}} \frac{T}{m} \right] \\
\\
S_{4,3} &= \mu \left[\frac{6(\bar{v} \cdot \bar{\lambda}_v)^2}{r^5} - \frac{6(\bar{r} \cdot \bar{\lambda}_r)(\bar{v} \cdot \bar{\lambda}_v)}{r^5} - \frac{6(\bar{r} \cdot \bar{\lambda}_v)(\bar{v} \cdot \bar{\lambda}_r)}{r^5} - \frac{30(\bar{r} \cdot \bar{v})(\bar{r} \cdot \bar{\lambda}_v)(\bar{v} \cdot \bar{\lambda}_v)}{r^7} \right. \\
&\quad \left. - \frac{6\mu(\bar{r} \cdot \bar{\lambda}_v)^2}{r^8} - \frac{6\mu_i(\bar{r} \cdot \bar{\lambda}_v)(\bar{r}_i \cdot \bar{\lambda}_v)}{r^5 r_i^3} - \frac{6(\bar{r} \cdot \bar{\lambda}_v)(\bar{a}_M \cdot \bar{\lambda}_v)}{r^5} + \frac{6(\bar{r} \cdot \bar{\lambda}_v)\sqrt{\bar{\lambda}_v \cdot \bar{\lambda}_v}}{r^5} \frac{T}{m} \right]
\end{aligned}$$

$$\begin{aligned}
S_{4,4} &= \mu \left[\frac{12(\bar{r} \cdot \bar{\lambda}_r)^2}{r^5} - \frac{12(\bar{r} \cdot \bar{\lambda}_v)(\bar{v} \cdot \bar{\lambda}_r)}{r^5} - \frac{12(\bar{r} \cdot \bar{\lambda}_r)(\bar{v} \cdot \bar{\lambda}_v)}{r^5} + \frac{60(\bar{r} \cdot \bar{v})(\bar{r} \cdot \bar{\lambda}_r)(\bar{r} \cdot \bar{\lambda}_v)}{r^7} \right. \\
&\quad \left. - \frac{12\mu(\bar{r} \cdot \bar{\lambda}_v)^2}{r^8} - \frac{12\mu_i(\bar{r} \cdot \bar{\lambda}_v)^2}{r^5 r_i^3} + \frac{36(\bar{r} \cdot \bar{r})(\bar{r} \cdot \bar{\lambda}_v)^2}{r^{10}} + \frac{36(\bar{r} \cdot \bar{r}_i)(\bar{r} \cdot \bar{\lambda}_v)(\bar{r}_i \cdot \bar{\lambda}_v)}{r^5 r_i^5} \right] \\
S_{4,5} &= \mu_i \left[\frac{3(\bar{v}_i \cdot \bar{v}_i)(\bar{\lambda}_v \cdot \bar{\lambda}_v)}{r_i^5} - \frac{15(\bar{r}_i \cdot \bar{v}_i)^2(\bar{\lambda}_v \cdot \bar{\lambda}_v)}{r_i^7} - \frac{3\mu_i(\bar{r}_i \cdot \bar{r}_i)(\bar{\lambda}_v \cdot \bar{\lambda}_v)}{r_i^8} \right. \\
&\quad \left. - \frac{3\mu(\bar{r} \cdot \bar{r}_i)(\bar{\lambda}_v \cdot \bar{\lambda}_v)}{r^3 r_i^5} - \frac{3(\bar{r}_i \cdot \bar{a}_l)(\bar{\lambda}_v \cdot \bar{\lambda}_v)}{r_i^5} + \frac{3(\bar{r}_i \cdot \bar{\lambda}_v)\sqrt{\bar{\lambda}_v \cdot \bar{\lambda}_v}}{r_i^8} \frac{T}{m} \right] \\
S_{4,6} &= \mu_i \left[-\frac{15(\bar{v}_i \cdot \bar{v}_i)(\bar{r}_i \cdot \bar{\lambda}_v)^2}{r_i^7} - \frac{30(\bar{r}_i \cdot \bar{v}_i)(\bar{r}_i \cdot \bar{\lambda}_v)(\bar{v}_i \cdot \bar{\lambda}_v)}{r_i^7} + \frac{30(\bar{r}_i \cdot \bar{v}_i)(\bar{r}_i \cdot \bar{\lambda}_r)(\bar{r}_i \cdot \bar{\lambda}_v)}{r_i^7} \right. \\
&\quad + \frac{105(\bar{r}_i \cdot \bar{v}_i)^2(\bar{r}_i \cdot \bar{\lambda}_v)^2}{r_i^9} + \frac{15\mu_i(\bar{r}_i \cdot \bar{r}_i)(\bar{r}_i \cdot \bar{\lambda}_v)^2}{r_i^{10}} + \frac{15\mu(\bar{r} \cdot \bar{r}_i)(\bar{r}_i \cdot \bar{\lambda}_v)^2}{r^3 r_i^7} \\
&\quad \left. + \frac{15(\bar{r}_i \cdot \bar{a}_l)(\bar{r}_i \cdot \bar{\lambda}_v)^2}{r_i^7} - \frac{15(\bar{r}_i \cdot \bar{\lambda}_v)^3}{r_i^7 \sqrt{\bar{\lambda}_v \cdot \bar{\lambda}_v}} \frac{T}{m} \right] \\
S_{4,7} &= \mu_i \left[\frac{6(\bar{v}_i \cdot \bar{\lambda}_v)^2}{r_i^5} - \frac{6(\bar{r}_i \cdot \bar{\lambda}_r)(\bar{v}_i \cdot \bar{\lambda}_v)}{r_i^5} - \frac{6(\bar{r}_i \cdot \bar{\lambda}_v)(\bar{v}_i \cdot \bar{\lambda}_r)}{r_i^5} - \frac{30(\bar{r}_i \cdot \bar{v}_i)(\bar{r}_i \cdot \bar{\lambda}_v)(\bar{v}_i \cdot \bar{\lambda}_v)}{r_i^7} \right. \\
&\quad \left. - \frac{6\mu_i(\bar{r}_i \cdot \bar{\lambda}_v)^2}{r_i^8} - \frac{6\mu(\bar{r} \cdot \bar{\lambda}_v)(\bar{r}_i \cdot \bar{\lambda}_v)}{r^3 r_i^5} - \frac{6(\bar{r}_i \cdot \bar{\lambda}_v)(\bar{a}_l \cdot \bar{\lambda}_v)}{r_i^5} + \frac{6(\bar{r}_i \cdot \bar{\lambda}_v)\sqrt{\bar{\lambda}_v \cdot \bar{\lambda}_v}}{r_i^5} \frac{T}{m} \right] \\
S_{4,8} &= \mu_i \left[\frac{12(\bar{r}_i \cdot \bar{\lambda}_r)^2}{r_i^5} - \frac{12(\bar{r}_i \cdot \bar{\lambda}_v)(\bar{v}_i \cdot \bar{\lambda}_r)}{r_i^5} - \frac{12(\bar{r}_i \cdot \bar{\lambda}_r)(\bar{v}_i \cdot \bar{\lambda}_v)}{r_i^5} + \frac{60(\bar{r}_i \cdot \bar{v}_i)(\bar{r}_i \cdot \bar{\lambda}_r)(\bar{r}_i \cdot \bar{\lambda}_v)}{r_i^7} \right. \\
&\quad \left. - \frac{12\mu_i(\bar{r}_i \cdot \bar{\lambda}_v)^2}{r_i^8} - \frac{12\mu(\bar{r}_i \cdot \bar{\lambda}_v)^2}{r^3 r_i^5} + \frac{36(\bar{r}_i \cdot \bar{r}_i)(\bar{r}_i \cdot \bar{\lambda}_v)^2}{r_i^{10}} + \frac{36(\bar{r} \cdot \bar{r}_i)(\bar{r} \cdot \bar{\lambda}_v)(\bar{r}_i \cdot \bar{\lambda}_v)}{r^5 r_i^5} \right]
\end{aligned}$$

Legendre-Clebesch Condition (convexity)

$$\begin{aligned} (-1)^4 \frac{\partial}{\partial T} \frac{d^4}{dt^4} \left(\frac{\partial H}{\partial T} \right) &= \frac{\partial}{\partial T} \frac{d^4 S}{dt^4} \geq 0 \\ \Rightarrow \frac{1}{m^2} \left[\frac{9\mu(\bar{r} \cdot \bar{\lambda}_v)}{r^5} + \frac{9\mu_i(\bar{r}_i \cdot \bar{\lambda}_v)}{r_i^5} - \frac{15\mu(\bar{r} \cdot \bar{\lambda}_v)^3}{r^7(\bar{\lambda}_v \cdot \bar{\lambda}_v)} - \frac{15\mu_i(\bar{r}_i \cdot \bar{\lambda}_v)^3}{r_i^7(\bar{\lambda}_v \cdot \bar{\lambda}_v)} \right] &\geq 0 \end{aligned}$$

APPENDIX B. END-POINT TRANSVERSALITY CONDITION

The transversality condition states:

$$\underline{\lambda}(t_f) = \frac{\partial \bar{E}}{\partial \underline{x}_f}, \text{ where } \bar{E}(\underline{v}, \underline{x}(t_f)) = E(\underline{x}(t_f)) + \underline{v}^T e(\underline{x}(t_f))$$

The variable, \underline{v} , represents the Lagrange multiplier vector associated with the end-point state condition, $e(\underline{x}(t_f))$. The end-point cost is $E(\underline{x}(t_f))$. The given end-point boundary condition is defined as $\underline{x}^f = [x^f, y^f, z^f, v_x^f, v_y^f, v_z^f]$. As can be seen in each of the problems, the only additional information yielded is $\lambda_m(t_f)$.

Minimum Fuel Problem End-point Transversality Condition

$$\begin{aligned} \bar{E}(\underline{v}, \underline{x}(t_f)) = & m_0 - m_f + v_1(x_f - x^f) + v_2(y_f - y^f) + v_3(z_f - z^f) + \\ & v_4(v_{xf} - v_x^f) + v_5(v_{yf} - v_y^f) + v_6(v_{zf} - v_z^f) \end{aligned}$$

$$\lambda_x(t_f) = \frac{\partial \bar{E}}{\partial x_f} = v_1$$

$$\lambda_y(t_f) = \frac{\partial \bar{E}}{\partial y_f} = v_2$$

$$\lambda_z(t_f) = \frac{\partial \bar{E}}{\partial z_f} = v_3$$

$$\lambda_{vx}(t_f) = \frac{\partial \bar{E}}{\partial v_{xf}} = v_4$$

$$\lambda_{vy}(t_f) = \frac{\partial \bar{E}}{\partial v_{yf}} = v_5$$

$$\lambda_{vz}(t_f) = \frac{\partial \bar{E}}{\partial v_{zf}} = v_6$$

$$\lambda_m(t_f) = \frac{\partial \bar{E}}{\partial m_f} = -1$$

Minimum Time Problem End-point Transversality Condition

$$\begin{aligned}\bar{E}(\underline{v}, \underline{x}(t_f)) = & t_f + \nu_1(x_f - x^f) + \nu_2(y_f - y^f) + \nu_3(z_f - z^f) + \\ & \nu_4(v_{xf} - v_x^f) + \nu_5(v_{yf} - v_y^f) + \nu_6(v_{zf} - v_z^f)\end{aligned}$$

$$\lambda_x(t_f) = \frac{\partial \bar{E}}{\partial x_f} = \nu_1$$

$$\lambda_y(t_f) = \frac{\partial \bar{E}}{\partial y_f} = \nu_2$$

$$\lambda_z(t_f) = \frac{\partial \bar{E}}{\partial z_f} = \nu_3$$

$$\lambda_{v_x}(t_f) = \frac{\partial \bar{E}}{\partial v_{xf}} = \nu_4$$

$$\lambda_{v_y}(t_f) = \frac{\partial \bar{E}}{\partial v_{yf}} = \nu_5$$

$$\lambda_{v_z}(t_f) = \frac{\partial \bar{E}}{\partial v_{zf}} = \nu_6$$

$$\lambda_m(t_f) = \frac{\partial \bar{E}}{\partial m_f} = 0$$

LIST OF REFERENCES

- Betts, J. T. (2001). *Practical methods for optimal control using nonlinear programming*. Philadelphia: Society for Industrial and Applied Mathematics.
- Bryson, A. E. (1975). *Applied optimal control: Optimization, estimation, and Control*. New York: Hemisphere Publishing Corporation.
- Curtis, H. D. (2005). *Orbital mechanics for engineering students*. Oxford: Elsevier Ltd.
- Jet Propulsion Laboratory. (n.d.). *Horizons system*. Retrieved October 29, 2010, from Jet Propulsion Laboratory: <http://ssd.jpl.nasa.gov/?horizons>
- Kirk, D. E. (1998). *Optimal control theory: An introduction*. Mineola: Dover Publishing, Inc.
- Park, C., Yan, H. Gong, Q., & Ross, I. M. (2010, February). Numerical verification of singular arcs on optimal moon-to-earth transfer. Document AAS 10-104. Paper presented at *20th AAS/AIAA Space Flight Mechanics Meeting*, San Diego.
- Park, C., Yan, H. Gong, Q., & Ross, I. M. (2010, February). Optimality of singular arcs for a rocket trajectory of mayer's variational problem. Document AAS 10-106. Paper presented at *20th AAS/AIAA Space Flight Mechanics Meeting*, San Diego.
- Pinch, E. R. (1993). *Optimal control and the calculus of variations*. New York: Oxford University Press Inc.
- Ross, I. M. (2007). "A beginner's guide to DIDO: A MATLAB application package for solving optimal control problems." *Elissar Technical Report TR-711* . Monterey, CA.
- Ross, I. M. (2009). *A primer on pontryagin's principle in optimal control*. San Francisco: Collegiate Publishers.
- Ross, I. M., Gong, Q., & Sehkavat, P. (2007). Low-thrust high-accuracy trajectory optimization. *Journal of Guidance, Control, and Dynamics*, Vol. 30, No. 4, pp. 921-933.
- Ross, I. M., Gong, Q., & Sehkavat, P. (2008, August). The bellman pseudospectral method. Document AIAA 2008-6448. Paper presented at *AIAA/AAS Astrodynamics Specialist Conference and Exhibit*, Honolulu.

- Scarritt, S., Marchand, B., & Weeks, M. (2009, August). An autonomous onboard targeting algorithm using finite thrust maneuvers. Paper presented at *AIAA Guidance, Navigation, and Control Conference and Exhibit*, Chicago.
- Vallado, D. A. (1997). *Fundamentals of astrodynamics and applications*. New York: McGraw-Hill.
- Yan, H., Gong, Q., Park, C., Ross, I. M., & Souza, C. (2010, August). High-accuracy moon to earth escape trajectory optimization. Paper presented at *AIAA Guidance, Navigation, and Control Conference*, Toronto.

INITIAL DISTRIBUTION LIST

1. Defense Technical Information Center
Ft. Belvoir, VA
2. Dudley Knox Library
Naval Postgraduate School
Monterey, CA
3. Head, Information Operations and Space Integration Branch
PLI/PP&O/HQMC
Washington, DC
4. Dr. Hui Yan
Dept. of Applied Math and Stats
MS SOE2
University of California, Santa Cruz
Santa Cruz, CA
5. Dr. Qi Gong
Dept. of Applied Math and Stats
MS SOE2
University of California, Santa Cruz
Santa Cruz, CA
6. Omar Wheatley
Author
Denver, CO